

Chirality-induced spin-selective Peierls transition

Shun Asano^{1,*} and Youichi Yanase^{1,†}

¹*Department of Physics, Kyoto University, Kyoto 606-8502, Japan*

Chirality, referring to the absence of mirror and inversion symmetries, is a ubiquitous concept in nature. In condensed matter physics, vigorous research has clarified how chiral materials harbour unconventional electronic and vibrational responses. In parallel, recent studies have demonstrated that chiral structures can be engineered or tuned from achiral precursors. Despite these complementary advances, an integrated understanding of electronic and phononic dynamics, self-organized chiral structures, and their interplay is still lacking. Such an integrated framework is crucial both for elucidating the spontaneous formation and stabilization of chiral structures and for advancing the electronic functionalities of chiral materials. Here, we predict novel spontaneous structural phase transitions unique to chiral crystals with screw symmetry. In quasi-one-dimensional chiral crystals, the phonon frequency renormalized by the electron-phonon coupling depends on the handedness of circular polarization. Consequently, the soft mode encoding the intrinsic phonon angular momentum induces spin-selective Peierls gaps in the electronic band, entailing a helical spin density wave and chiral lattice distortion. We also elucidate the chiral signature of collective modes. Our findings offer new avenues for advanced spintronics applications and crucial insights into the elusive mechanisms underlying the formation process of chirality in nature.

Main

Structure and functionality are inextricably linked in general. In condensed matter physics, the crystal structure rules static and dynamic properties, shaping phenomena ranging from macroscopic phases to microscopic states. This indicates that exotic behaviors can be observed in distinctive structures. A chiral structure, lacking both inversion and mirror symmetry, is the ultimate realization of such a unique system. Recent vibrant research has uncovered remarkable phenomena linked to structural chirality, e.g., chirality-induced spin selectivity (CISS) and magnetochiral anisotropy [1–7]. Their exotic electronic functionalities offer new avenues for advanced electronics and quantum devices.

Conversely, a complementary line of research based on the opposite perspective has recently emerged: leveraging the functionalities to engineer chiral structures from achiral precursors [8–13]. Namely, a desirable chiral

structure could be induced from an achiral crystal by some external means. Phonons in chiral crystals, so-called chiral phonons, acquire left-handed (LH) or right-handed (RH) circular polarization depending on the chirality of the crystal, since phonons are tightly interlinked with the entire structure [14–20]. Therefore, for example, structural chirality has been revealed to arise by breaking the compensation of phonon handedness, which is inherently degenerate in the parent achiral phase [10–12, 21]. These approaches to achiral-to-chiral phase transitions would provide key insights into the ubiquitous formation process of chiral structures in nature, as well as of chiral inorganic crystals [22–26].

The structural chirality affects the constituents and vice versa, which have been demonstrated independently so far. This raises a fundamental question: Can the interplay between structural chirality and its constituents trigger novel cooperative phenomena? If so, such phenomena could foster both practical advancements and fundamental insights. In conventional crystals, the Peierls transition serves as a classical example arising from the cooperation of the electrons and the lattice structure [27–30]. The essence of Peierls transitions embodies both elements, giving rise to the charge density wave (CDW) and the lattice deformation simultaneously. Extending this concept to chiral materials, where a unique structure and exotic electronic behaviors coexist, will suggest the potential for entirely novel phenomena. Nevertheless, studies on chirality in the Peierls transition have been confined to achiral-to-chiral phase transitions; accordingly, the above question remains unresolved.

Here, we address this question and predict a novel spontaneous phase transition dubbed the chirality-induced spin-selective Peierls transition (CISSPT). We focus on the case where the parent phase is a chiral metal and consider electron-phonon coupling (EPC) under a screw symmetry. Then, we demonstrate the Kohn anomaly of chiral phonons renormalized by electrons, which reveals that the nesting vector involves not merely the linear momentum but also the phonon angular momentum (AM). As a result, a spin-selective Peierls gap is introduced in the electronic band, regardless of whether the original band is spin degenerate or not. Furthermore, we explore the electronic order, lattice distortion, and collective excitation associated with CISSPT.

Formulations

Although realistic materials are three-dimensional, some materials are highly conductive only in a certain direction, the so-called quasi-one-dimensional (quasi-1D) con-

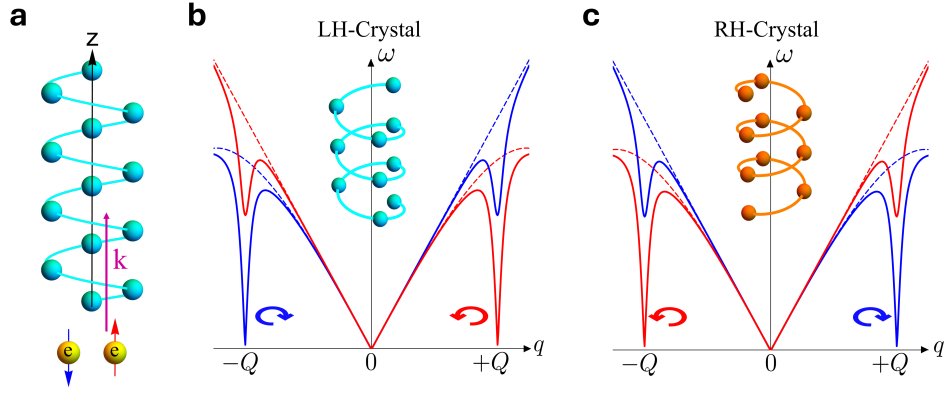


FIG. 1. **Kohn anomaly in chiral quasi-1D conductors.** **a**, An illustration of chiral quasi-1D conductors. The electrons are assumed to be highly conductive along the direction of the chiral axis. The global spin quantization axis is aligned with the z -axis. The figure shows a crystal with the three-fold screw symmetry as an example. **b**, Schematic plots of TA phonon dispersions in the LH crystal. The dotted lines are the frequencies at high temperatures, while the solid lines are those just above the transition temperature. The red (blue) lines denote the branch with phonon AM $l_z^{\text{ph}} = +1$ (-1). **c**, Same as **b**, but for the RH crystal. Note that the correspondence between the handedness of phonon AM and that of crystals is material-dependent, but they have a one-to-one correspondence in general.

ductors. We here focus on chiral inorganic or organic conductors with a helical structure, i.e., belonging to chiral space groups. In the main text, as an example, we consider quasi-1D systems with three-fold screw symmetry \hat{S}_3 . As depicted in Fig. 1a, we set the z -axis along the chiral axis and assume that the electrons are highly anisotropic to this direction, which is treated as a 1D electron system. Nevertheless, the three-dimensional features of the electrons are incorporated into the electron pseudo-angular momentum (see Supplementary Note 1).

Chirality, including static and dynamical properties, can be defined by the electric toroidal monopole G_0 , which consists of time-reversal (\mathcal{T})-even pseudoscalars [31–33]. The energy dispersion of truly chiral phonons splits due to the structural chirality during propagation along the chiral axis. The phonon frequency $\omega_{q,\lambda}$, where q is the wave vector along the z -axis and $\lambda = \pm$ is the handedness of the anti-clockwise/clockwise-circularly polarized phonon, satisfies the relations $\omega_{q,\lambda} \neq \omega_{-q,\lambda}$ and $\omega_{q,\lambda} = \omega_{-q,-\lambda}$ [17–20]. The former denotes the inversion (\mathcal{P}) symmetry breaking, while the latter is due to the preservation of the \mathcal{T} symmetry.

We here consider the longitudinal acoustic (LA) mode and transverse acoustic (TA) modes. The index of these modes is labeled $\eta = (\text{L}, +, -)$ [$\bar{\eta} = (\text{L}, -, +)$] in a unified manner. The TA modes possess phonon AM $l_{z,\pm}^{\text{ph}} = \pm 1$ at each q , while the LA mode does not. The displacement vector is written in the continuum limit as

$$\begin{aligned} \mathbf{u}(\mathbf{r}) &= \sum_{q,\eta} \sqrt{\frac{\hbar}{2N_i M_i \omega_{q,\eta}}} \boldsymbol{\epsilon}_{q,\eta} (\hat{b}_{q,\eta} + \hat{b}_{-q,\bar{\eta}}^\dagger) e^{iqz} \\ &\equiv \frac{1}{\sqrt{N_i}} \sum_{q,\eta} \boldsymbol{\epsilon}_{q,\eta} \hat{\zeta}_{q,\eta} e^{iqz}, \end{aligned} \quad (1)$$

where $\hat{b}_{q,\eta}$ ($\hat{b}_{q,\eta}^\dagger$) is the phonon annihilation (creation) operator, $\hat{\zeta}_{q,\eta}$ is the phonon field operator, and M_i is the mass of ions. Polarization vectors are defined as $\boldsymbol{\epsilon}_{q,L} = (0, 0, 1)^T$ and $\boldsymbol{\epsilon}_{q,\lambda} = \frac{1}{\sqrt{2}}(1, \lambda i, 0)^T$.

In the conventional Peierls transition, only the LA phonon is considered based on the basic EPC. However, in previous research [21], the EPC for the LA mode and the TA modes was derived using the Bir-Pikus formalism [34], where rotational symmetry imposes selection rules on the EPC for both LA and TA phonons. Here, we extend this concept to our system in the presence of the screw symmetry. The minimal EPC Hamiltonian for each mode is given by (see details in Methods 1-3)

$$\hat{H}_{\text{ep}}^{(\text{L})} = \frac{1}{\sqrt{N_i}} \sum_q i q g_L \hat{S}_{-q}^{(0)} \hat{\zeta}_{q,L}, \quad (2)$$

$$\hat{H}_{\text{ep}}^{(\text{T})} = \frac{1}{\sqrt{N_i}} \sum_q i q g_T [\hat{S}_{-q}^{(+)} \hat{\zeta}_{q,+} + \hat{S}_{-q}^{(-)} \hat{\zeta}_{q,-}], \quad (3)$$

where g_L and g_T denote the coupling constants and $\hat{S}_{-q}^{(X)} = \sum_{k,s,s'} \hat{c}_{k+q,s}^\dagger (\hat{\sigma}_X)_{ss'} \hat{c}_{k,s}$ [$X = 0, z, \pm$] indicates the density wave operator, with electron momentum k , spin $s = \uparrow, \downarrow$, and Pauli matrices $\hat{\sigma}_X$. The global spin quantization axis is chosen along the z -axis. The screw symmetry gives the selection rule on the EPC $s = s' + l_{z,\lambda}^{\text{ph}}$ for TA phonons $\hat{H}_{\text{ep}}^{(\text{T})}$ and $s = s'$ for LA phonons $\hat{H}_{\text{ep}}^{(\text{L})}$.

We begin with the following total Hamiltonian, which includes the electron and phonon parts: $\hat{H} = \hat{H}_{\text{el}} + \hat{H}_{\text{ph}} + \hat{H}_{\text{ep}}$. The EPC part is given by $\hat{H}_{\text{ep}} = \hat{H}_{\text{ep}}^{(\text{L})} + \hat{H}_{\text{ep}}^{(\text{T})}$. To capture the essential role of chiral phonons, we assume spin-degenerate electronic bands: $\hat{H}_{\text{el}} = \sum_{k,s} \xi_{k,s} \hat{c}_{k,s}^\dagger \hat{c}_{k,s}$, where $\xi_{k,s} = \hbar^2 k^2 / 2m_e - \varepsilon_{\text{F}}$ is the electron dispersion measured from the Fermi level within the parabolic approximation.

Kohn anomaly of chiral phonons

We first discuss the renormalization of chiral phonons by the EPC, a phenomenon commonly referred to as the Kohn anomaly. This effect leads to the softening of the relevant phonon branch in 1D systems. The renormalized phonon frequencies for each branch are given by (Methods 4)

$$\hbar\tilde{\omega}_{q,L} = \hbar\omega_{q,L} \sqrt{1 - \frac{2g_L^2 q^2}{M_i \omega_{q,L}^2} \mathcal{L}(q, 0)}, \quad (4)$$

$$\hbar\tilde{\omega}_{q,\lambda} = \hbar\omega_{q,\lambda} \sqrt{1 - \frac{4g_T^2 q^2}{M_i \omega_{q,\lambda}^2} \mathcal{L}(q, 0)} \quad [\lambda = \pm], \quad (5)$$

where $\mathcal{L}(q, \omega)$ is the Lindhard function. At low temperatures, the logarithmic singularity of $\mathcal{L}(q, 0)$ drives $\tilde{\omega}_q$ to zero at $q = \pm Q$, where $Q = 2k_F$ is twice the Fermi momentum. Thus, the transition temperature of the individual mode is calculated as

$$k_B T^{(\text{LA})} = \frac{2e^\gamma}{\pi} \varepsilon_F \exp\left(-\frac{M_i \omega_{Q,L}^2}{4k_F^2 g_L^2 D(\varepsilon_F)}\right), \quad (6)$$

$$k_B T_\lambda^{(\text{TA})} = \frac{2e^\gamma}{\pi} \varepsilon_F \exp\left(-\frac{M_i \omega_{Q,\lambda}^2}{8k_F^2 g_T^2 D(\varepsilon_F)}\right) \quad [\lambda = \pm], \quad (7)$$

with the Euler constant γ and the density of states at the Fermi level $D(\varepsilon_F)$. By comparing these transition temperatures, the realized phase can be inferred. When $T^{(\text{LA})} > \max\{T_+^{(\text{TA})}, T_-^{(\text{TA})}\}$, the predominant freezing of the LA mode leads to the conventional Peierls transition. In the other cases, the TA chiral phonons are preferentially frozen, and we hereafter focus on the latter case.

Furthermore, the inequivalence between $T_+^{(\text{TA})}$ and $T_-^{(\text{TA})}$ results in a handedness-dependent phonon softening. According to Eq. (7), the chiral phonon mode with the lowest frequency softens. Therefore, the soft mode is a time-reversal pair of the modes, (Q, λ) and $(-Q, -\lambda)$. Figures 1b and 1c show schematic illustrations of phonon dispersion at $T_+^{(\text{TA})}$ in LH crystals and at $T_-^{(\text{TA})}$ in RH crystals, respectively. These figures highlight the one-to-one correspondence between the handedness of the soft phonon λ and that of the parent chiral crystal, defined by χ .

Spin-selective Peierls transition

Owing to this handedness-dependent signature, the properties of phonon AM $l_{z,\pm}^{\text{ph}}$ as well as the linear momentum Q are embedded in the soft mode. This information is subsequently transferred to the electron system through the EPC, giving rise to CISSPT. We mainly focus on the case of incommensurate Q , where the lattice constant c and the wavelength $l_{\text{DW}} = 2\pi/Q$ form an irrational fraction. Throughout the main text, we consider a case with soft modes $(Q, +)$ and $(-Q, -)$ without loss of generality.

Within the mean-field approximation, the Hamiltonian

related to the electronic states becomes

$$\hat{H}_{\text{el}}^{\text{MF}} = \sum_{k>0} \hat{C}_k^\dagger \mathbf{H}_k \hat{C}_k, \quad (8)$$

$$\hat{C}_k^\dagger \equiv \begin{bmatrix} \hat{c}_{k,\uparrow}^\dagger & \hat{c}_{k-Q,\downarrow}^\dagger & \hat{c}_{k,\downarrow}^\dagger & \hat{c}_{k-Q,\uparrow}^\dagger \end{bmatrix}, \quad (9)$$

$$\mathbf{H}_k \equiv \begin{bmatrix} \xi_{k,\uparrow} & \Delta & 0 & 0 \\ \Delta^* & \xi_{k-Q,\downarrow} & 0 & 0 \\ 0 & 0 & \xi_{k,\downarrow} & 0 \\ 0 & 0 & 0 & \xi_{k-Q,\uparrow} \end{bmatrix}, \quad (10)$$

where $\Delta = 2iQg_T \langle \hat{\zeta}_{Q,+} \rangle / \sqrt{N_i}$ is defined as the order parameter. Unlike the conventional Peierls transition, electronic states with opposite spins connected by the wave number Q are coupled according to the selection rule $s = s' + l_{z,\lambda}^{\text{ph}}$ for the EPC. Moreover, this selection rule forbids other spin-flip processes, thereby enforcing the spin-selective gap, shown in Figs. 2a and 2b. We adopt the term ‘‘spin-selective Peierls transition’’ following previous research [35], but note that, in contrast to their analogical usage, the CISSPT formulated here denotes a qualitatively distinct phenomenon in the rigorous physical sense. Along with this spin-selective gap, only the off-diagonal components in spin space $\langle \hat{S}_{-Q}^{(+)} \rangle$ ($= \langle \hat{S}_{-Q}^{(-)*} \rangle$) take finite values, whereas only diagonal components $\langle \hat{S}_{-Q}^{(0)} \rangle$ or $\langle \hat{S}_{-Q}^{(z)} \rangle$ become non-zero in conventional CDW or spin density wave (SDW) orders. As a result, the itinerant electrons themselves compose a helical SDW, shown in Fig. 2c. In CISSPT, the chiral phonon acts as a helical Overhauser field [35, 36], and the helical SDW is represented in real space by

$$\delta \mathbf{S}(\mathbf{r}) = \frac{|\Delta|}{2\pi\hbar v_F \Lambda} \begin{bmatrix} \cos(Qz + \phi) \\ -\sin(Qz + \phi) \\ 0 \end{bmatrix}, \quad (11)$$

where $|\Delta|$ and ϕ denote the amplitude and phase of the order parameter, respectively, and Λ is the dimensionless EPC constant (Supplementary Note 2).

At the same time, the crystal undergoes a structural phase transition, and a chiral lattice distortion arises, as shown in Fig. 2d. Due to the non-zero thermal average $\langle \hat{\zeta}_{Q,+} \rangle$, the periodicity of the daughter phase is modulated in quadrature:

$$\delta \mathbf{u}(\mathbf{r}) = \frac{|\Delta|}{\sqrt{2}Qg_T} \begin{bmatrix} \cos(Qz + \phi - \pi/2) \\ -\sin(Qz + \phi - \pi/2) \\ 0 \end{bmatrix}. \quad (12)$$

Therefore, the lattice positions shift from the original \mathbf{R}_0 to $\mathbf{R} = \mathbf{R}_0 + \delta \mathbf{u}(\mathbf{R}_0)$ and, as a consequence, the screw symmetry is broken. The handedness of $\delta \mathbf{S}(\mathbf{r})$ and $\delta \mathbf{u}(\mathbf{r})$ is inverted in the opposite enantiomorph.

The above discussion can be straightforwardly extended to systems with spin-split electronic bands. For instance, when the spin-orbit coupling (SOC) is included in the electron Hamiltonian $\xi_{k,s} = \hbar^2 k^2 / 2m_e +$

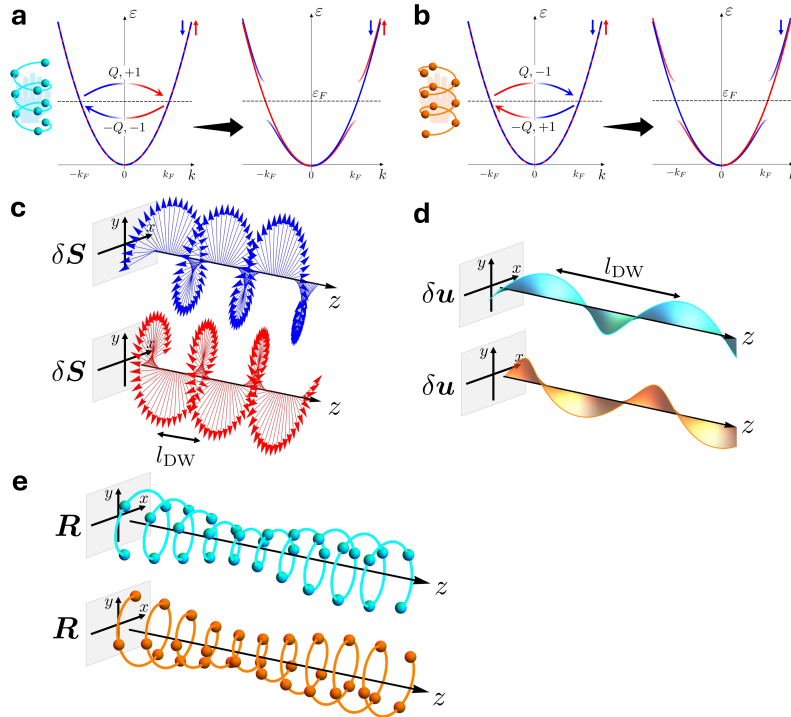


FIG. 2. **Incommensurate chirality-induced spin-selective Peierls transition.** **a**, The spin-selective gap in the electronic energy band in the LH crystal. Even if the energy band is spin degenerate above the transition temperature (left panel), spin-selective gap opens (right panel). The red-blue gradient arrows represent nesting vectors encompassing phonon AM. **b**, The same figure as **a**, but in the RH crystal. **c**, The helical SDW in the LH (top) and RH (bottom) crystals with $l_{\text{DW}} = 2\pi/Q = \pi/k_{\text{F}}$ denoting the wavelength of the CISSPT. Note that this figure shows illustration in real space. **d**, The chiral lattice distortion due to the CISSPT in the LH (top) and RH (bottom) crystals. **e**, The entire crystal geometry $\mathbf{R}_0 + \delta\mathbf{u}(\mathbf{R}_0)$ below the transition temperature in the LH (top) and RH (bottom) crystals.

$\alpha_{\text{SO}}k(\delta_z)_{ss} - \epsilon_{\text{F}}$, the same results are obtained by treating the system as spin subbands (Extended Data Fig. 2). This framework remains applicable to various forms of SOC, provided that spin remains a well-defined quantum number at the Fermi level [37]. Furthermore, correlation effects are known to stabilize this spin-selective gap [35].

Note that the spin-selective gap is forbidden when Q is commensurate. In this case, the nesting vectors $(Q, +)$ and $(Q, -)$ coexist in the same electronic state, and the two spin sectors couple identically, resulting in apparently conventional Peierls gaps. See more details in Supplementary Note 2.

Predicted experimental signatures

While the identification of materials hosting CISSPT remains an open challenge for future work, the underlying theoretical framework allows us to infer its universal experimental hallmarks. Here, we discuss the signatures in a material-independent manner, highlighting characteristic phononic and electronic responses arising from the intrinsic chiral lattice instability (for considerations on material classes and order estimation, see Methods 5).

CISSPT can be experimentally identified through characteristic phononic and electronic signatures. Inelastic neutron scattering or inelastic X-ray scattering measure-

ments can detect soft phonon modes in acoustic branches at a finite wave vector Q [38]. Notably, the degree of softening differs between left- and right-handed polarizations in CISSPT. Thus, polarization-resolved measurements, if accessible, can provide complementary signatures of chiral phonon dynamics [39], serving as pivotal evidence of the chiral lattice origin of the instability.

As for the electronic properties, a characteristic halving of conductance is anticipated below the transition temperature [35, 36, 40]. Furthermore, the helical SDW can be examined via elastic neutron scattering or nuclear magnetic resonance techniques and so on [28], while spin- and angle-resolved photoemission spectroscopy can further verify spin-selective gap formation [41]. Another key test is whether the wave vector Q changes systematically with carrier doping, in contrast to conventional helimagnets governed by the spin-orbit interaction.

A defining feature of CISSPT is the momentum-space consistency between the soft mode, the density wave, and the lattice modulation, all rooted in the same nesting instability. Detecting such correlations, alongside evidence of phonon AM, would offer compelling evidence for a chirality-driven mechanism fundamentally distinct from spin-orbit-based scenarios [42, 43]. These signatures to-

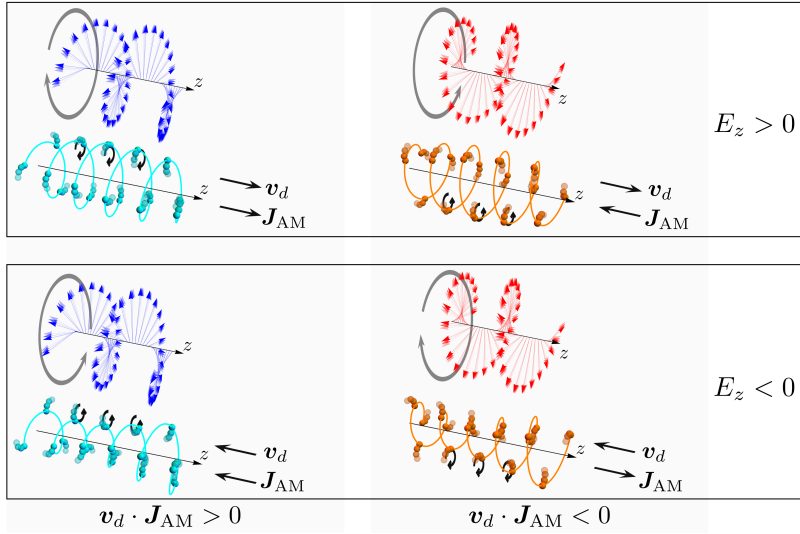


FIG. 3. **Sliding motions and the mechanical angular momentum transport under external electric field.** The upper panels show the sliding motion of the helical SDW and the accompanying lattice distortion under an electric field parallel to the z -axis, while the lower panels show the case of the opposite field direction. The left and right columns correspond to the LH and RH crystals, respectively. Here, $\mathbf{v}_d = v_d \mathbf{e}_z$ denotes the sliding velocity associated with the temporal evolution of the phase, and \mathbf{J}_{AM} represents the mechanical angular momentum induced by the sliding. The gray circular arrows indicate the rotational direction of the helical SDW entailed by the translational sliding motion, while the black circular arrows represent the local circular motion of the lattice displacements.

gether form a coherent experimental framework for identifying CISSPT and distinguishing it from conventional itinerant helimagnets.

Chiral sliding motions

Finally, we discuss the collective dynamics that reflect the distinctive nature of the CISSPT. The primary excitations are phase (phason) and amplitude (amplitudon) fluctuations of the density wave; the former being the Goldstone mode underlying the sliding motion. The energy dispersion of each mode takes the same form as in conventional CDWs (Supplementary Note 3):

$$\Omega_P^2(q) = \frac{m_e}{m_e^*} v_F^2 q^2, \quad (13)$$

$$\Omega_A^2(q) = \Lambda \omega_{Q,+}^2 + \frac{1}{3} \frac{m_e}{m_e^*} v_F^2 q^2, \quad (14)$$

$$m_e^* \equiv m_e \left(1 + \frac{4|\Delta|^2}{\Lambda(\hbar\omega_{Q,+})^2} \right), \quad (15)$$

for the phason (P) and amplitudon (A). These behaviours arise from the coupling between electrons and chiral phonons, indicating that, unlike conventional SDWs [30], the sliding mode of the density wave entails the circular motion of ordered ions. It is also emphasized that the nature of the sliding mode is different from that of conventional CDWs [27], since the CISSPT forms a helical SDW.

Under a static driving force such as a dc electric field E_z , the phase of the density wave ϕ evolves over time and generates a drift velocity $v_d = Q^{-1} \partial\phi/\partial t \propto E_z$,

which drives the sliding conduction. Without pinning, the sliding helical SDW pumps charge and spin supercurrent along the chiral axis [44]. Even in the presence of pinning by impurities or defects in realistic materials, sliding can occur above a threshold field. Alongside, the structural change of atomic positions \mathbf{R} transports mechanical AM on a macroscopic scale (see Methods 6):

$$\langle \mathbf{J}_{AM} \rangle = - \frac{|\Delta|^2 M_i N_i}{2Q^2 g_T^2} \langle \dot{\phi} \rangle \mathbf{e}_z, \quad (16)$$

where $\langle \dots \rangle$ means the temporal average. This mechanical AM superficially resembles that of chiral phonons since both involve circular ionic motions. However, unlike chiral phonons, the AM can be transported directly by an electric field. This is because the electric field directly induces a phase evolution of the helical SDW, thereby dragging the associated ordered state of lattice displacement. This mechanism renders the transport electrically switchable, providing direct control via an applied field and opening a route to harness angular momentum as a robust carrier for information and actuation beyond excitation-driven phononics.

Figure 3 illustrates the direction of sliding velocity $\langle \mathbf{v}_d \rangle$ and AM $\langle \mathbf{J}_{AM} \rangle$ depending on the handedness of crystals and the sign of the external electric field. These patterns can be classified from a multipole perspective by defining the pseudo-scalar $\mathbf{v}_d \cdot \mathbf{J}_{AM}$, enabling a unified understanding of the response handedness in a similar manner to the handedness of static orders (Methods 7) [32].

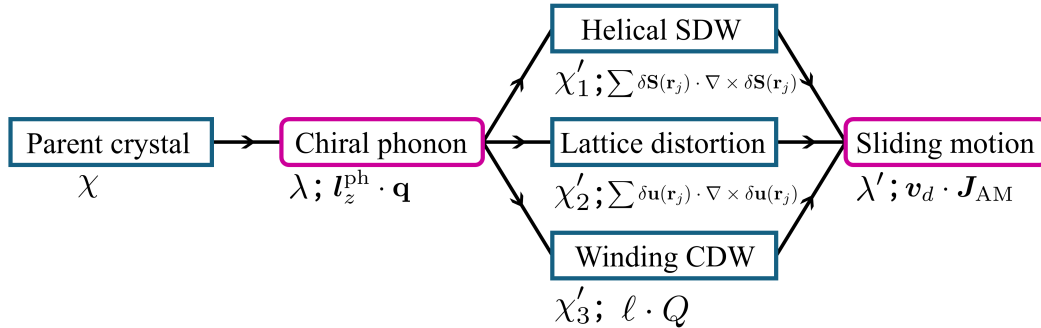


FIG. 4. **Flowchart representing the cyclic conversion of chirality.** Starting from the handedness of parental crystals, each physical quantity exhibits chiral signatures. The navy rectangles represent static chirality while purple rounded rectangles represent dynamical chirality. The black arrow indicates the process by which chirality is sequentially determined. Every Greek letter and pseudo scalar are shown in Methods 7. For a winding CDW, see Supplementary Note 4.

Beyond dc driving, the application of an ac field can trigger unique interference phenomena. When the external field frequency ω_{ac} is near the characteristic pinning frequency, the phase shift is locked to $\langle \dot{\phi} \rangle = n\omega_{ac}$, where n is an integer. Consequently, the AM $\langle \mathbf{J}_{AM} \rangle$ that is proportional to $\langle \dot{\phi} \rangle$ is also locked to integer multiples in sliding mode, as well as the electric and spin current. This phenomenon is expected to be observed as plateaux, so-called Shapiro steps on the angular momentum-voltage characteristics [45, 46].

Conclusions and Perspectives

We have demonstrated a spontaneous structural phase transition unique to chiral crystals, driven by the mutual coupling between electrons and chiral phonons. The CIS-SPT constitutes a family of the transverse Peierls transition [12, 21, 47]. Unlike in Ref. [21], where an imbalance of electronic spin states induces the soft mode with a specific phonon AM, in CISSPT, the intrinsic splitting of chiral phonons plays a central role and enables transferring the phonon AM to the electronic system. The material conditions assumed in this work are realized in many chiral chain conductors and chiral metals (for material relevance and order estimations, see Methods 5). Moreover, our formulation predicts other electronic orders; an alternative instability where the electronic spin is conserved, but the orbital component is not conserved. In this case, a winding CDW order emerges, whose helical modulation wraps around the chiral axis. Details of this complementary scenario are provided in Supplementary Note 4.

The CISSPT is qualitatively different from the CISS effect, which persists over a wide temperature range. Nonetheless, the spin-selective Peierls gap also provides ideal platforms for the optimized spin-filtering effect and the remarkable spin response [35, 40, 48]. Furthermore, our mechanism—helical SDW stabilized by chiral lattice dynamics—offers a new possibility for the emergence of itinerant helimagnets in structurally chiral materials

such as MnSi [49], providing an alternative to conventional scenarios. This may also open up opportunities for chirality-induced electromagnetic coupling, supporting the development of multiferroic functionalities in itinerant systems.

From a broader perspective, physical mechanisms such as the CISS effect are currently being explored as a potential origin of biomolecular homochirality [1, 2, 22, 23, 50]. These studies highlight that the interplay between electrons and structural chirality may have far-reaching implications beyond condensed matter physics. In our results, a cyclic conversion of chirality emerges between the electronic and lattice subsystems (shown in Fig. 4 and Methods 7), offering a pathway by which structural chirality can dictate electronic ordering—and conversely, how microscopic quantum interactions could give rise to macroscopic asymmetry. Our findings may thus represent a key missing piece of the puzzle in chirality-driven phenomena in physics and beyond.

Acknowledgments

The authors are grateful to R. Sano and K. Hara for fruitful discussions. This work was supported by JSPS KAKENHI (Grant Numbers 25KJ1482, JP22H01181, JP22H04933, JP23K22452, JP23K17353, JP24K21530, JP24H00007, JP25H01249).

Code availability

All relevant data are available on reasonable request.

Ethics declarations

Competing interests. The authors declare no competing interests.

Author contributions

S.A. conceived the original idea and performed all theoretical analyses. Y.Y. supervised the project. All authors discussed the results and contributed to the writing of the manuscript.

- * asano.shun.57x@st.kyoto-u.ac.jp
 † yanase@scphys.kyoto-u.ac.jp
- [1] Naaman, R., Paltiel, Y. & Waldeck, D. H. Chiral induced spin selectivity and its implications for biological functions. *Annual Review of Biophysics* **51**, 99–114 (2022). URL <https://www.annualreviews.org/content/journals/10.1146/annurev-biophys-083021-070400>.
 - [2] Bloom, B. P., Paltiel, Y., Naaman, R. & Waldeck, D. H. Chiral induced spin selectivity. *Chemical Reviews* **124**, 1950–1991 (2024). URL <https://doi.org/10.1021/acs.chemrev.3c00661>.
 - [3] Rikken, G. L. J. A. & Raupach, E. Enantioselective magnetochiral photochemistry. *Nature* **405**, 932–935 (2000). URL <https://doi.org/10.1038/35016043>.
 - [4] Nagaosa, N. & Yanase, Y. Nonreciprocal transport and optical phenomena in quantum materials. *Annual Review of Condensed Matter Physics* **15**, 63–83 (2024). URL <https://www.annualreviews.org/content/journals/10.1146/annurev-conmatphys-032822-033734>.
 - [5] Yan, B. Structural chirality and electronic chirality in quantum materials. *Annual Review of Materials Research* **54**, 97–115 (2024). URL <https://www.annualreviews.org/content/journals/10.1146/annurev-matsci-080222-033548>.
 - [6] Yang, S.-H., Naaman, R., Paltiel, Y. & Parkin, S. P. Chiral spintronics. *Nature Reviews Physics* **3**, 328–343 (2021). URL <https://doi.org/10.1038/s42254-021-00302-9>.
 - [7] Inui, A. et al. Chirality-induced spin-polarized state of a chiral crystal CrNb_3S_6 . *Phys. Rev. Lett.* **124**, 166602 (2020). URL <https://link.aps.org/doi/10.1103/PhysRevLett.124.166602>.
 - [8] Bousquet, E. et al. Structural chirality and related properties in periodic inorganic solids: review and perspectives. *Journal of Physics: Condensed Matter* **37**, 163004 (2025). URL <https://dx.doi.org/10.1088/1361-648X/adb674>.
 - [9] Hayashida, T., Kimura, K. & Kimura, T. Switching crystallographic chirality in $\text{Ba}(\text{TiO})\text{Cu}_4(\text{PO}_4)_4$ by laser irradiation. *The Journal of Physical Chemistry Letters* **13**, 3857–3862 (2022). URL <https://doi.org/10.1021/acs.jpcllett.2c00606>.
 - [10] Romao, C. P. & Juraschek, D. M. Phonon-induced geometric chirality. *ACS Nano* **18**, 29550–29557 (2024). URL <https://doi.org/10.1021/acsnano.4c05978>.
 - [11] Zeng, Z. et al. Photo-induced chirality in a nonchiral crystal. *Science* **387**, 431–436 (2025). URL <https://www.science.org/doi/abs/10.1126/science.adr4713>.
 - [12] Zhang, S., Luo, K. & Zhang, T. Understanding chiral charge-density wave by frozen chiral phonon. *npj Computational Materials* **10**, 264 (2024). URL <https://doi.org/10.1038/s41524-024-01440-1>.
 - [13] Fava, M., Romero, A. H. & Bousquet, E. Handedness selection and hysteresis of chiral orders in crystals. *Phys. Rev. Lett.* **135**, 146102 (2025). URL <https://link.aps.org/doi/10.1103/c4v9-nd4b>.
 - [14] Zhang, L. & Niu, Q. Angular momentum of phonons and the einstein-de haas effect. *Phys. Rev. Lett.* **112**, 085503 (2014). URL <https://link.aps.org/doi/10.1103/PhysRevLett.112.085503>.
 - [15] Zhu, H. et al. Observation of chiral phonons. *Science* **359**, 579–582 (2018). URL <https://www.science.org/doi/abs/10.1126/science.aar2711>.
 - [16] Wang, T., Sun, H., Li, X. & Zhang, L. Chiral phonons: Prediction, verification, and application. *Nano Letters* **24**, 4311–4318 (2024). URL <https://doi.org/10.1021/acs.nanolett.4c00606>.
 - [17] Ishito, K. et al. Truly chiral phonons in α -hgs. *Nature Physics* **19**, 35–39 (2023). URL <https://doi.org/10.1038/s41567-022-01790-x>.
 - [18] Ueda, H. et al. Chiral phonons in quartz probed by x-rays. *Nature* **618**, 946–950 (2023). URL <https://doi.org/10.1038/s41586-023-06016-5>.
 - [19] Chen, H. et al. Chiral phonon diode effect in chiral crystals. *Nano Letters* **22**, 1688–1693 (2022). URL <https://doi.org/10.1021/acs.nanolett.1c04705>.
 - [20] Kishine, J., Ovchinnikov, A. S. & Tereshchenko, A. A. Chirality-induced phonon dispersion in a noncentrosymmetric micropolar crystal. *Phys. Rev. Lett.* **125**, 245302 (2020). URL <https://link.aps.org/doi/10.1103/PhysRevLett.125.245302>.
 - [21] Luo, K. & Dai, X. Transverse peierls transition. *Phys. Rev. X* **13**, 011027 (2023). URL <https://link.aps.org/doi/10.1103/PhysRevX.13.011027>.
 - [22] Budin, I. & Szostak, J. W. Expanding roles for diverse physical phenomena during the origin of life. *Annual Review of Biophysics* **39**, 245–263 (2010). URL <https://www.annualreviews.org/content/journals/10.1146/annurev.biophys.050708.133753>.
 - [23] Michaeli, K., Kantor-Uriel, N., Naaman, R. & Waldeck, D. H. The electron’s spin and molecular chirality – how are they related and how do they affect life processes? *Chem. Soc. Rev.* **45**, 6478–6487 (2016). URL <http://dx.doi.org/10.1039/C6CS00369A>.
 - [24] Viedma, C. Chiral symmetry breaking during crystallization: Complete chiral purity induced by nonlinear autocatalysis and recycling. *Phys. Rev. Lett.* **94**, 065504 (2005). URL <https://link.aps.org/doi/10.1103/PhysRevLett.94.065504>.
 - [25] Bailey, J. et al. Circular polarization in star-formation regions: Implications for biomolecular homochirality. *Science* **281**, 672–674 (1998). URL <https://www.science.org/doi/abs/10.1126/science.281.5377.672>.
 - [26] Takano, Y., Ichi Takahashi, J., Kaneko, T., Marumo, K. & Kobayashi, K. Asymmetric synthesis of amino acid precursors in interstellar complex organics by circularly polarized light. *Earth and Planetary Science Letters* **254**, 106–114 (2007). URL <https://www.sciencedirect.com/science/article/pii/S0012821X06008399>.
 - [27] Grüner, G. The dynamics of charge-density waves. *Rev. Mod. Phys.* **60**, 1129–1181 (1988). URL <https://link.aps.org/doi/10.1103/RevModPhys.60.1129>.
 - [28] Grüner, G. *Density Waves In Solids* (CRC Press, 1994), 1st edn.
 - [29] Monceau, P. Electronic crystals: an experimental overview. *Advances in Physics* **61**, 325–581 (2012). URL <https://doi.org/10.1080/00018732.2012.719674>.
 - [30] Grüner, G. The dynamics of spin-density waves. *Rev. Mod. Phys.* **66**, 1–24 (1994). URL <https://link.aps.org/doi/10.1103/RevModPhys.66.1>.
 - [31] Barron, L. D. *Molecular Light Scattering and Optical Activity*

- (Cambridge University Press, 2004), 2 edn.
- [32] Kusunose, H., Kishine, J.-i. & Yamamoto, H. M. Emergence of chirality from electron spins, physical fields, and material-field composites. *Applied Physics Letters* **124**, 260501 (2024). URL <https://doi.org/10.1063/5.0214919>.
- [33] Oiwa, R. & Kusunose, H. Rotation, electric-field responses, and absolute enantioselection in chiral crystals. *Phys. Rev. Lett.* **129**, 116401 (2022). URL <https://link.aps.org/doi/10.1103/PhysRevLett.129.116401>.
- [34] Bir, G. L. & Pikus, G. E. *Symmetry and strain-induced effects in semiconductors* (Wiley, 1974). URL <https://cir.nii.ac.jp/crid/1130282270775839488>.
- [35] Braunecker, B., Japaridze, G. I., Klinovaja, J. & Loss, D. Spin-selective peierls transition in interacting one-dimensional conductors with spin-orbit interaction. *Phys. Rev. B* **82**, 045127 (2010). URL <https://link.aps.org/doi/10.1103/PhysRevB.82.045127>.
- [36] Overhauser, A. W. Giant spin density waves. *Phys. Rev. Lett.* **4**, 462–465 (1960). URL <https://link.aps.org/doi/10.1103/PhysRevLett.4.462>.
- [37] Meng, T. & Loss, D. Helical nuclear spin order in two-subband quantum wires. *Phys. Rev. B* **87**, 235427 (2013). URL <https://link.aps.org/doi/10.1103/PhysRevB.87.235427>.
- [38] Hippert, F., Geissler, E., Hodeau, J., Lelièvre-Berna, E. & Regnard, J. *Neutron and X-ray Spectroscopy* (2005).
- [39] Wang, T., Zhou, J., Ren, Q. & Zhang, L. Inelastic neutron scattering for direct detection of chiral phonons (2025). URL <https://arxiv.org/abs/2507.20168>.
- [40] Braunecker, B., Simon, P. & Loss, D. Nuclear magnetism and electronic order in ^{13}C nanotubes. *Phys. Rev. Lett.* **102**, 116403 (2009). URL <https://link.aps.org/doi/10.1103/PhysRevLett.102.116403>.
- [41] Sobota, J. A., He, Y. & Shen, Z.-X. Angle-resolved photoemission studies of quantum materials. *Rev. Mod. Phys.* **93**, 025006 (2021). URL <https://link.aps.org/doi/10.1103/RevModPhys.93.025006>.
- [42] Togawa, Y., Kousaka, Y., Inoue, K. & Kishine, J.-i. Symmetry, structure, and dynamics of monoaxial chiral magnets. *Journal of the Physical Society of Japan* **85**, 112001 (2016). URL <https://doi.org/10.7566/JPSJ.85.112001>.
- [43] Ishikawa, Y., Tajima, K., Bloch, D. & Roth, M. Helical spin structure in manganese silicide mnsi. *Solid State Communications* **19**, 525–528 (1976). URL <https://www.sciencedirect.com/science/article/pii/0038109876900570>.
- [44] Kurebayashi, D., Liu, Y., Masell, J. & Nagaosa, N. Theory of charge and spin pumping in atomic-scale spiral magnets. *Phys. Rev. B* **106**, 205110 (2022). URL <https://link.aps.org/doi/10.1103/PhysRevB.106.205110>.
- [45] Kriza, G., Quirion, G., Traetteberg, O., Kang, W. & Jérôme, D. Shapiro interference in a spin-density-wave system. *Phys. Rev. Lett.* **66**, 1922–1925 (1991). URL <https://link.aps.org/doi/10.1103/PhysRevLett.66.1922>.
- [46] Nikitin, M. V., Zybtev, S. G., Pokrovskii, V. Y. & Loginov, B. A. Mechanically induced shapiro steps: Enormous effect of vibrations on the charge-density wave transport. *Applied Physics Letters* **118**, 223105 (2021). URL <https://doi.org/10.1063/5.0051436>.
- [47] Yang, F. Z. et al. Incommensurate transverse peierls transition and signature of chiral charge density wave in EuAl_4 . *Nature Communications* **16**, 10401 (2025). URL <https://doi.org/10.1038/s41467-025-65374-y>.
- [48] Li, T. et al. Observation of a helical luttinger liquid in InAs/GaSb quantum spin hall edges. *Phys. Rev. Lett.* **115**, 136804 (2015). URL <https://link.aps.org/doi/10.1103/PhysRevLett.115.136804>.
- [49] Stishov, S. M. & Petrova, A. E. Itinerant helimagnet mnsi. *Physics-Uspekhi* **54**, 1117 (2011). URL <https://doi.org/10.3367/UFNe.0181.201111b.1157>.
- [50] Ozturk, S. F. & Sasselov, D. D. On the origins of life’s homochirality: Inducing enantiomeric excess with spin-polarized electrons. *Proceedings of the National Academy of Sciences* **119**, e2204765119 (2022). URL <https://www.pnas.org/doi/10.1073/pnas.2204765119>.
- [51] Valentín-Pérez, Á., Rosa, P., Hillard, E. A. & Giorgi, M. Chirality determination in crystals. *Chirality* **34**, 163–181 (2022). URL <https://onlinelibrary.wiley.com/doi/abs/10.1002/chir.23377>.
- [52] Ni, B. & Cölfen, H. Chirality communications between inorganic and organic compounds. *SmartMat* **2**, 17–32 (2021). URL <https://onlinelibrary.wiley.com/doi/abs/10.1002/smm2.1021>.
- [53] Fecher, G. H., Kübler, J. & Felser, C. Chirality in the solid state: Chiral crystal structures in chiral and achiral space groups. *Materials* **15** (2022). URL <https://www.mdpi.com/1996-1944/15/17/5812>.
- [54] Zhang, L. & Niu, Q. Chiral phonons at high-symmetry points in monolayer hexagonal lattices. *Phys. Rev. Lett.* **115**, 115502 (2015). URL <https://link.aps.org/doi/10.1103/PhysRevLett.115.115502>.
- [55] Zhang, T. & Murakami, S. Chiral phonons and pseudoangular momentum in nonsymmorphic systems. *Phys. Rev. Res.* **4**, L012024 (2022). URL <https://link.aps.org/doi/10.1103/PhysRevResearch.4.L012024>.
- [56] Chen, H., Wu, W., Zhu, J., Yang, S. A. & Zhang, L. Propagating chiral phonons in three-dimensional materials. *Nano Letters* **21**, 3060–3065 (2021). URL <https://doi.org/10.1021/acs.nanolett.1c00236>.
- [57] Yang, Y. et al. Catalogue of chiral phonon materials (2025). URL <https://arxiv.org/abs/2506.13721>.
- [58] Zhang, S. et al. Comprehensive study of phonon chirality under symmetry constraints (2025). URL <https://arxiv.org/abs/2503.22794>.
- [59] Juraschek, D. M. et al. Chiral phonons. *Nature Physics* **21**, 1532–1540 (2025). URL <https://doi.org/10.1038/s41567-025-03001-9>.
- [60] Buda, A. B., der Heyde, T. A. & Mislow, K. On quantifying chirality. *Angewandte Chemie International Edition in English* **31**, 989–1007 (1992). URL <https://onlinelibrary.wiley.com/doi/abs/10.1002/anie.199209891>.
- [61] Ayuso, D., Ordonez, A. F. & Smirnova, O. Ultrafast chirality: the road to efficient chiral measurements. *Phys. Chem. Chem. Phys.* **24**, 26962–26991 (2022). URL <http://dx.doi.org/10.1039/D2CP01009G>.
- [62] Gómez-Ortiz, F., Fava, M., McCabe, E. E., Romero, A. H. & Bousquet, E. Structural chirality measurements and computation of handedness in periodic solids. *Phys. Rev. B* **110**, 174112 (2024). URL <https://link.aps.org/doi/10.1103/PhysRevB.110.174112>.

- [aps.org/doi/10.1103/PhysRevB.110.174112](https://doi.org/10.1103/PhysRevB.110.174112).
- [63] Streib, S. Difference between angular momentum and pseudoangular momentum. *Phys. Rev. B* **103**, L100409 (2021). URL <https://link.aps.org/doi/10.1103/PhysRevB.103.L100409>.
- [64] Božović, I. Possible band-structure shapes of quasi-one-dimensional solids. *Phys. Rev. B* **29**, 6586–6599 (1984). URL <https://link.aps.org/doi/10.1103/PhysRevB.29.6586>.
- [65] Božović, I. B., Delhalle, J. & Damnjanović, M. A posteriori symmetry analysis of polymer electronic band structures. *International Journal of Quantum Chemistry* **20**, 1143–1163 (1981). URL <https://onlinelibrary.wiley.com/doi/abs/10.1002/qua.560200602>.
- [66] Wang, X., Xian, Y. & Yan, Y. Chiral electrons and spin selectivity at chiral-achiral interfaces (2024). URL <https://arxiv.org/abs/2306.01664>. 2306.01664.
- [67] Tateishi, T., Kato, A. & Kishine, J.-i. Electron–chiral phonon coupling, crystal angular momentum, and phonon chirality. *Journal of the Physical Society of Japan* **94**, 053601 (2025). URL <https://doi.org/10.7566/JPSJ.94.053601>.
- [68] Kato, A. & Kishine, J.-i. Note on angular momentum of phonons in chiral crystals. *Journal of the Physical Society of Japan* **92**, 075002 (2023). URL <https://doi.org/10.7566/JPSJ.92.075002>.
- [69] Tsunetsugu, H. & Kusunose, H. Theory of energy dispersion of chiral phonons. *Journal of the Physical Society of Japan* **92**, 023601 (2023). URL <https://doi.org/10.7566/JPSJ.92.023601>.
- [70] Fransson, J. Chiral phonon induced spin polarization. *Phys. Rev. Res.* **5**, L022039 (2023). URL <https://link.aps.org/doi/10.1103/PhysRevResearch.5.L022039>.
- [71] Garanin, D. A. & Chudnovsky, E. M. Angular momentum in spin-phonon processes. *Phys. Rev. B* **92**, 024421 (2015). URL <https://link.aps.org/doi/10.1103/PhysRevB.92.024421>.
- [72] Vittmann, C., Lim, J., Tamascelli, D., Huelga, S. F. & Plenio, M. B. Spin-dependent momentum conservation of electron–phonon scattering in chirality-induced spin selectivity. *The Journal of Physical Chemistry Letters* **14**, 340–346 (2023). URL <https://doi.org/10.1021/acs.jpcllett.2c03224>. PMID: 36625481.
- [73] Fransson, J. Vibrational origin of exchange splitting and ”chiral-induced spin selectivity. *Phys. Rev. B* **102**, 235416 (2020). URL <https://link.aps.org/doi/10.1103/PhysRevB.102.235416>.
- [74] Funato, T., Matsuo, M. & Kato, T. Chirality-induced phonon-spin conversion at an interface. *Phys. Rev. Lett.* **132**, 236201 (2024). URL <https://link.aps.org/doi/10.1103/PhysRevLett.132.236201>.
- [75] Sano, R. & Kato, T. Chirality-induced spin selectivity by variable-range hopping along dna double helix (2024). URL <https://arxiv.org/abs/2404.19000>. 2404.19000.
- [76] Nakajima, R. et al. Giant spin polarization and a pair of antiparallel spins in a chiral superconductor. *Nature* **613**, 479–484 (2023). URL <https://doi.org/10.1038/s41586-022-05589-x>.
- [77] Nakajima, R., Pop, F. & Avarvari, N. Superconductors with structural chirality. *J. Mater. Chem. C* **12**, 12207–12217 (2024). URL <http://dx.doi.org/10.1039/D4TC01719F>.
- [78] Hara, K. & Yanase, Y. Spin supercurrent in parity-mixed superconductors with structural chirality. *Communications Physics* **8**, 389 (2025). URL <https://doi.org/10.1038/s42005-025-02295-8>.
- [79] Sato, T., Goto, H. & Yamamoto, H. M. Sturdy spin-momentum locking in a chiral organic superconductor. *Phys. Rev. Res.* **7**, 023056 (2025). URL <https://link.aps.org/doi/10.1103/PhysRevResearch.7.023056>.
- [80] Qin, F. et al. Superconductivity in a chiral nanotube. *Nature Communications* **8**, 14465 (2017). URL <https://doi.org/10.1038/ncomms14465>.
- [81] Takagi, R. et al. Square and rhombic lattices of magnetic skyrmions in a centrosymmetric binary compound. *Nature Communications* **13**, 1472 (2022). URL <https://doi.org/10.1038/s41467-022-29131-9>.
- [82] Miao, H. et al. Spontaneous chirality flipping in an orthogonal spin-charge ordered topological magnet. *Phys. Rev. X* **14**, 011053 (2024). URL <https://link.aps.org/doi/10.1103/PhysRevX.14.011053>.
- [83] Wang, L.-L., Nepal, N. K. & Canfield, P. C. Origin of charge density wave in topological semimetals SrAl_4 and eAl_4 . *Communications Physics* **7**, 111 (2024). URL <https://doi.org/10.1038/s42005-024-01600-1>.
- [84] Ramakrishnan, S. et al. Noncentrosymmetric, transverse structural modulation in SrAl_4 , and elucidation of its origin in the BaAl_4 family of compounds. *Phys. Rev. Res.* **6**, 023277 (2024). URL <https://link.aps.org/doi/10.1103/PhysRevResearch.6.023277>.
- [85] Zhang, T. et al. Weyl phonons in chiral crystals. *Nano Letters* **23**, 7561–7567 (2023). URL <https://doi.org/10.1021/acs.nanolett.3c02132>.
- [86] Zhang, H. et al. Measurement of phonon angular momentum. *Nature Physics* **21**, 1387–1391 (2025). URL <https://doi.org/10.1038/s41567-025-02952-3>.
- [87] Peng, H., Hou, D. & Chen, G. Quasi-one-dimensional thermal transport in trigonal selenium crystal. *Journal of Physics: Condensed Matter* **33**, 455402 (2021). URL <https://doi.org/10.1088/1361-648X/ac1d15>.
- [88] Hirayama, M., Okugawa, R., Ishibashi, S., Murakami, S. & Miyake, T. Weyl node and spin texture in trigonal tellurium and selenium. *Phys. Rev. Lett.* **114**, 206401 (2015). URL <https://link.aps.org/doi/10.1103/PhysRevLett.114.206401>.
- [89] Wessely, O., Skubic, B. & Nordström, L. Current driven magnetization dynamics in helical spin density waves. *Phys. Rev. Lett.* **96**, 256601 (2006). URL <https://link.aps.org/doi/10.1103/PhysRevLett.96.256601>.
- [90] Katsura, H., Nagaosa, N. & Balatsky, A. V. Spin current and magnetoelectric effect in noncollinear magnets. *Phys. Rev. Lett.* **95**, 057205 (2005). URL <https://link.aps.org/doi/10.1103/PhysRevLett.95.057205>.
- [91] Katsura, H., Balatsky, A. V. & Nagaosa, N. Dynamical magnetoelectric coupling in helical magnets. *Phys. Rev. Lett.* **98**, 027203 (2007). URL <https://link.aps.org/doi/10.1103/PhysRevLett.98.027203>.
- [92] Hamada, M., Minamitani, E., Hirayama, M. & Murakami, S. Phonon angular momentum induced by the temperature gradient. *Phys. Rev. Lett.* **121**, 175301 (2018). URL <https://link.aps.org/doi/10.1103/PhysRevLett.121.175301>.
- [93] Kishine, J.-i., Kusunose, H. & Yamamoto, H. M. On the definition of chirality and enantioselective

fields. *Israel Journal of Chemistry* **62**, e202200049 (2022). URL <https://onlinelibrary.wiley.com/doi/abs/10.1002/ijch.202200049>.

- [94] Edelstein, V. Spin polarization of conduction electrons induced by electric current in two-dimensional asymmetric electron systems. *Solid State Communications* **73**, 233–235 (1990). URL <https://www.sciencedirect.com/science/article/pii/003810989090963C>.
- [95] Edelstein, V. M. Magnetoelectric effect in polar superconductors. *Phys. Rev. Lett.* **75**, 2004–2007 (1995). URL <https://link.aps.org/doi/10.1103/PhysRevLett.75.2004>.
- [96] Yoda, T., Yokoyama, T. & Murakami, S. Orbital edelstein effect as a condensed-matter analog of solenoids. *Nano Letters* **18**, 916–920 (2018). URL <https://doi.org/10.1021/acs.nanolett.7b04300>.

Methods

1. Notes on the considered system

In this study, we focus on materials belonging to nonsym-morphic chiral space groups. Such materials are characterized by the absence of improper rotations and the existence of screw symmetry [51–53]. The former property, the absence of improper rotations, is a strict definition of structural chirality and causes phonon band splitting depending on LH or RH polarization [14–20, 54–59]. On the other hand, the latter property, the existence of screw symmetry, is essential for the following selection rule of the EPC.

In the main text, we consider a single helix for simplicity, and impose \hat{S}_3 screw symmetry, i.e., the pseudo-angular momentum l_{PAM} described below is $0, \pm 1$. There is no unified definition for handedness of the structures, including inorganic crystals [60–62]. Therefore, we define right-handed crystals as those in which the atoms are arranged counter-clockwise along the helix, and left-handed crystals as those with opposite helix. This definition merely serves to distinguish between RH and LH crystals. We show the LH crystal with the symmetry of the Line group $L3_1$ in Fig. 1a as an example. Throughout this article, the LH chiral structure is represented by light blue color, and the RH chiral structure by light orange color.

2. Pseudo-angular momenta in chiral crystals

We summarize the features of the pseudo- (or crystal-) angular momentum (PAM). For more details, see Supplementary Note 1.

In chiral materials without improper rotations, PAM plays an analogous role to angular momentum in rotationally symmetric crystals [17, 55, 63–67]: while crystal rotation conserves angular momentum, screw symmetry conserves PAM, just as crystal momentum is conserved in a periodic lattice.

For electronic states with crystal momentum $\mathbf{k} =$

$(0, 0, k)$, the eigenvalue under \hat{S}_n is

$$\begin{aligned}\hat{S}_n \psi_{\mathbf{k}} &= \lambda_{S_n}^{(\text{el})} \psi_{\mathbf{k}}, \\ \lambda_{S_n}^{(\text{el})} &= \exp\left(-i\frac{kc}{n} - i\frac{2\pi}{n}l_{\text{PAM,el}}\right),\end{aligned}$$

where $l_{\text{PAM,el}}$ is defined modulo n and decomposes into orbital and spin contributions:

$$l_{\text{PAM,el}} = m_{\mathbf{k}}^{(\text{orb})} + m_{\mathbf{k}}^{(\text{spin})}.$$

Here, $m^{(\text{orb})}$ reflects the azimuthal phase winding of the Bloch wave function, while $m^{(\text{spin})}$ comes from the $\text{SU}(2)$ spin rotation:

$$\hat{U}_{\text{spin}}(C_n) |\sigma\rangle = \exp\left(-i\frac{2\pi}{n}m_{\mathbf{k}}^{(\text{spin})}\right) |\sigma\rangle.$$

Importantly, regardless of the presence of SOC, electron PAM remains a half-integer conserved quantity, reflecting the combined effect of orbital and spin rotations under screw symmetry [64, 66]. Neglecting the electronic SOC, it reduces to $l_{\text{PAM,el}} = l + 1/2$ ($l \in \mathbb{Z}$).

Similarly, the phonon PAM is defined as the eigenvalue of \hat{S}_n acting on the polarization vector:

$$\hat{S}_n \mathbf{u}_{\mathbf{q}}(\mathbf{r}) = \exp\left(-i\frac{qc}{n} - i\frac{2\pi}{n}l_{\text{PAM,ph}}^s\right) \mathbf{u}_{\mathbf{q}}(\mathbf{r}),$$

with $l_{\text{PAM,ph}}^s \in \mathbb{Z}_n$ representing the spin part of the phonon PAM. Although PAM differs from the angular momentum, it transforms similarly under time reversal: $\hat{\mathcal{T}}^{-1}l_{\text{PAM}}(\mathbf{k})\hat{\mathcal{T}} = -l_{\text{PAM}}(-\mathbf{k})$.

The phase factors $\exp(-ikc/n)$ and $\exp(-iqc/n)$ arise from the translational part of \hat{S}_n ; in most cases, they cancel, allowing them to be ignored. Therefore, in systems with screw symmetry, the total PAM is conserved in any interaction that commutes with \hat{S}_n ; $\hat{S}_n^{-1}\hat{H}_{\text{int}}\hat{S}_n = \hat{H}_{\text{int}}$. For example, the selection rule for the electron-phonon coupling leads to

$$l_{\text{PAM,el}} + l_{\text{PAM,ph}}^s = l_{\text{PAM,el}} \pmod{n}. \quad (17)$$

In the main text, for simplicity, we equate the phonon angular momentum l_z^{ph} with the phonon PAM and completely separate the longitudinal and transverse modes (Supplementary Note 1). This can be justified by the fact that they agree with each other in the long-wavelength to medium-wavelength region [68, 69].

3. Details of the electron-phonon coupling

Our minimal electron-phonon coupling is in the form of (Supplementary Note 1)

$$\begin{aligned}\hat{H}_{\text{ep}}^{(\text{L})} &= \frac{1}{\sqrt{N}} \sum_{k,q} \sum_{s,s',m_{\text{orb}},m'_{\text{orb}}} i q g L \hat{c}_{k+q,s,m_{\text{orb}}}^\dagger \hat{c}_{k,s',m'_{\text{orb}}} \\ &\quad \times \hat{\zeta}_{q,L} \delta_{m_{\text{orb}}+s,m'_{\text{orb}}+s'}, \\ \hat{H}_{\text{ep}}^{(\text{T})} &= \frac{1}{\sqrt{N}} \sum_{k,q} \sum_{s,s',m_{\text{orb}},m'_{\text{orb}}} \sum_{\lambda=\pm} i q g T \hat{c}_{k+q,s,m_{\text{orb}}}^\dagger \hat{c}_{k,s',m'_{\text{orb}}} \\ &\quad \times \hat{\zeta}_{q,\lambda} \delta_{m_{\text{orb}}+s,m'_{\text{orb}}+s'+l_{z,\lambda}^{\text{ph}}},\end{aligned}$$

where m_{orb} is the orbital contribution of the electron PAM (the aforementioned $m^{(\text{orb})}$), s is the electron spin, and $l_{z,\lambda}^{\text{ph}}$ is the phonon angular momentum. The above equations include both the real-space orbital and spin contributions of the electron PAM. Therefore, we will discuss further in order to extract essential phenomena and derive minimal models.

One possibility is to assume that the spatial part m_{orb} is invariant between the initial and final states. This assumption leads to the following simple form:

$$\begin{aligned}\hat{H}_{\text{ep}}^{(\text{L})} &= \frac{1}{\sqrt{N}} \sum_{k,q,s,s'} i q g_L \hat{c}_{k+q,s}^\dagger \hat{c}_{k,s'} \hat{\zeta}_{q,L} \delta_{s,s'}, \\ \hat{H}_{\text{ep}}^{(\text{T})} &= \frac{1}{\sqrt{N}} \sum_{k,q,s,s'} \sum_{\lambda=\pm} i q g_T \hat{c}_{k+q,s}^\dagger \hat{c}_{k,s'} \hat{\zeta}_{q,\lambda} \delta_{s,s'+l_{z,\lambda}^{\text{ph}}},\end{aligned}$$

where we omit the index of m_{orb} . The spin-selective Peierls states can arise from this EPC, and we mainly discuss this type of EPC.

On the other hand, an alternative approach is to assume that the electron spin s is invariant. In this case, the electronic states with the same spin are coupled [67], and we have

$$\begin{aligned}\hat{H}_{\text{ep}}^{(\text{L})} &= \frac{1}{\sqrt{N}} \sum_{k,q,m_{\text{orb}},m'_{\text{orb}}} i q g_L \hat{c}_{k+q,m_{\text{orb}}}^\dagger \hat{c}_{k,m'_{\text{orb}}} \hat{\zeta}_{q,L} \delta_{m_{\text{orb}},m'_{\text{orb}}}, \\ \hat{H}_{\text{ep}}^{(\text{T})} &= \frac{1}{\sqrt{N}} \sum_{k,q,m_{\text{orb}},m'_{\text{orb}}} \sum_{\lambda=\pm} i q g_T \hat{c}_{k+q,m_{\text{orb}}}^\dagger \hat{c}_{k,m'_{\text{orb}}} \\ &\quad \times \hat{\zeta}_{q,\lambda} \delta_{m_{\text{orb}},m'_{\text{orb}}+l_{z,\lambda}^{\text{ph}}}.\end{aligned}$$

The transverse Peierls transition and a novel class of chiral CDW, dubbed winding CDW, can be induced by this type of EPC, as discussed in Supplementary Note 4.

Note that, in the context of electron-chiral phonon coupling [70–75], the EPC due to dynamical contributions such as spin-microrotation coupling has been discussed [74, 75]. However, such couplings are proportional to the phonon conjugate momentum $\hat{\pi}$ rather than to the phonon field operator $\hat{\zeta}$. Therefore, these mechanisms are not expected to make a major contribution to the structural phase transition.

4. Calculations of the renormalized chiral phonon

We here mention the way to calculate the renormalized phonon frequencies, are shown in the main text. The renormalized phonon frequency can be evaluated from the Feynman diagrams shown in Extended Data Fig. 1. When the electrons are spin degenerate, the phonon self-energy becomes (see Supplementary Note 2 for general

expressions and detailed calculations)

$$\begin{aligned}\Pi^{(\text{L})}(q, i\omega_m) &= \frac{g_L^2 q^2 \hbar}{2M_i \omega_{q,L}} \chi_{zz}^{(0)}(q, i\omega_m), \\ \Pi^{(\text{T})}(q, +, i\omega_m) &= \frac{2g_T^2 q^2 \hbar}{M_i \omega_{q,+}} \chi_{\uparrow\downarrow}^{(0)}(q, i\omega_m), \\ \Pi^{(\text{T})}(q, -, i\omega_m) &= \frac{2g_T^2 q^2 \hbar}{M_i \omega_{q,-}} \chi_{\uparrow\downarrow}^{(0)}(q, i\omega_m),\end{aligned}$$

where

$$\begin{aligned}\chi_{zz}^{(0)}(q, i\omega_m) &= \frac{k_B T}{N} \sum_{k, i\epsilon_n, s} \mathcal{G}_{ss}^{(0)}(k, i\epsilon_n) \mathcal{G}_{ss}^{(0)}(k-q, i\epsilon_n - i\omega_m), \\ \chi_{\uparrow\downarrow}^{(0)}(q, i\omega_m) &= \frac{k_B T}{N} \sum_{k, i\epsilon_n} \mathcal{G}_{\uparrow\uparrow}^{(0)}(k, i\epsilon_n) \mathcal{G}_{\downarrow\downarrow}^{(0)}(k-q, i\epsilon_n - i\omega_m), \\ \chi_{\downarrow\uparrow}^{(0)}(q, i\omega_m) &= \frac{k_B T}{N} \sum_{k, i\epsilon_n} \mathcal{G}_{\downarrow\downarrow}^{(0)}(k, i\epsilon_n) \mathcal{G}_{\uparrow\uparrow}^{(0)}(k-q, i\epsilon_n - i\omega_m).\end{aligned}$$

For spin-degenerate electrons, we have

$$\begin{aligned}\frac{1}{2} \chi_{zz}^{(0)}(q, i\omega_m) &= \chi_{\uparrow\downarrow}^{(0)}(q, i\omega_m) = \chi_{\downarrow\uparrow}^{(0)}(q, i\omega_m) \\ &= \frac{1}{N} \sum_k \frac{f(\varepsilon_{k-q}) - f(\varepsilon_k)}{i\omega_m + \varepsilon_{k-q} - \varepsilon_k}.\end{aligned}$$

Then, we perform the analytic continuation $i\omega_m \rightarrow \hbar\omega + i\delta$, and define the Lindhard function as

$$\mathcal{L}(q, \omega) \equiv \text{Re} \left[-\frac{1}{N} \sum_k \frac{f(\varepsilon_{k-q}) - f(\varepsilon_k)}{\hbar\omega + i\delta + \varepsilon_{k-q} - \varepsilon_k} \right]. \quad (18)$$

The renormalized phonon frequencies correspond to the poles of the renormalized phonon Green functions. Therefore, they are determined by the condition $\mathcal{D}_L^{-1}(q, \hbar\omega + i\delta) = 0$, $\mathcal{D}_T^{-1}(q, \lambda, \hbar\omega + i\delta) = 0$, which lead to

$$\begin{aligned}(\hbar\tilde{\omega}_{q,L})^2 &= (\hbar\omega_{q,L})^2 \left(1 - \frac{2g_L^2 q^2}{M_i \omega_{q,L}^2} \mathcal{L}(q, 0) \right), \\ (\hbar\tilde{\omega}_{q,\lambda})^2 &= (\hbar\omega_{q,\lambda})^2 \left(1 - \frac{4g_T^2 q^2}{M_i \omega_{q,\lambda}^2} \mathcal{L}(q, 0) \right).\end{aligned}$$

We assumed that the energy scale of phonons is sufficiently small relative to the Fermi energy, as usual.

As the temperature approaches zero, the Lindhard function diverges logarithmically to $+\infty$ with $q = \pm 2k_F$ in quasi-1D systems, resulting in the Kohn anomaly of phonons. Accordingly, the transition temperature of each mode follows from the condition $\tilde{\omega}_{Q,\eta} = 0$,

$$\begin{aligned}k_B T_{+}^{(\text{LA})} &= \frac{2e^\gamma}{\pi} \varepsilon_F \exp \left(-\frac{M_i \omega_{Q,L}^2}{4k_F^2 g_L^2 D(\varepsilon_F)} \right), \\ k_B T_{+}^{(\text{TA})} &= \frac{2e^\gamma}{\pi} \varepsilon_F \exp \left(-\frac{M_i \omega_{Q,+}^2}{8k_F^2 g_T^2 D(\varepsilon_F)} \right), \\ k_B T_{-}^{(\text{TA})} &= \frac{2e^\gamma}{\pi} \varepsilon_F \exp \left(-\frac{M_i \omega_{Q,-}^2}{8k_F^2 g_T^2 D(\varepsilon_F)} \right).\end{aligned}$$

As mentioned in the main text, when the conditional equation $T^{(\text{LA})} < \max\{T_+^{(\text{TA})}, T_-^{(\text{TA})}\}$ is satisfied, a softening of the transverse mode occurs, which triggers CISSPT. This condition can be specifically written as

$$\min\left\{\frac{\omega_{2k_F,+}}{g_T}, \frac{\omega_{2k_F,-}}{g_T}\right\} < \sqrt{2} \frac{\omega_{2k_F,L}}{g_L}. \quad (19)$$

5. Minimal requirements and material relevance

In this section, we summarize the general conditions under which CISSPT occurs and demonstrate whether the corresponding energy scales fall within experimentally realistic ranges, without invoking any specific material system. Here, we simply employ rough order estimation; therefore, the identification of specific material candidates and more quantitative calculations depend on future work. Based on the theoretical framework in this article, the minimal necessary conditions that must be satisfied for CISSPT are summarized as follows.

1. The parent crystal structure hosts structural chirality, lacking inversion and mirror symmetries, and screw symmetry along a well-defined axis.
2. The parent phase is a metal or organic conductor with itinerant carriers and Fermi surfaces. This is necessary because the Peierls instability requires electronic states at the Fermi level.
3. The electronic structure must provide substantial conduction along the chiral axis or exhibit Fermi-surface nesting with a wave vector Q parallel to the chiral axis; this requirement is not limited to quasi-1D systems.
4. The quantitative criterion derived in Eq. (19) holds: the softening transition temperature for transverse phonons must exceed that of longitudinal phonons, thereby guaranteeing that the transverse Peierls transition is preferentially realized.

To assess whether this instability is experimentally achievable, we perform a rough order estimation using representative rather than compound-specific parameters. We assume the acoustic branch of the transverse phonon at momentum $2k_F$ with energy $\hbar\omega_{Q,T} = 0.01$ eV, an effective ionic mass $M_i = 50$ u, together with $k_F = 1 \text{ \AA}^{-1}$, and an electronic density of states $D(\varepsilon_F) = 0.5$ states/(eV · spin · atom), which are employed as physically realistic scales.

Under these representative conditions, the transition temperature associated with the transverse Peierls instability ($\max\{T_+^{(\text{TA})}, T_-^{(\text{TA})}\}$) is given by

$$k_B T^{(\text{TA})} \simeq 1.13 \varepsilon_F \exp\left(-\frac{0.32}{g_T^2}\right),$$

where the unit for the coupling constant g_T is eV. Solving this relation for g_T yields

$$g_T(T^{(\text{TA})}; \varepsilon_F) = \sqrt{\frac{0.32}{\log(1.13 \varepsilon_F / (k_B T^{(\text{TA})}))}}.$$

To visualize the magnitude of the coupling required to stabilize the transverse Peierls instability, $T^{(\text{TA})}$ as a function of g_T was plotted for $\varepsilon_F = 1, 0.1, 0.01$ eV, as shown in Extended Data Fig. 3. Because such plots alone may obscure the scale between different regimes of $T^{(\text{TA})}$, we additionally tabulated the values of g_T required to obtain $T^{(\text{TA})} = 0.1, 1, 10, 100$ K for each ε_F . These values are provided in the Extended Data Table I. The figure and table clarify the range of EPC strengths necessary for CISSPT under experimentally relevant thermal conditions, and we can infer that the instability for CISSPT is achievable within a coupling constant regime comparable to that of realistic materials.

Next, to demonstrate that handedness-dependent phonon softening is sufficiently visible, we examine the ratio of the transition temperatures of CISSPT, $T_+^{(\text{TA})}/T_-^{(\text{TA})}$. We employ the same parameter set as above for the order estimation of $T^{(\text{TA})}$. Introducing chiral phonon splitting as $\omega_{Q,\pm} = \omega_{Q,T} \pm \delta\omega$, the ratio becomes

$$\frac{T_-^{(\text{TA})}}{T_+^{(\text{TA})}} = \exp\left[-\frac{0.64}{g_T^2} \frac{\delta\omega}{\omega_{Q,T}}\right]. \quad (20)$$

We evaluate this ratio for $g_T = 0.1\text{--}0.5$ eV and relative phonon splitting $\delta\omega/\omega_{Q,T} = 1\%$ and 10% . The results, summarized in Extended Data Tables II and III, show that even small frequency splitting leads to a sufficiently large difference in transition temperatures especially in the weak-coupling regime. This indicates that CISSPT naturally favours specific phonon chirality.

These considerations indicate that the Peierls instability driven by chiral phonons is plausible. Moreover, the observation of a transverse Peierls transition in an achiral crystal EuAl_4 suggests that candidate materials for CISSPT may be found in the future. Potential material classes span from chiral organic systems with screw symmetry, resembling κ -NCS compounds in structure and conduction [76–80], to metallic compounds hosting structural chirality, analogous to EuAl_4 [47, 81–84]. Elemental tellurium and selenium also provide relevant platforms hosting experimentally observed chiral phonons [19, 85–87]; although their natural forms are non-metallic, carrier doping or alloying that generates Fermi surfaces aligned with the chiral axis could render them viable candidates [88].

6. Sliding motion and the angular momentum

Since the itinerant electron system constitutes the helical SDW order, the phase of the order parameter is driven by

the electric field through the time evolution of the electronic momenta. Under a uniform electric field E_z , the electronic states obey $k = -eE_z/\hbar$, so that the mean-field coupling between $(k + Q/2, \uparrow)$ and $(k - Q/2, \downarrow)$ acquires a time-dependent phase. A unitary transformation eliminating this momentum shift shows that the Peierls gap takes the form $|\Delta|e^{i\phi(t)}$ with $\dot{\phi} = 2eE_z/(\hbar Q) \propto E_z$ in the absence of pinning effects [27–30]. Furthermore, the spin transfer torque induced by the current can also serve as a mechanism driving the phase. In any case, the time evolution of the phase ϕ is, at the lowest order, proportional to the electric field [89–91].

The mechanical AM generated by the sliding motion of the density wave is evaluated as follows [86, 92]:

$$\begin{aligned} \langle \mathbf{J}_{\text{AM}} \rangle &= M_1 \sum_j^{N_i} \langle \mathbf{R}_j \times \dot{\mathbf{R}}_j \rangle \\ &= M_1 \sum_j^{N_i} \langle \delta \mathbf{u}(\mathbf{R}_{0,j}) \times \delta \dot{\mathbf{u}}(\mathbf{R}_{0,j}) \rangle \\ &\quad + M_1 \sum_j^{N_i} \langle \mathbf{R}_{0,j} \times \delta \dot{\mathbf{u}}(\mathbf{R}_{0,j}) \rangle \\ &\simeq -\lambda \frac{|\Delta|^2 M_1 N_i}{2Q^2 g_T^2} \langle \dot{\phi} \rangle \mathbf{e}_z \quad [\lambda = \pm], \end{aligned} \quad (21)$$

where the second term $M_1 \sum \mathbf{R}_0 \times \delta \dot{\mathbf{u}} \propto \dot{\phi} \sin(\phi)$ is a rapidly oscillatory term with a zero time average, and is therefore assumed negligible. In the rigid density wave, the lattice distortion can be expressed as

$$\begin{aligned} \delta \mathbf{u}(\mathbf{r}) &= \frac{|\Delta|}{\sqrt{2}Qg_T} [\cos(Qz + \phi - \pi/2)\mathbf{e}_x \\ &\quad - \lambda \sin(Qz + \phi - \pi/2)\mathbf{e}_y]. \end{aligned}$$

Substituting this form into the above definition yields the last line of Eq. (21), showing that the expectation value of the mechanical AM is proportional to the time derivative of the phase ϕ and its direction is fixed by structural handedness λ . This establishes that phase evolution in the electronic subsystem induces macroscopic AM transport in the lattice subsystem, consistently carrying the same G_0 symmetry as discussed in the following Methods 7.

7. G_0 orders and cyclic conversion of chirality

Finally, we overview the chiral signatures that arise in this work using \mathcal{P} -odd, \mathcal{T} -even pseudo-scalars, i.e., the electric toroidal monopole G_0 as a unifying descriptor [32, 33, 93]. The key point of this section is that every physical quantity discussed in this article — whether it is a dynamical phonon quantity, static electronic orders, or a driven response — carries the same symmetry signature G_0 , and the sign of G_0 for each observable is fixed by the original structural handedness χ . Before proceeding to the concrete formulation, we summarize the relevant

quantities in the main text and Supplementary Note 4 and show the representative expressions for G_0 as follows [32, 33, 57, 58, 67, 93].

1. The parent crystals: χ
2. (Soft) chiral phonons: λ
phonon Zilch $\sum_j \mathbf{u}(\mathbf{r}_j) \cdot \nabla \times \mathbf{u}(\mathbf{r}_j)$,
phonon helicity $\mathbf{l}_z^{\text{ph}} \cdot \mathbf{q}$, etc.
3. Helical spin density waves: χ'_1
 $\sum_j \delta \mathbf{S}(\mathbf{r}_j) \cdot \nabla \times \delta \mathbf{S}(\mathbf{r}_j)$
4. Chiral lattice distortions: χ'_2
 $\sum_j \delta \mathbf{u}(\mathbf{r}_j) \cdot \nabla \times \delta \mathbf{u}(\mathbf{r}_j)$
5. Winding charge density waves: χ'_3
 $\ell \cdot \mathbf{Q}$
6. Chiral sliding motions: λ'
 $\mathbf{v}_d \cdot \mathbf{J}_{\text{AM}}$

Each Greek letter shall take a value of ± 1 according to their handedness.

As discussed in the main text, the handedness of the soft phonon modes λ has a one-to-one correspondence with the handedness χ of the parent crystal. The electronic band structure involved in the instability is \mathcal{T} -even and \mathcal{P} -odd, and the resulting helical SDW and chiral lattice distortion are therefore statically chiral in the same sense. In other words, the helical SDW (χ'_1) and the lattice distortion (χ'_2) inherit their handedness from the soft phonon and thus indirectly from χ . Note that although the helical SDW does not possess net \mathcal{T} symmetry, the \mathcal{T} operation merely shifts the helimagnetic ordering by half a period without altering the helical orientation itself, thus exhibiting G_0 characteristics [32]. The winding CDW, which is discussed in Supplementary Note 4, likewise appears in LH and RH forms depending on the sign of the soft phonon mode.

The sliding motion of the density wave under an applied electric field also reflects this handedness: when a static chiral order is present, driving the phase produces a drift of the density wave and an associated circular motion of ionic positions, which in turn carries a mechanical AM. The handedness of the driven response λ' follows directly from the handedness of the static orders $\chi'_1, \chi'_2, \chi'_3$ and hence from χ . In this way, the sliding response bears a striking resemblance to chiral phonons as it transports AM, but it differs in that the AM is produced and controlled electrically through the driven electronic order.

We remark that the pseudoscalar $\mathbf{v}_d \cdot \mathbf{J}_{\text{AM}}$ can be regarded as dynamical realization of G_0 . The drift velocity \mathbf{v}_d akin to the electric current transforms as \mathcal{P} -odd and \mathcal{T} -odd, the same symmetry as the magnetic toroidal dipole \mathbf{T} . The mechanical AM \mathbf{J}_{AM} is \mathcal{P} -even and \mathcal{T} -odd (the same as the magnetic dipole \mathbf{M}). Hence, there is a correspondence from the viewpoint of symmetry;

$G_0 \longleftrightarrow \mathbf{T} \cdot \mathbf{M}$. This observation reveals that the sliding motion is a \mathbf{T} - \mathbf{M} cross correlation that produces a dynamical G_0 , which is analogous to the Edelstein effect [94-96]. Nonetheless, they are microscopically different: in Edelstein effects, the electric current couples to electronic spin or orbital angular momentum, whereas the density wave pumps ionic mechanical angular momentum by the sliding motion.

In this manner, starting from the parent lattice handedness χ , the inherent phonon chirality determines the chirality of the electronic orders. When an electric field is applied and the electronic density wave is driven, the information of chirality carried by the electronic order is expressed again in a lattice response — the mechanical AM transport associated with the sliding motion. Figure 4 in the main text illustrates this flowchart. Thus, a series of phenomena discussed in this article can be regarded as a symmetry-preserving transfer of chirality information across lattice and electron subsystems: the phonon chirality is transferred into electronic chirality by the Peierls instability, and driven electronic dynamics feed back a chiral signature into the lattice subsystem. For brevity, we refer to this process as a cyclic conversion of chirality.

Extended Data

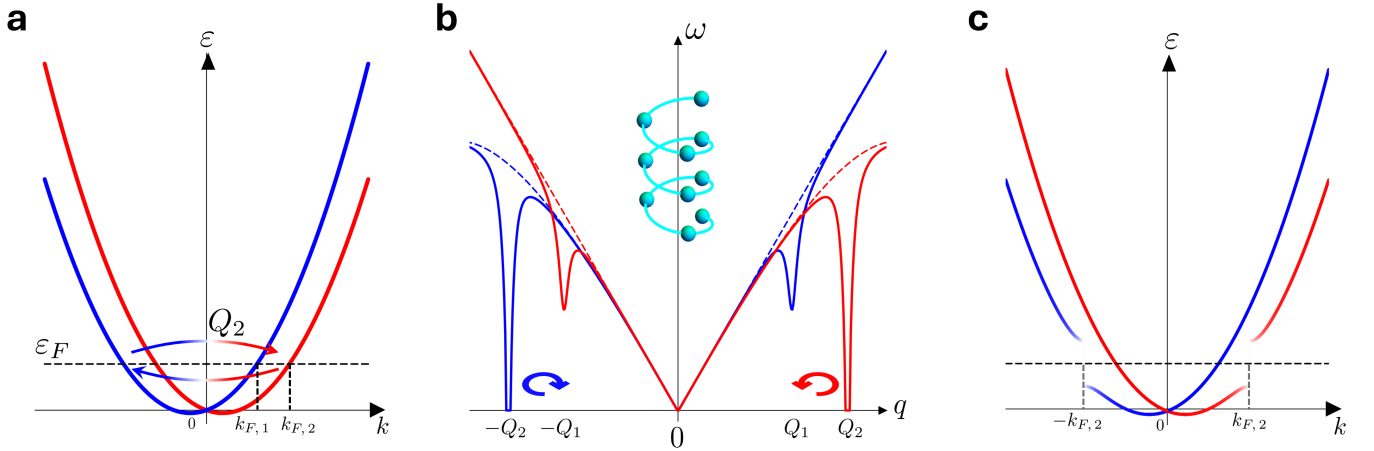
Longitudinal mode

$$\begin{aligned}
 \text{---} \circ \text{---} &= \text{---} \circ \text{---} + \text{---} \circ \text{---} \Pi^{(L)}(q, i\omega_m) \text{---} \circ \text{---} \\
 \text{---} \circ \text{---} &= \text{---} \circ \text{---} \Pi^{(L)}(q, i\omega_m) \text{---} \circ \text{---} \\
 \text{---} \circ \text{---} &= \text{---} \circ \text{---} \begin{matrix} \uparrow \\ k, i\epsilon_n \\ \downarrow \\ k - q, i\epsilon_n - i\omega_m \end{matrix} \text{---} \circ \text{---} = \chi_{zz}(q, i\omega_m)
 \end{aligned}$$

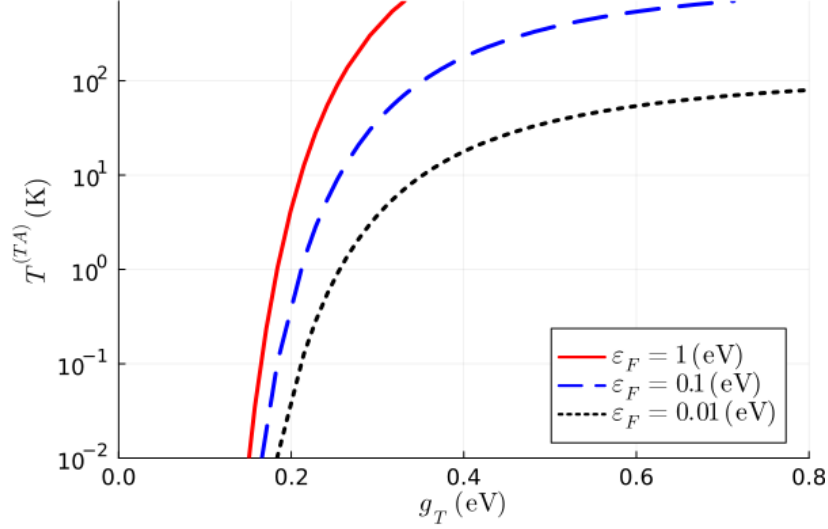
Transverse mode

$$\begin{aligned}
 \text{---} \times \text{---} &= \text{---} \times \text{---} + \text{---} \times \text{---} \Pi^{(T)}(q, \lambda, i\omega_m) \text{---} \times \text{---} \\
 \text{---} \times \text{---} &= \text{---} \times \text{---} \Pi^{(T)}(q, +, i\omega_m) \text{---} \times \text{---} \\
 \text{---} \times \text{---} &= \text{---} \times \text{---} \begin{matrix} \uparrow \\ k, i\epsilon_n \\ \downarrow \\ k - q, i\epsilon_n - i\omega_m \end{matrix} \text{---} \times \text{---} = \chi_{+-}(q, i\omega_m) \\
 \text{---} \times \text{---} &= \text{---} \times \text{---} \begin{matrix} \downarrow \\ k, i\epsilon_n \\ \uparrow \\ k - q, i\epsilon_n - i\omega_m \end{matrix} \text{---} \times \text{---} = \chi_{-+}(q, i\omega_m)
 \end{aligned}$$

Extended Data Figure 1. **Feynman diagram for the Dyson equation with the spin-degenerate electronic bands.** The upper (lower) panel shows the Dyson equation and the phonon self-energy within random phase approximation for the longitudinal (transverse) phonon mode. The black arrows indicate spin of electrons. The red circles represent the vertex part for $\hat{H}_{\text{ep}}^{(L)}$ while blue crosses for $\hat{H}_{\text{ep}}^{(T)}$.



Extended Data Figure 2. **Spin-selective Peierls states in the LH crystal with the electron spin-orbit coupling.** **a**, The electronic bands including the SOC Hamiltonian $\hat{H}_{\text{SOC}} = \alpha_{\text{SO}} \mathbf{k} \cdot \hat{\boldsymbol{\sigma}}$ with negative α_{SO} . The lift of spin-degeneracy produces distinct Fermi wave vectors $k_{F,1}$ and $k_{F,2}$. **b**, Schematic illustration of the phonon dispersion in the LH crystal at the transition temperature. Chiral phonon branches $\lambda = \pm 1$ exhibit Kohn anomalies at distinct wave vectors $Q_1 = 2k_{F,1}$ and $Q_2 = 2k_{F,2}$. **c**, The spin-selective Peierls gap below the transition temperature. The soft phonon Q_2 couples the electronic subbands with $(-k_{F,2}, \downarrow)$ and $(k_{F,2}, \uparrow)$, where $k_{F,2} = Q_2/2$. See more details in Supplementary Note 2.



Extended Data Figure 3. **Transition temperature of CISSPT as a function of the coupling constant.** Transition temperature evaluated from $k_B T^{(\text{TA})} = 1.13 \epsilon_F \exp(-0.32/g_T^2)$ is plotted against the transverse EPC constant g_T . Curves correspond to representative Fermi energies $\epsilon_F = 1, 0.1, 0.01$ eV, spanning typical conduction bandwidths in realistic systems.

ϵ_F (eV)	$T^{(\text{TA})}$ (K)	0.1	1	10	100
	0.01		0.21	0.26	0.35
0.1		0.18	0.21	0.26	0.35
1		0.16	0.18	0.21	0.26

Extended Data Table I: **Required electron phonon coupling constant for each transition temperature.** Values of the EPC strength for transverse phonons g_T (in eV) required to obtain $T^{(\text{TA})} = 0.1, 1, 10, \text{ and } 100$ K are listed for representative Fermi energies $\epsilon_F = 0.01, 0.1, \text{ and } 1$ eV. $T^{(\text{TA})} \equiv \max\{T_+^{(\text{TA})}, T_-^{(\text{TA})}\}$ means the transition temperature of CISSPT. The parameter set is the same as the Extended Data Fig. 3.

g_T (eV)	0.1	0.2	0.3	0.4	0.5
$T_+^{(\text{TA})}/T_-^{(\text{TA})}$	0.52	0.85	0.93	0.96	0.97

Extended Data Table II: **Ratio of transition temperatures for each phonon handedness $T_+^{(\text{TA})}/T_-^{(\text{TA})}$ with a 1% splitting in chiral phonon frequencies.** For each value of g_T , the ratio of transition temperatures is calculated based on Eq. (20) with $\delta\omega/\omega_{Q,T} = 0.01$. Here, we assume $T_+^{(\text{TA})} < T_-^{(\text{TA})}$, i.e., $\omega_{Q,+} < \omega_{Q,-}$, which corresponds to the situation being considered in the main text.

g_T (eV)	0.1	0.2	0.3	0.4	0.5
$T_+^{(\text{TA})}/T_-^{(\text{TA})}$	0.0016	0.20	0.49	0.67	0.77

Extended Data Table III: **Ratio of transition temperatures for each phonon handedness $T_+^{(\text{TA})}/T_-^{(\text{TA})}$ with 10% splitting in chiral phonon frequencies.** The same as Extended Data Table II, but with $\delta\omega/\omega_{Q,T} = 0.1$.

Supplementary Information for “Chirality-induced spin-selective Peierls transition”

Shun Asano^{1,*} and Youichi Yanase^{1,†}

¹*Department of Physics, Kyoto University, Kyoto 606-8502, Japan*

Table of contents in Supplementary Information

Supplementary Note 1. Details of the formulations

1. Definition of pseudo-angular momentum
2. Selection rule of pseudo-angular momentum
3. Bir-Pikus formalism
4. Pseudo-angular momenta in the electronic bands

Supplementary Note 2. Detailed calculations for CISSPT

1. Notation for Green functions
2. Calculation for the renormalized phonon frequency
3. The case with explicit spin-orbit couplings
4. Gap equation of the spin-selective Peierls states
5. Resultant orders in CISSPT
6. Commensurability effect in CISSPT

Supplementary Note 3. Derivation of collective excitations

1. Calculation of phason and amplitudon frequencies

Supplementary Note 4. On transverse Peierls transitions and chiral charge density waves

1. Transverse Peierls transitions in chiral crystals
2. Collective excitations and angular momentum flow
3. Coexistence of CISSPT and winding charge density wave
4. Extension to transverse Peierls transitions in achiral crystals

Reference

Supplementary Note 1. Details of the formulations.

In this Supplementary note, we explain the details of our formulation, which includes the characteristics of the pseudo-angular momentum (PAM) and the effective electron-phonon coupling (EPC). We here set $\hbar = 1$ and all the angular momenta and pseudo-angular momenta are expressed as integers or half-integers.

1. Definition of pseudo-angular momentum.

We consider a crystalline system preserving a n -fold screw symmetry $\hat{S}_n = [\hat{C}_n | \mathbf{c}/n]$ along the z -axis, where \hat{C}_n is a n -fold rotation around the z -axis and \mathbf{c} is a lattice vector along z . The Hamiltonian \hat{H} , \hat{S}_n , and the translation operator along the z -axis \hat{T}_c are all commutative:

$$[\hat{H}, \hat{S}_n] = [\hat{H}, \hat{T}_c] = [\hat{S}_n, \hat{T}_c] = 0.$$

Therefore, as far as the wave propagation along the z -axis is considered, $\hat{C}_n \mathbf{k} = \mathbf{k}$, etc., are satisfied, and the energy eigenstate can be chosen as an eigenstate of both \hat{S}_n and \hat{T}_c :

$$\hat{S}_n \psi_{\mathbf{k}} = \lambda_{S_n}^{(\text{el})} \psi_{\mathbf{k}},$$

where $\psi_{\mathbf{k}}$ is defined as symmetry-adapted Bloch eigenstates at crystal momentum $\mathbf{k} = (0, 0, k)$ and the irrelevant band indices are omitted for simplicity [1–4].

In spinless cases, from the property $\hat{S}_n^n = \hat{T}_c$, it follows that

$$\hat{S}_n^n \psi_{\mathbf{k}} = \exp(-ikc) \psi_{\mathbf{k}},$$

and, therefore,

$$\lambda_{S_n}^{(\text{el})} = \exp\left(-i\frac{kc}{n} - i\frac{2\pi}{n}l_{\text{PAM,el}}\right), \quad l_{\text{PAM,el}} \in \mathbb{Z}_n. \quad (\text{S.1})$$

The pseudo-angular momentum (PAM) $l_{\text{PAM,el}}$ is an integer modulo n , which is attributed to the rotation operator included in \hat{S}_n [3]. Therefore, in addition to the translational symmetry designating the crystal momentum, the eigenstates are characterized by the PAM under the screw symmetry.

In the same manner, when the degree of freedom of electron spins is included, each electronic band is labelled by the PAM $l_{\text{PAM,el}}$. However, since the rotation operator \hat{C}_n acts not only in real space but also in spin space, a double group is introduced to characterize the system, and $l_{\text{PAM,el}}$ becomes a half-integer [1]. Then, we construct the symmetry-adapted Bloch function categorized by $l_{\text{PAM,el}} \in \mathbb{Z}_n/2$ as

$$\psi_{\mathbf{k}, l_{\text{PAM}}}(\mathbf{r}) = \sum_{\sigma} e^{ikz} e^{im_{\mathbf{k}}^{(\text{orb})}\Phi} u_{\mathbf{k}, m^{(\text{orb})}, \sigma}(\rho, \Phi, z) |\sigma\rangle,$$

where $|\sigma\rangle$ denotes the spin state ($|\uparrow\rangle, |\downarrow\rangle$), Φ is the azimuthal angle within the xy plane, and $u_{\mathbf{k}, \sigma}(\mathbf{r}) = u_{\mathbf{k}, \sigma}(\rho, \Phi, z)$ is a periodic function with lattice periodicity, written in cylindrical coordinates:

$$u_{\mathbf{k}, \sigma}(\rho, \Phi - 2\pi/n, z - c/n) = u_{\mathbf{k}, \sigma}(\rho, \Phi, z).$$

Here, $m^{(\text{orb})}$ represents the phase factor that arises from the screw operator. Under this formulation, because the screw operator acts on both real space coordinates and spin, the wave function is transformed as

$$\begin{aligned} \hat{S}_n \psi_{\mathbf{k}, l_{\text{PAM}}}(\mathbf{r}) &= \sum_{\sigma\sigma'} e^{ik(z-c/n)} e^{im_{\mathbf{k}}^{(\text{orb})}(\Phi-2\pi/n)} u_{\mathbf{k}, \sigma}(\rho, \Phi - 2\pi/n, z - c/n) \left[\hat{U}_{\text{spin}}(C_n) \right]_{\sigma\sigma'} |\sigma'\rangle \\ &= e^{-ikc/n} e^{ikz} \sum_{\sigma\sigma'} e^{-2\pi im_{\mathbf{k}}^{(\text{orb})}/n} e^{im_{\mathbf{k}}^{(\text{orb})}\Phi} u_{\mathbf{k}, \sigma}(\rho, \Phi, z) \left[\hat{U}_{\text{spin}}(C_n) \right]_{\sigma\sigma'} |\sigma'\rangle \\ &= \sum_{\sigma} \exp\left(-i\frac{kc}{n} - i\frac{2\pi}{n}(m_{\mathbf{k}}^{(\text{orb})} + m_{\mathbf{k}}^{(\text{spin})})\right) e^{ikz} e^{im_{\mathbf{k}}^{(\text{orb})}\Phi} u_{\mathbf{k}, \sigma}(\rho, \Phi, z) |\sigma\rangle, \end{aligned}$$

where $\hat{U}_{\text{spin}}(C_n) = \exp(-i\frac{2\pi}{n}\frac{\sigma_z}{2})$ is the SU(2) spin rotation matrix corresponding to \hat{C}_n , and we used

$$\hat{U}_{\text{spin}}(C_n) |\sigma\rangle = e^{-i\frac{2\pi}{n}m_{\mathbf{k}}^{(\text{spin})}} |\sigma\rangle, \quad (\text{S.2})$$

with $m^{(\text{spin})} = \pm 1/2$ for $|\uparrow\rangle$ and $|\downarrow\rangle$, respectively. Therefore, the electron PAM can be decomposed into $m^{(\text{orb})}$ and $m^{(\text{spin})}$; the former originates from the real space coordinate dependence of the Bloch function and the latter from the spin space. In other words, the total electron PAM is generally preserved modulo n in each eigenstate:

$$l_{\text{PAM,el}} = m_{\mathbf{k}}^{(\text{orb})} + m_{\mathbf{k}}^{(\text{spin})}. \quad (\text{S.3})$$

In general, although their sum modulo n remains a good quantum number, $m^{(\text{orb})}$ and $m^{(\text{spin})}$ are not individually conserved. However, at wave vectors where the electronic spin is regarded a good quantum number, it is expected that $m^{(\text{orb})}$ and $m^{(\text{spin})}$ can be approximately treated separately. This applies not only to systems with negligible spin-orbit coupling (SOC), but also to cases where SOC preserves the spin direction either locally or globally, such as in $\hat{H}_{\text{SOI}} = \alpha_{\text{SO}} \mathbf{k} \cdot \boldsymbol{\sigma}$ [5–8].

It is important to note that the electron PAM is fundamentally different from the orbital angular momenta. The latter refers to the characteristics of atomic orbitals or the rotational motion of electrons, which are largely independent of the global crystal symmetry. Meanwhile, the former is a quantum number determined solely by the screw symmetry of the crystal. Hence, it is the PAM rather than the angular momenta that plays a significant role in phenomena involving the screw symmetry, e.g., selection rules in chiral crystals with helical structures. However, it is expected that the features of atomic orbitals underlie those of PAM because each atomic orbital constitutes the PAM in a way that the symmetry of the crystal adopts.

In the same manner, the phonon PAM is defined at crystal momentum $\mathbf{q} = (0, 0, q)$ by the eigenvalue of \hat{S}_n [9–12]:

$$\hat{S}_n \mathbf{u}_{\mathbf{q}}(\mathbf{r}) = \lambda_{S_n}^{(\text{ph})} \mathbf{u}_{\mathbf{q}}(\mathbf{r}).$$

As long as considering the phonon propagation along the z -axis, the explicit expression becomes

$$\begin{aligned} \hat{S}_n \mathbf{u}_{\mathbf{q}}(\mathbf{r}) &= [\hat{C}_n \boldsymbol{\epsilon}_{\mathbf{q}}] \zeta_{\mathbf{q}} \exp\left(i\mathbf{q} \cdot [\hat{C}_n |\mathbf{c}/n]^{-1} \mathbf{r}\right) \\ &= [\hat{C}_n \boldsymbol{\epsilon}_{\mathbf{q}}] \zeta_{\mathbf{q}} \exp\left(i(\hat{C}_n \mathbf{q}) \cdot \mathbf{r} - i(\hat{C}_n \mathbf{q}) \cdot \frac{\mathbf{c}}{n}\right) \\ &= [\hat{C}_n \boldsymbol{\epsilon}_{\mathbf{q}}] \zeta_{\mathbf{q}} \exp\left(iqz - i\frac{qc}{n}\right), \end{aligned}$$

where we used

$$[\hat{C}_n |\mathbf{c}/n]^{-1} = [\hat{C}_n^{-1} | -\hat{C}_n^{-1} \mathbf{c}/n].$$

The eigenvalue of $[\hat{C}_n \boldsymbol{\epsilon}_{\mathbf{q}}]$ corresponding to the discrete rotation is related to $\exp\left(-i\frac{2\pi}{n} l_{\text{PAM,ph}}^s\right) \boldsymbol{\epsilon}_{\mathbf{q}}$ with the discrete integer $l_{\text{PAM,ph}}^s$. Therefore,

$$\hat{S}_n \mathbf{u}_{\mathbf{q}}(\mathbf{r}) = \exp\left(-i\frac{qc}{n} - i\frac{2\pi}{n} l_{\text{PAM,ph}}^s\right) \mathbf{u}_{\mathbf{q}}(\mathbf{r}), \quad (\text{S.4})$$

holds, where the spin part $l_{\text{PAM,ph}}^s \in \mathbb{Z}_n$ originates from the local atomic rotation. Note that, in the context of phonon PAM, the phase factor $\exp(-iqc/n)$ is usually written as $\exp(-i\frac{2\pi}{n} l_{\text{PAM,ph}}^o)$, where $l_{\text{PAM,ph}}^o$ is interpreted as the orbital component of phonon PAM. The total phonon PAM is then written as the sum $l_{\text{PAM,ph}}^s + l_{\text{PAM,ph}}^o$. In contrast, in this article, we refer to the spin part merely as phonon PAM in order to avoid confusion with the designation in electronic systems.

2. Selection rule of pseudo-angular momentum.

In the previous section, we introduced the PAM defined by screw symmetry. Here, we provide an overview of the conservation laws of the PAM between the initial and final states through the interaction process. Hereafter, as in the main text, we consider wave vectors such as $\mathbf{k} = (0, 0, k)$, and the index z is omitted for simplicity.

The screw symmetry of the crystal conserves the total PAM, just as the lattice periodicity conserves the total crystal momentum. It is not the angular momentum but the PAM that is strictly conserved. This is similar to the situation where the discrete angular momentum, rather than the angular momentum, is conserved under rotation symmetry. Expressed in a more detailed form, when the interaction Hamiltonian \hat{H}_{int} is invariant with respect to screw symmetry \hat{S}_n ;

$$\hat{S}_n^{-1} \hat{H}_{\text{int}} \hat{S}_n = \hat{H}_{\text{int}},$$

the total PAM of all elementary excitations involved is conserved modulo n . One of the well-known examples is the selection rule for the optical transition process [9, 10, 13, 14], where the total PAM of the phonon and the circularly polarized light is conserved. Moreover, the crystal momentum is conserved between the initial and final states;

$$\mathbf{k}_{i,1} + \mathbf{k}_{i,2} + \cdots = \mathbf{k}_{f,1} + \mathbf{k}_{f,2} + \cdots,$$

where $i(f)$ means the initial (final) state. This relation makes factors such as $\exp(-ikc/n)$ included in the PAM ignorable because they are always cancelled out:

$$\exp(-i\frac{k_{i,1}c}{n})\exp(-i\frac{k_{i,2}c}{n})\cdots = \exp(-i\frac{k_{f,1}c}{n})\exp(-i\frac{k_{f,2}c}{n})\cdots$$

Therefore, the selection rule is usually written by the discrete part of PAM, e.g., $l_{\text{PAM,el}}$ or $l_{\text{PAM,ph}}^s$ that we defined above.

As another example, the same argument can be applied to the EPC. In this case, the phonon PAM and the electron PAM are involved in the selection rule [2]. Thus, the following constraints are imposed on the interaction Hamiltonian by the screw symmetry alone, in the process of phonon creation or annihilation:

$$l_{\text{PAM,el}} + l_{\text{PAM,ph}}^s = l'_{\text{PAM,el}} \pmod n,$$

or equivalently

$$m_{\mathbf{k}}^{(\text{orb})} + m_{\mathbf{k}}^{(\text{spin})} + l_{\text{PAM,ph}}^s = m'_{\mathbf{k}+\mathbf{q}}^{(\text{orb})} + m'_{\mathbf{k}+\mathbf{q}}^{(\text{spin})} \pmod n.$$

However, it is not clear whether the EPC induces spin flips in electrons. In other words, the spin PAM $m_{\mathbf{k}}^{(\text{spin})}$ could be independently preserved and the selection rule does not necessarily involve both orbital and spin components $m_{\mathbf{k}}^{(\text{orb})}$ and $m_{\mathbf{k}}^{(\text{spin})}$. This is because, when the electron PAM is well separated into these components and the EPC only includes contributions from the lattice displacement, exchange between the phonon and electron PAM occurs solely in the orbital components.

In the following sections, we consider a more general form of the EPC Hamiltonian based on previous research [15, 16]. Starting from the Hamiltonian that explicitly includes the spin-orbit coupling, we will derive the effective EPC, of which the selection rule includes both $m_{\mathbf{k}}^{(\text{spin})}$ and $m_{\mathbf{k}}^{(\text{orb})}$.

3. Bir-Pikus formalism.

In the elementary formulation, the Fröhlich Hamiltonian is commonly used to describe the EPC, incorporating only the effect of the periodic potential modulated by lattice displacements. However, the modified lattice potential can exert a crucial influence on electrons via the SOC. Several previous studies derived the EPC that takes into account both the modification of the periodic potential and the variation in the SOC strength induced by phonons [15, 17–21]. In particular, Luo and Dai qualitatively discussed the EPC under rotational symmetry [15], where the effects of phonon-induced lattice displacements on electrons are fully considered. We therefore extend this theory to systems under screw symmetry and qualitatively derive the EPC between chiral phonons and electrons.

The essence of Ref. [15] is that the deformation of the lattice potential due to phonons is treated beyond the regular perturbation theory because a generic deformed lattice potential no longer has the same periodicity as the original one in general. Hence, the coordinates are transformed so that the periodicity in the new coordinate system, which incorporates phonon displacements, coincides with the unstrained system in the original one. Subsequently, derivation of the effective EPC is achieved by performing the usual perturbation theory. We here briefly follow the same approach while replacing the features associated with rotational symmetry with those with screw symmetry.

We also start from the single-electron Hamiltonian, which respects the lattice symmetry:

$$\hat{H}_0 = \frac{\hat{\mathbf{p}}^2}{2m_e} + V_0(\hat{\mathbf{r}}) + \xi_{\text{SO}}\hat{\mathbf{p}} \cdot (\hat{\boldsymbol{\sigma}} \times \nabla V_0(\hat{\mathbf{r}})), \quad (\text{S.5})$$

where we assume the periodic potential is screw symmetric satisfying $\hat{S}_n^{-1}V_0(\hat{\mathbf{r}})\hat{S}_n = V_0(\hat{\mathbf{r}})$. The total Hamiltonian, therefore, also satisfies $\hat{S}_n^{-1}\hat{H}_0\hat{S}_n = \hat{H}_0$. The local strain operator $\hat{\boldsymbol{\varepsilon}}$ in terms of the phonon displacement is calculated by $\hat{\varepsilon}_{lm} = \partial_m \hat{u}_l$. This strain transforms the electron's operators and wave numbers up to the linear order as follows.

$$\begin{aligned} \hat{\mathbf{r}} &\rightarrow \hat{\mathbf{r}} + \hat{\boldsymbol{\varepsilon}}\hat{\mathbf{r}}, \\ \hat{\mathbf{p}} &\rightarrow \hat{\mathbf{p}} - \hat{\boldsymbol{\varepsilon}}\hat{\mathbf{p}}, \\ \mathbf{k} &\rightarrow \mathbf{k} - \boldsymbol{\varepsilon}\mathbf{k}. \end{aligned}$$

Accordingly, the Hamiltonian is transformed in the deformed coordinate, and the margin corresponds to the part of EPC:

$$\hat{H}_0 \rightarrow \hat{H}_0 + \hat{H}_{\text{int}}.$$

According to the detailed calculations in Ref. [15], the EPC Hamiltonian \hat{H}_{int} can be expressed using a certain rank-2 tensor operator and the strain operator as follows.

$$\begin{aligned} \hat{H}_{\text{int}} &= -\frac{1}{m_e} (\hat{\mathbf{p}} + \xi_{\text{SO}}(\hat{\boldsymbol{\sigma}} \times \nabla V_0))_i \hat{\varepsilon}_{ij} \hat{\mathbf{p}}_j - \xi_{\text{SO}} (\hat{\mathbf{p}} \times \hat{\boldsymbol{\sigma}})_i \hat{\varepsilon}_{ij} \partial_j V_0 + V_{ij} \hat{\varepsilon}_{ij} + \xi_{\text{SO}} [\hat{\boldsymbol{\sigma}} \times (\hat{\varepsilon}_{ij} \nabla V_{ij})] \cdot \hat{\mathbf{p}} \\ &\equiv \hat{\varepsilon}_{ij} \hat{\mathcal{V}}_{ij} + \mathcal{O}(q^2), \end{aligned} \quad (\text{S.6})$$

where

$$V_{ij} = \lim_{\varepsilon \rightarrow 0} \frac{V_\varepsilon((1 + \hat{\varepsilon})\mathbf{r}) - V_0(\mathbf{r})}{\hat{\varepsilon}_{ij}}. \quad (\text{S.7})$$

We are now able to use safely the conventional perturbation theory and obtain the total effective Hamiltonian and the corresponding Bloch function, which satisfy

$$\begin{aligned} \hat{H}_{\mathbf{k}}^{(\text{eff})} \tilde{u}_{\mathbf{k}}(\mathbf{r}) &= E_{\mathbf{k}} \tilde{u}_{\mathbf{k}}(\mathbf{r}), \\ \tilde{\psi}_{\mathbf{k}}(\mathbf{r}) &= e^{i\mathbf{k} \cdot \mathbf{r}} u_{\mathbf{k}}((1 + \varepsilon)\mathbf{r}) \equiv e^{i\mathbf{k} \cdot \mathbf{r}} \tilde{u}_{\mathbf{k}}(\mathbf{r}). \end{aligned}$$

Through further calculations with $\mathbf{k} \cdot \mathbf{p}$ perturbation, we obtain the following expression, where we focused on the dominant contribution of the EPC term \hat{H}_{ep} up to the zeroth order of \mathbf{k} and the first order of \mathbf{q} .

$$\begin{aligned} \hat{H}_{\mathbf{k}}^{(\text{eff})} &= \hat{H}_{0, \mathbf{k}} + \hat{H}_{\text{ep}}, \\ \hat{H}_{0, \mathbf{k}} &\equiv e^{-i\mathbf{k} \cdot \mathbf{r}} \hat{H}_0 e^{i\mathbf{k} \cdot \mathbf{r}} \\ &= \frac{\hbar^2 k^2}{2m_e} + \frac{\hbar}{m_e} \mathbf{k} \cdot [\hat{\mathbf{p}} + \xi_{\text{SO}} (\hat{\boldsymbol{\sigma}} \times \nabla V_0(\mathbf{r}))] + \hat{H}_0, \\ \hat{H}_{\text{ep}} &= \hat{\varepsilon}_{ij} \hat{\mathcal{V}}_{ij}. \end{aligned}$$

So far, we have not specified the coordinate system strictly. Here, since we are interested in chiral phonons, we introduce the chiral basis and rewrite all vector components accordingly. Moreover, when we focus on the phonon propagation along the chiral axis, the strain tensor components $\hat{\varepsilon}_{iz}$ ($i = x, y$) are significant. Then we rewrite the local strain in the chiral basis as follows,

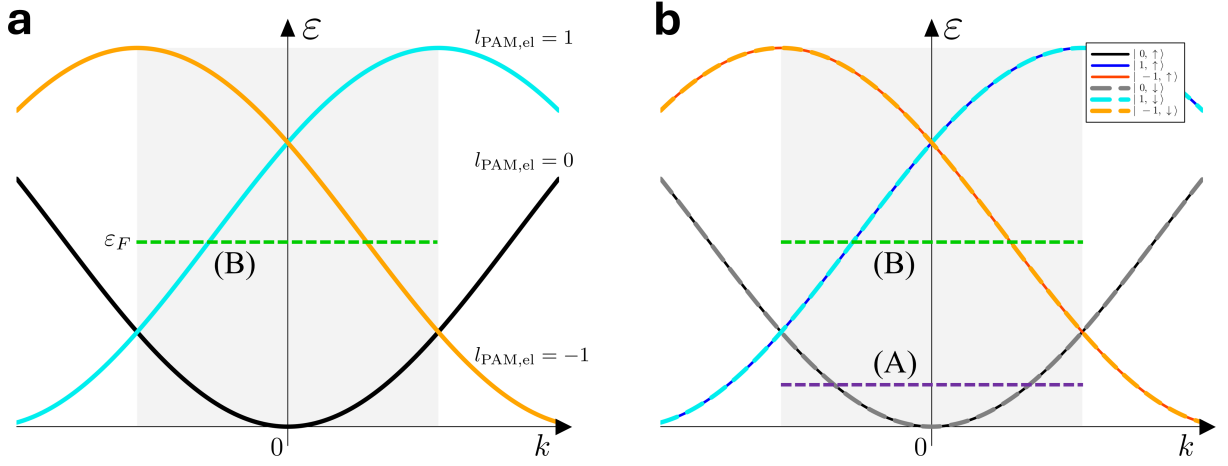
$$\begin{aligned} \hat{\varepsilon}_{\pm} &\equiv \frac{1}{\sqrt{N_i}} \sum_q i q \sqrt{\frac{\hbar}{2M_i \omega_{q, \pm}}} (\hat{b}_{q, \pm} + \hat{b}_{-q, \mp}^\dagger) e^{iqz}, \\ \hat{\varepsilon}_0 &\equiv \frac{1}{\sqrt{N_i}} \sum_q i q \sqrt{\frac{\hbar}{2M_i \omega_{q, 0}}} (\hat{b}_{q, 0} + \hat{b}_{-q, 0}^\dagger) e^{iqz}, \end{aligned}$$

and accordingly, we also redefine the spherical components $\hat{\mathcal{V}}_0, \hat{\mathcal{V}}_{\pm}$ so that the EPC Hamiltonian becomes $\hat{H}_{\text{ep}} = \hat{\varepsilon}_0 \hat{\mathcal{V}}_0 + \hat{\varepsilon}_{\pm} \hat{\mathcal{V}}_{\pm} + \hat{\varepsilon}_{\mp} \hat{\mathcal{V}}_{\mp}$. Therefore, we finally reach the matrix elements of the EPC Hamiltonian:

$$\begin{aligned} \langle \psi_{k, l_{\text{PAM}, \text{el}}} | \hat{\varepsilon}_0 \hat{\mathcal{V}}_0 | \psi_{k', l'_{\text{PAM}, \text{el}}} \rangle &= i q \sqrt{\frac{\hbar}{2N_i M_i \omega_{q, 0}}} (\hat{b}_{q, 0} + \hat{b}_{-q, 0}^\dagger) \langle u_{k, l_{\text{PAM}, \text{el}}} | \hat{\mathcal{V}}_0 | u_{k', l'_{\text{PAM}, \text{el}}} \rangle \delta(k' + q, k) \delta(l'_{\text{PAM}, \text{el}}, l_{\text{PAM}, \text{el}}) \\ &\equiv \frac{g^{(0)}(k, q, l_{\text{PAM}, \text{el}}, l'_{\text{PAM}, \text{el}})}{\sqrt{N_i}} i q \hat{\zeta}_{q, 0} \delta(k' + q, k) \delta(l'_{\text{PAM}, \text{el}}, l_{\text{PAM}, \text{el}}), \\ \langle \psi_{k, l_{\text{PAM}, \text{el}}} | \hat{\varepsilon}_{\pm} \hat{\mathcal{V}}_{\mp} | \psi_{k', l'_{\text{PAM}, \text{el}}} \rangle &= i q \sqrt{\frac{\hbar}{2N_i M_i \omega_{q, \pm}}} (\hat{b}_{q, \pm} + \hat{b}_{-q, \mp}^\dagger) \langle u_{k, l_{\text{PAM}, \text{el}}} | \hat{\mathcal{V}}_{\mp} | u_{k', l'_{\text{PAM}, \text{el}}} \rangle \\ &\quad \times \delta(k' + q, k) \delta(l'_{\text{PAM}, \text{el}} \pm 1, l_{\text{PAM}, \text{el}}) \\ &\equiv \frac{g^{(\pm)}(k, q, l_{\text{PAM}, \text{el}}, l'_{\text{PAM}, \text{el}})}{\sqrt{N_i}} i q \hat{\zeta}_{q, \pm} \delta(k' + q, k) \delta(l'_{\text{PAM}, \text{el}} \pm 1, l_{\text{PAM}, \text{el}}). \end{aligned}$$

Note that our notation slightly differs from that of Ref. [15] because we have defined the components of the phonon displacement in chiral coordinates.

In the above derivation, there are three points worth mentioning. To begin with, as previously mentioned, the total PAM as well as the crystal momentum are conserved as a consequence of screw symmetry alone. This was mentioned in the previous study [2], where the total PAM excluding the electron spin contribution is conserved because the EPC arising from the modified hopping strength was considered. It is also pointed out that, in each phonon mode with a specific PAM, the longitudinal and transverse components are mixed [2, 9, 22–27]. However, the phonon PAM approximately coincides with the phonon angular momentum in the long-wavelength regime. In some models [22, 23], this correspondence remains accurate even up to half of the Brillouin zone (BZ). Therefore, for brevity, in the main text, we do not explicitly distinguish between the angular momentum and



Supplementary Figure S1. **Electronic band structures classified by pseudo-angular momentum with \hat{S}_3 symmetry [1].** **a**, The electronic bands for spinless case, where the bands are labelled by integer PAM. **b**, The electronic bands for spinful case with negligible spin-orbit coupling, where PAM is a half-integer. Two representative Fermi levels are indicated by the purple dashed line (A) and green dashed line (B). The electronic bands are shown in the extended zone scheme and the gray rectangle represents the reduced BZ folded by the \hat{S}_3 symmetry.

PAM unless necessary, and rewrite $l_{\text{PAM,ph}} = 0, \pm 1 \rightarrow l_{z,L}^{(\text{ph})} = 0, l_{z,\lambda}^{(\text{ph})} = \lambda$ ($\lambda = \pm 1$). Accordingly, the phonon Hamiltonian is written as the sum of all branches:

$$\hat{H}_{\text{ph}} = \sum_q \hbar\omega_{q,L} \hat{b}_{q,L}^\dagger \hat{b}_{q,L} + \sum_{q,\lambda} \hbar\omega_{q,\lambda} \hat{b}_{q,\lambda}^\dagger \hat{b}_{q,\lambda}.$$

Next, it is impractical to determine the coupling coefficients $g^{(0)}(k, q, l_{\text{PAM,el}}, l'_{\text{PAM,el}})$ in realistic materials. In this study, we assume

$$\begin{aligned} g^{(0)}(k, q, l_{\text{PAM,el}}, l'_{\text{PAM,el}}) &= g_L, \\ g^{(\pm)}(k, q, l_{\text{PAM,el}}, l'_{\text{PAM,el}}) &= g_T, \end{aligned}$$

with the constants g_L and g_T . This simplification is justified by the fact that our analysis focuses on qualitative features, and the difference in magnitude between $g^{(+)}(k, q, l_{\text{PAM,el}}, l'_{\text{PAM,el}})$ and $g^{(-)}(k, q, l_{\text{PAM,el}}, l'_{\text{PAM,el}})$ has only a minor effect due to the intrinsic splitting of the phonon branches $\omega_{q,\pm}$.

The last point is that we assumed a Hamiltonian with SOC as the starting point for the derivation. This allows us to safely conclude that total PAM conservation includes the electron spin component; namely, $l_{\text{PAM,ph}}^s$, $m^{(\text{orb})}$, and $m^{(\text{spin})}$ are all intertwined. This type of EPC is called spin-orbit assisted electron-phonon coupling in some studies [20, 21]. Its physical interpretation is given as follows [18]. The change in the periodic potential associated with the lattice displacements, i.e., the modulation of $\nabla V_0(\hat{r})$, induces an additional local electric field. This field has the SOC-like effect, causing $l_{\text{PAM,ph}}$, $m_{\mathbf{k},\sigma}^{(\text{orb})}$, and $m_{\mathbf{k},\sigma}^{(\text{spin})}$ to all hybridize. Therefore, it is expected that the strong SOC in an electronic system favors CISSPT. However, it is not certain whether this type of EPC is weak in a system with a weak electronic SOC. This is because even if the intrinsic field $\nabla V_0(\hat{r})$ is sufficiently small, such terms as V_{ij} in Eq. (S.6) could become large enough. A more quantitative evaluation of their details is expected in future studies.

With keeping the above points in mind, in the main text, we assume a simple SOC Hamiltonian for the electronic system, since our main interest is the role of chiral phonons. Specifically, we consider a parabolic approximation or a spin-diagonal Hamiltonian $\hat{H}_{\text{SO}} = \alpha_{\text{SO}} \mathbf{k} \cdot \boldsymbol{\sigma}$ as simple models. In these cases, the electronic PAM is simplified as $l_{\text{PAM,el}} = m_{\text{orb}} + \sigma$. Therefore, we eventually obtain the EPC for each branch.

$$\hat{H}_{\text{ep}}^{(\text{L})} = \frac{1}{\sqrt{N_i}} \sum_{\mathbf{k},q} \sum_{s,s',m_{\text{orb}},m'_{\text{orb}}} i q g_L \hat{c}_{\mathbf{k}+q,s,m_{\text{orb}}}^\dagger \hat{c}_{\mathbf{k},s',m'_{\text{orb}}} \hat{\zeta}_{q,L} \delta_{m_{\text{orb}}+s, m'_{\text{orb}}+s'}, \quad (\text{S.8})$$

$$\hat{H}_{\text{ep}}^{(\text{T})} = \frac{1}{\sqrt{N_i}} \sum_{\mathbf{k},q} \sum_{s,s',m_{\text{orb}},m'_{\text{orb}}} \sum_{\lambda=\pm} i q g_T \hat{c}_{\mathbf{k}+q,s,m_{\text{orb}}}^\dagger \hat{c}_{\mathbf{k},s',m'_{\text{orb}}} \hat{\zeta}_{q,\lambda} \delta_{m_{\text{orb}}+s, m'_{\text{orb}}+s'+l_{z,\lambda}^{\text{ph}}}. \quad (\text{S.9})$$

4. Pseudo-angular momenta in the electronic bands.

Figure S1 illustrates how the PAM classifies electronic bands with the three-fold screw symmetry and the possible Peierls instabilities. Figure S1a shows the spinless case, where the PAM takes integer values. On the other hand, Figure S1b shows the spinful case with negligible SOC, in which the PAM is a half-integer and the spin remains a good quantum number. In this situation, the electronic bands are labelled by $l_{\text{PAM,el}} = m_{\mathbf{k}}^{(\text{orb})} + s$.

When the Fermi level intersects the band with $m_{\text{orb}} = 0$ corresponding to (A), i.e., the orbital contributions are not involved, the conservation law of PAM in the EPC reduces to the relation $s + l_{\text{PAM,ph}} = s'$. Only the electron spin and the phonon PAM participate in this process, and the resulting instability corresponds to the CISSPT discussed in the main text and Supplementary Notes 2-3. By contrast, when the Fermi level lies in the bands with non-zero m_{orb} as shown by (B), such that electron spin is not changed, the Peierls instability couples the states with $m_{\text{orb}} = \pm 1$. In this case, PAM conservation is fulfilled through the orbital component of the electron and the phonon PAM, leading to a transverse Peierls transition and a winding charge density wave as described in Supplementary Note 4.

In essence, Fig. S1 highlights that the nature of the Peierls instability, whether spin-selective Peierls states or winding CDW states are realized, is determined by whether the spin or the orbital component of the electronic PAM, or both of them participate in the conservation law at the Fermi level.

Supplementary Note 2. Detailed calculations for CISSPT.

In this Supplementary note, we show the details of calculations and add information for the basic properties of chirality-induced spin-selective Peierls transitions.

1. Notations for Green functions.

In this section, we briefly describe the basic notation for later calculations using the Green function [28]. Regarding the phonon Green function, the expectation value $\langle \hat{\zeta}_{q,\eta} \hat{\zeta}_{q',\eta'} \rangle$ is finite only for time-reversal paired indices, that is, when $q' = -q$ and $\eta' = -\eta$; otherwise, it vanishes. Therefore, the phonon Green function is defined as

$$\mathcal{D}(q, \eta, \tau - \tau') = -\langle T(\hat{b}_{q,\eta}(\tau) + \hat{b}_{-q,-\eta}^\dagger(\tau))(\hat{b}_{-q,-\eta}(\tau') + \hat{b}_{q,\eta}^\dagger(\tau')) \rangle,$$

where τ is the imaginary time. We omit the interaction and Heisenberg representation indicators for brevity. Each mode can be written down in detail as

$$\begin{aligned} \mathcal{D}_L^{(0)}(q, \tau - \tau') &\equiv \mathcal{D}^{(0)}(q, L, \tau - \tau') \\ &= -e^{-\hbar\omega_{q,L}(\tau-\tau')} [\Theta(\tau - \tau')(1 + n(\hbar\omega_{q,L})) + \Theta(\tau' - \tau)n(\hbar\omega_{q,L})] \\ &\quad - e^{\hbar\omega_{-q,L}(\tau-\tau')} [\Theta(\tau - \tau')n(\hbar\omega_{-q,L}) + \Theta(\tau' - \tau)(1 + n(\hbar\omega_{-q,L}))], \\ \mathcal{D}_T^{(0)}(q, \lambda, \tau - \tau') &\equiv \mathcal{D}^{(0)}(q, \lambda, \tau - \tau') \\ &= -e^{-\hbar\omega_{q,\lambda}(\tau-\tau')} [\Theta(\tau - \tau')(1 + n(\hbar\omega_{q,\lambda})) + \Theta(\tau' - \tau)n(\hbar\omega_{q,\lambda})] \\ &\quad - e^{\hbar\omega_{-q,-\lambda}(\tau-\tau')} [\Theta(\tau - \tau')n(\hbar\omega_{-q,-\lambda}) + \Theta(\tau' - \tau)(1 + n(\hbar\omega_{-q,-\lambda}))]. \end{aligned}$$

We then perform a Fourier transformation on the phonon Green function with respect to the Matsubara frequency:

$$\begin{aligned} \mathcal{D}_L^{(0)}(q, i\omega_m) &\equiv \int_0^\beta d\tau \mathcal{D}_L^{(0)}(q, \tau) e^{i\omega_m \tau} \\ &= \frac{2\hbar\omega_{q,L}}{(i\omega_m)^2 - (\hbar\omega_{q,L})^2}, \\ \mathcal{D}_T^{(0)}(q, \lambda, i\omega_m) &\equiv \int_0^\beta d\tau \mathcal{D}_T^{(0)}(q, \lambda, \tau) e^{i\omega_m \tau} \\ &= \frac{2\hbar\omega_{q,\lambda}}{(i\omega_m)^2 - (\hbar\omega_{q,\lambda})^2}, \end{aligned}$$

where we used $\omega_{-q,L} = \omega_{q,L}$ and $\omega_{-q,-\lambda} = \omega_{q,\lambda}$, and $\omega_m = 2\pi m/\beta$ denote the bosonic Matsubara frequencies.

On the other hand, the electron Green function is defined as

$$\mathcal{G}_{ss'}(k, \tau - \tau') = -\langle T \hat{c}_{k,s}(\tau) \hat{c}_{k,s'}^\dagger(\tau') \rangle.$$

When the electron Hamiltonian is spin-diagonal, it becomes

$$\mathcal{G}_{ss'}^{(0)}(k, i\epsilon_n) = \frac{1}{i\epsilon_n - \xi_{k,s}} \delta_{s,s'},$$

where $\epsilon_n = (2n + 1)\pi/\beta$ are the fermionic Matsubara frequencies.

Accordingly, the electron-phonon coupling for CISSPT (see the main text) is given by the following expression in the interaction representation.

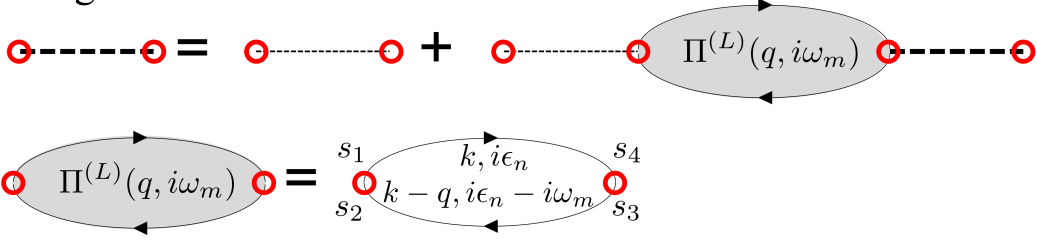
$$\begin{aligned} \hat{H}_{\text{ep}}^{(L)}(\tau) &= \frac{1}{\sqrt{N_i}} \sum_{\mathbf{k}, q, s, s'} g_{s,s'}^{(L)}(q) \hat{c}_{\mathbf{k}+q,s}^\dagger(\tau) \hat{c}_{\mathbf{k},s'}(\tau) (\hat{b}_{q,L}(\tau) + \hat{b}_{-q,L}^\dagger(\tau)), \\ \hat{H}_{\text{ep}}^{(T)}(\tau) &= \frac{1}{\sqrt{N_i}} \sum_{\mathbf{k}, q, \lambda, s, s'} g_{s,s'}^{(T)}(q, \lambda) \hat{c}_{\mathbf{k}+q,s}^\dagger(\tau) \hat{c}_{\mathbf{k},s'}(\tau) (\hat{b}_{q,\lambda}(\tau) + \hat{b}_{-q,-\lambda}^\dagger(\tau)), \end{aligned}$$

and we define the vertex coefficient for the following calculation as follows.

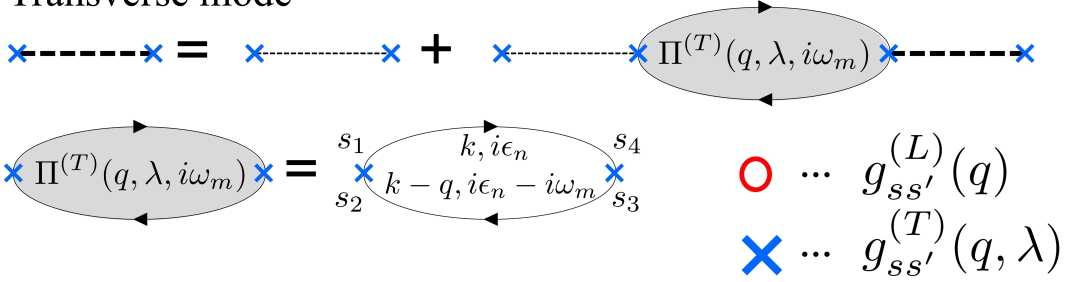
$$g_{s,s'}^{(L)}(q) = i q g_L \sqrt{\frac{\hbar}{2M_i \omega_{q,L}}} (\hat{\sigma}_0)_{ss'}, \quad (\text{S.10})$$

$$g_{s,s'}^{(T)}(q, \lambda) = i q g_T \sqrt{\frac{\hbar}{2M_i \omega_{q,\lambda}}} (\hat{\sigma}_\lambda)_{ss'}. \quad (\text{S.11})$$

Longitudinal mode



Transverse mode



Supplementary Figure S2. **Feynman diagram for the calculation of the renormalized phonon frequency.** The red circles represent the vertex part for $\hat{H}_{\text{ep}}^{(L)}$ while the blue crosses for $\hat{H}_{\text{ep}}^{(T)}$.

2. Calculations for the renormalized phonon frequency.

We describe in detail the method for calculating the renormalized phonon frequencies. We begin by deriving the general form of the phonon self-energy [29]. The renormalized phonon frequency under the random phase approximation (RPA) can be evaluated from the Feynman diagrams shown in Fig. S2. The Green functions for the dressed phonons, which incorporate electronic screening, satisfy the following Dyson equations:

$$\begin{aligned}\mathcal{D}_L(q, i\omega_m) &= \mathcal{D}_L^{(0)}(q, i\omega_m) + \mathcal{D}_L^{(0)}(q, i\omega_m)\Pi^{(L)}(q, i\omega_m)\mathcal{D}_L(q, i\omega_m), \\ \mathcal{D}_T(q, \lambda, i\omega_m) &= \mathcal{D}_T^{(0)}(q, \lambda, i\omega_m) + \mathcal{D}_T^{(0)}(q, \lambda, i\omega_m)\Pi^{(T)}(q, \lambda, i\omega_m)\mathcal{D}_T(q, \lambda, i\omega_m).\end{aligned}$$

Therefore,

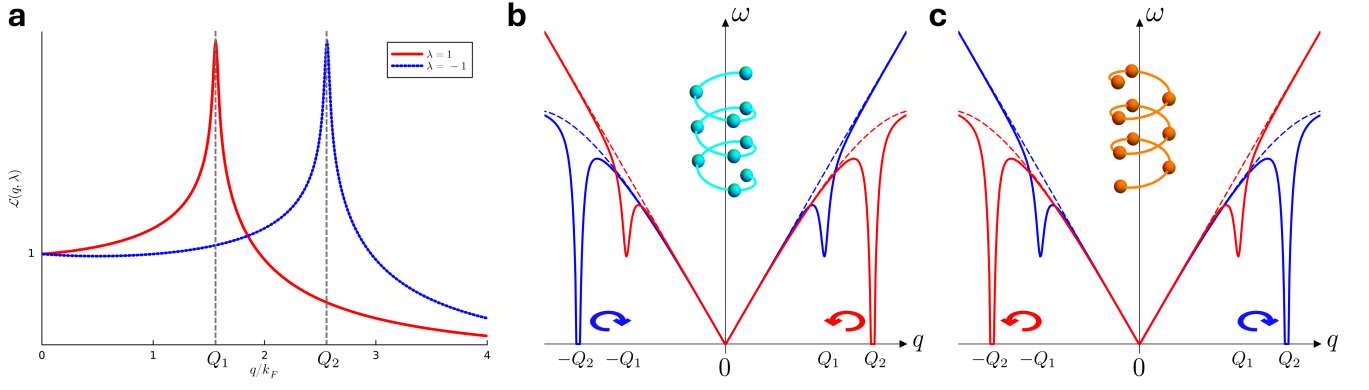
$$\begin{aligned}\mathcal{D}_L^{-1}(q, i\omega_m) &= \mathcal{D}_L^{(0)}(q, i\omega_m)^{-1} - \Pi^{(L)}(q, i\omega_m), \\ \mathcal{D}_T^{-1}(q, \lambda, i\omega_m) &= \mathcal{D}_T^{(0)}(q, \lambda, i\omega_m)^{-1} - \Pi^{(T)}(q, \lambda, i\omega_m).\end{aligned}$$

Under the RPA and the Migdal approximation, the phonon self-energy is

$$\begin{aligned}\Pi^{(L)}(q, i\omega_m) &= \frac{k_B T}{N_i} \sum_{k, i\epsilon_n} \sum_{s_1 s_2 s_3 s_4} g_{s_1 s_2}^{(L)}(q) g_{s_3 s_4}^{(L)}(-q) \mathcal{G}_{s_4 s_1}^{(0)}(k, i\epsilon_n) \mathcal{G}_{s_2 s_3}^{(0)}(k - q, i\epsilon_n - i\omega_m), \\ \Pi^{(T)}(q, \lambda, i\omega_m) &= \frac{k_B T}{N_i} \sum_{k, i\epsilon_n} \sum_{s_1 s_2 s_3 s_4} g_{s_1 s_2}^{(T)}(q, \lambda) g_{s_3 s_4}^{(T)}(-q, -\lambda) \mathcal{G}_{s_4 s_1}^{(0)}(k, i\epsilon_n) \mathcal{G}_{s_2 s_3}^{(0)}(k - q, i\epsilon_n - i\omega_m).\end{aligned}$$

Substituting Eqs. (S.10) and (S.11) yields

$$\begin{aligned}\Pi^{(L)}(q, i\omega_m) &= \frac{k_B T}{N_i} \sum_{k, i\epsilon_n} \sum_s \frac{\hbar q^2 g_L^2}{2M_i \omega_{q,L}} \mathcal{G}_{ss}^{(0)}(k, i\epsilon_n) \mathcal{G}_{ss}^{(0)}(k - q, i\epsilon_n - i\omega_m) \equiv \frac{\hbar q^2 g_L^2}{2M_i \omega_{q,L}} \chi_{zz}(q, i\omega_m), \\ \Pi^{(T)}(q, +, i\omega_m) &= \frac{k_B T}{N_i} \sum_{k, i\epsilon_n} \frac{2\hbar q^2 g_T^2}{M_i \omega_{q,+}} \mathcal{G}_{\uparrow\uparrow}^{(0)}(k, i\epsilon_n) \mathcal{G}_{\downarrow\downarrow}^{(0)}(k - q, i\epsilon_n - i\omega_m) \equiv \frac{2\hbar q^2 g_T^2}{M_i \omega_{q,+}} \chi_{+-}(q, i\omega_m), \\ \Pi^{(T)}(q, -, i\omega_m) &= \frac{k_B T}{N_i} \sum_{k, i\epsilon_n} \frac{2\hbar q^2 g_T^2}{M_i \omega_{q,-}} \mathcal{G}_{\downarrow\downarrow}^{(0)}(k, i\epsilon_n) \mathcal{G}_{\uparrow\uparrow}^{(0)}(k - q, i\epsilon_n - i\omega_m) \equiv \frac{2\hbar q^2 g_T^2}{M_i \omega_{q,-}} \chi_{-+}(q, i\omega_m).\end{aligned}$$



Supplementary Figure S3. **Softening of chiral phonons with explicit spin-orbit coupling.** **a**, Dimensionless Lindhard function $\tilde{L}_\lambda(q, \lambda)$ for $\alpha_{\text{SO}}k_F/\varepsilon_F = 1$, showing logarithmic singularities at wave vectors Q_1 and Q_2 . **b**, Schematic illustration of the phonon dispersion for the LH crystal. Chiral phonon branches $\lambda = \pm 1$ exhibit Kohn anomalies at distinct wave vectors Q_1 and Q_2 . **c**, Schematic illustration of the phonon dispersion for the RH crystal. The correspondence between phonon chirality and nesting vectors is reversed relative to the LH crystal.

Here, $\chi_{zz}, \chi_{+-}, \chi_{-+}$ correspond to individual susceptibility functions, and their explicit forms are given by the Lindhard function:

$$\frac{k_B T}{N_i} \sum_{k, i\epsilon_n} \mathcal{G}_{ss}^{(0)}(k, i\epsilon_n) \mathcal{G}_{s's'}^{(0)}(k - q, i\epsilon_n - i\omega_m) = \frac{1}{N_i} \sum_k \frac{f(\varepsilon_{k-q, s'}) - f(\varepsilon_{k, s})}{i\omega_m + \varepsilon_{k-q, s'} - \varepsilon_{k, s}}. \quad (\text{S.12})$$

By performing the analytic continuation $i\omega_m \rightarrow \hbar\omega + i\delta$, the renormalized phonon frequencies correspond to the poles of the renormalized phonon Green functions, and therefore, they are determined by the condition $\mathcal{D}_L^{-1}(q, \hbar\omega + i\delta) = 0$, $\mathcal{D}_T^{-1}(q, \lambda, \hbar\omega + i\delta) = 0$, where

$$\mathcal{D}_L^{-1}(q, \hbar\omega + i\delta) = \frac{1}{2\hbar\omega_{q,L}} \left[(\hbar\omega + i\delta)^2 - (\hbar\omega_{q,L})^2 \left(1 + \frac{2}{\hbar\omega_{q,L}} \Pi^{(L)}(q, \omega) \right) \right], \quad (\text{S.13})$$

$$\mathcal{D}_T^{-1}(q, \lambda, \hbar\omega + i\delta) = \frac{1}{2\hbar\omega_{q,\lambda}} \left[(\hbar\omega + i\delta)^2 - (\hbar\omega_{q,\lambda})^2 \left(1 + \frac{2}{\hbar\omega_{q,\lambda}} \Pi^{(T)}(q, \lambda, \omega) \right) \right]. \quad (\text{S.14})$$

As usual, the phonon energy scale is assumed to be sufficiently small relative to the Fermi energy. Therefore, the frequency dependence of the phonon self-energies is negligible, and the renormalized phonon frequencies are obtained as

$$\begin{aligned} (\hbar\tilde{\omega}_{q,L})^2 &= (\hbar\omega_{q,L})^2 \left(1 + \frac{2}{\hbar\omega_{q,L}} \text{Re} \Pi^{(L)}(q, 0) \right), \\ (\hbar\tilde{\omega}_{q,\lambda})^2 &= (\hbar\omega_{q,\lambda})^2 \left(1 + \frac{2}{\hbar\omega_{q,\lambda}} \text{Re} \Pi^{(T)}(q, \lambda, 0) \right). \end{aligned}$$

3. The case with explicit electronic spin-orbit couplings.

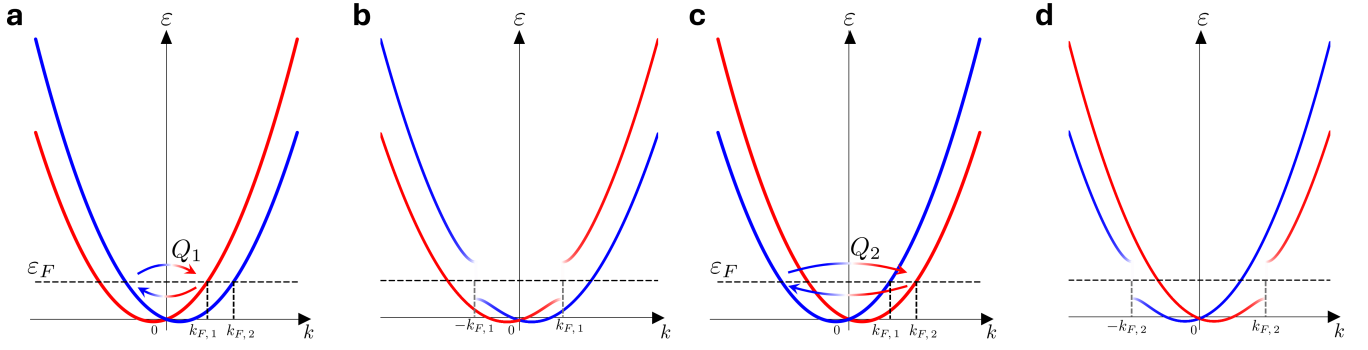
In the main text and Methods, the formulations in the previous section are used to obtain the renormalized phonon frequencies with spin-degenerate electrons. We here show that the same argument can be extended to the case with the electron Hamiltonian including the explicit SOC term. Let us consider the following electron Hamiltonian as the model case.

$$\hat{H}_e = \left(\frac{\hbar^2 k^2}{2m_e} - \varepsilon_F \right) \hat{\sigma}_0 + \alpha_{\text{SO}} \mathbf{k} \cdot \hat{\boldsymbol{\sigma}} = \left(\frac{\hbar^2 k^2}{2m_e} - \varepsilon_F \right) \hat{\sigma}_0 + \alpha_{\text{SO}} k \hat{\sigma}_z,$$

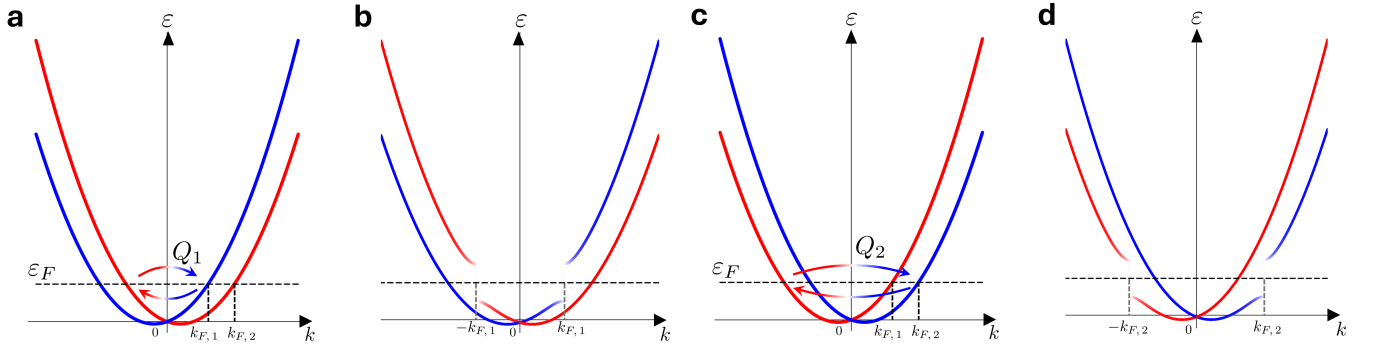
that is, the eigenenergy is

$$\varepsilon_{k,s} = \frac{\hbar^2 k^2}{2m_e} + \alpha_{\text{SO}} k s.$$

Although the sign of the SOC coupling constant α_{SO} depends on the material, it is generally flipped between opposite enantiomorphs [5–8].



Supplementary Figure S4. **Spin-selective Peierls states in the LH crystal with explicit spin-orbit coupling.** **a** and **b**, Case of positive α_{SO} and the soft phonons $(Q_1, +)$ and $(-Q_1, -)$. The nesting vector Q_1 couples the electronic subbands with $(-k_{F,1}, \downarrow)$ and $(k_{F,1}, \uparrow)$, where $k_{F,1} = Q_1/2$. **c** and **d**, Case of negative α_{SO} and the soft phonons $(Q_2, +)$ and $(-Q_2, -)$, corresponding to Fig. S3b. The electronic subbands with $(-k_{F,2}, \downarrow)$ and $(k_{F,2}, \uparrow)$ are coupled, where $k_{F,2} = Q_2/2$.



Supplementary Figure S5. **Spin-selective Peierls states in the RH crystal with explicit spin-orbit coupling.** **a** and **b**, Case of negative α_{SO} and the soft phonons $(Q_1, -)$ and $(-Q_1, +)$. The nesting vector Q_1 couples the electronic subbands with $(-k_{F,1}, \uparrow)$ and $(k_{F,1}, \downarrow)$. **c** and **d**, Case of positive α_{SO} and the soft phonons $(Q_2, -)$ and $(-Q_2, +)$, corresponding to Fig. S3c. The electronic subbands with $(-k_{F,2}, \uparrow)$ and $(k_{F,2}, \downarrow)$ are coupled.

Then, the phonon self-energy with respect to the chiral phonon becomes

$$\begin{aligned}\Pi^{(\text{T})}(q, +, i\omega_m) &= \frac{2\hbar q^2 g_{\text{T}}^2}{M_{\text{i}}\omega_{q,+}} \chi_{+-}(q, i\omega_m) \\ &= \frac{2\hbar q^2 g_{\text{T}}^2}{M_{\text{i}}\omega_{q,+}} \frac{1}{N_{\text{i}}} \sum_{\mathbf{k}} \frac{f(\epsilon_{\mathbf{k}-q,\downarrow}) - f(\epsilon_{\mathbf{k},\uparrow})}{i\omega_m + \epsilon_{\mathbf{k}-q,\downarrow} - \epsilon_{\mathbf{k},\uparrow}}, \\ \Pi^{(\text{T})}(q, -, i\omega_m) &= \frac{2\hbar q^2 g_{\text{T}}^2}{M_{\text{i}}\omega_{q,-}} \chi_{-+}(q, i\omega_m) \\ &= \frac{2\hbar q^2 g_{\text{T}}^2}{M_{\text{i}}\omega_{q,-}} \frac{1}{N_{\text{i}}} \sum_{\mathbf{k}} \frac{f(\epsilon_{\mathbf{k}-q,\uparrow}) - f(\epsilon_{\mathbf{k},\downarrow})}{i\omega_m + \epsilon_{\mathbf{k}-q,\uparrow} - \epsilon_{\mathbf{k},\downarrow}}.\end{aligned}$$

Therefore, the renormalized phonon frequency of each chirality is obtained as

$$(\hbar\tilde{\omega}_{q,\pm})^2 = (\hbar\omega_{q,\pm})^2 \left(1 - \Lambda \tilde{\mathcal{L}}_{\pm}(q, 0)\right),$$

where Λ is a dimensionless electron-phonon coupling constant described in Eq. (S.37) below, and we define the dimensionless Lindhard function:

$$\tilde{\mathcal{L}}_{\lambda}(q, \omega) = -\frac{1}{N_{\text{i}}} \sum_{\mathbf{k}} \sum_{s,s'} \text{Re} \left[\frac{f(\epsilon_{\mathbf{k}-q,s}) - f(\epsilon_{\mathbf{k},s'})}{\hbar\omega + i0 + \epsilon_{\mathbf{k}-q,s} - \epsilon_{\mathbf{k},s'}} \delta(s' - s - \lambda) \right]. \quad (\text{S.15})$$

Figure S3a shows the q dependence of $\tilde{\mathcal{L}}(q, \lambda) \equiv \tilde{\mathcal{L}}_\lambda(q, \omega = 0)$ at low temperatures $k_B T / \epsilon_F \ll 1$. We set $\alpha_{\text{SO}} k_F / \epsilon_F = 1$. The wave vectors at which divergence occurs are given by

$$Q_1/k_F = -\frac{\alpha_{\text{SO}} k_F}{2\epsilon_F} + \sqrt{\left(\frac{\alpha_{\text{SO}} k_F}{2\epsilon_F}\right)^2 + 4}, \quad (\text{S.16})$$

$$Q_2/k_F = \frac{\alpha_{\text{SO}} k_F}{2\epsilon_F} + \sqrt{\left(\frac{\alpha_{\text{SO}} k_F}{2\epsilon_F}\right)^2 + 4}. \quad (\text{S.17})$$

Accordingly, the soft modes are modulated, and as shown in Figs. S3b and S3c, the chiral phonons with each chirality exhibit the Kohn anomaly at different wave vectors Q_1 and Q_2 .

If we alternatively set $\alpha_{\text{SO}} k_F / \epsilon_F = -1$, the wave vectors of anomaly, Q_1 and Q_2 , are switched, and thereby the handedness of frozen phonons is reversed from those shown in Fig. S3. Because the sign of the SOC coupling constant α_{SO} is opposite between different enantiomorphs, the handedness of frozen phonons is closely related to the handedness of crystals. Furthermore, because the sign of α_{SO} can alter depending on the environment even for a fixed enantiomorph, it introduces an additional variety of Kohn anomaly: the SOC parameter determines which of the two nesting vectors, Q_1 or Q_2 , governs the Peierls instability. The combination of crystal handedness and the sign of α_{SO} yields four distinct possibilities for the feasible Peierls states. In the RH crystal corresponding to Fig. S3c, the cases with negative and positive α_{SO} are illustrated in Figs. S5a,b and Figs. S5c,d, respectively. In contrast, for the LH crystal, the same consideration applies with the handedness reversed, as shown in Fig. S4. These four cases exhaust the possible spin-selective Peierls states stabilized in the presence of explicit electronic SOC.

In any case, by treating the spin-split bands as independent subbands, the analysis is a natural extension of the spin-degenerate case, and the same conclusions are obtained. Furthermore, as long as the spin remains a well-defined quantum number at the Fermi level, the argument herein is expected to apply to other types of SOC such as the Rashba SOC [30, 31].

4. Gap equation of spin-selective Peierls states.

In this section, we note the detailed calculations for incommensurate spin-selective Peierls states. We consider spin-degenerate electron bands under the parabolic approximation for simplicity. The energy dispersion in the parent phase is given by

$$\xi_k = \left(\frac{\hbar^2 k^2}{2m_e} - \epsilon_F \right) \delta_{ss'}. \quad (\text{S.18})$$

Under these approximations, the minimal Hamiltonian relevant to the CISSPT is given by

$$\mathcal{H} = \sum_{0 < k} \begin{bmatrix} c_{k,\uparrow}^\dagger & c_{k-2k_F,\downarrow}^\dagger \end{bmatrix} \begin{bmatrix} \frac{\hbar^2 k^2}{2m_e} - \epsilon_F & \Delta \\ \Delta^* & \frac{\hbar^2 (k-2k_F)^2}{2m_e} - \epsilon_F \end{bmatrix} \begin{bmatrix} c_{k,\uparrow} \\ c_{k-2k_F,\downarrow} \end{bmatrix}. \quad (\text{S.19})$$

Diagonalizing this matrix, the quasiparticle energy bands below the transition temperature, for $k > 0$ measured relative to the Fermi level are obtained as

$$E_\pm(k) = \frac{\epsilon_k + \epsilon_{k-2k_F}}{2} \pm \sqrt{\left(\frac{\epsilon_k - \epsilon_{k-2k_F}}{2}\right)^2 + |\Delta|^2 - \epsilon_F}, \quad (\text{S.20})$$

where

$$\epsilon_k = \frac{\hbar^2 k^2}{2m_e}. \quad (\text{S.21})$$

For $k < 0$, the band dispersion can be obtained by replacing $k \rightarrow -k$ in the above expression. Thus, in the extended zone scheme, the band structure is composed of the following branches:

$$\begin{aligned} E_-(k) & \quad (0 < k < k_F), \\ E_+(k) & \quad (k_F < k), \\ E_-(-k) & \quad (-k_F < k < 0), \\ E_+(-k) & \quad (k < -k_F). \end{aligned}$$

Let the unitary matrix used for diagonalization be defined via

$$\begin{aligned} \begin{bmatrix} \hat{\alpha}_{k,-} \\ \hat{\alpha}_{k,+} \end{bmatrix} &= U^{-1}(k) \begin{bmatrix} \hat{c}_{k,\uparrow} \\ \hat{c}_{k-2k_F,\downarrow} \end{bmatrix} \\ &= U^\dagger(k) \begin{bmatrix} \hat{c}_{k,\uparrow} \\ \hat{c}_{k-2k_F,\downarrow} \end{bmatrix} \\ &= \begin{bmatrix} u_{11}^*(k) & u_{21}^*(k) \\ u_{12}^*(k) & u_{22}^*(k) \end{bmatrix} \begin{bmatrix} \hat{c}_{k,\uparrow} \\ \hat{c}_{k-2k_F,\downarrow} \end{bmatrix}. \end{aligned} \quad (\text{S.22})$$

Then, the expectation value of the spin along the z -axis in the diagonalized bands is given by

$$E_-(k) : \quad s_z(k) = \frac{\hbar}{2} (|u_{11}(k)|^2 - |u_{21}(k)|^2) = \frac{\hbar}{2} (|\mathbf{u}_1^-(k)|^2 - |\mathbf{u}_2^-(k)|^2), \quad (\text{S.23})$$

$$E_+(k) : \quad s_z(k) = \frac{\hbar}{2} (|u_{12}(k)|^2 - |u_{22}(k)|^2) = \frac{\hbar}{2} (|\mathbf{u}_1^+(k)|^2 - |\mathbf{u}_2^+(k)|^2), \quad (\text{S.24})$$

where $\mathbf{u}^\pm(k)$ denotes the eigenvector corresponding to the eigenvalue $E_\pm(k)$.

We now focus on the fact that the electronic ordered state is primarily governed by the states near the Fermi energy. We restrict our analysis to the vicinity of (k_F, \uparrow) and $(-k_F, \downarrow)$, which are the states relevant to the CISSPT. The energy dispersion can be approximated near these points as

$$\begin{aligned} \xi_k &= \hbar v_F(k - k_F) \quad \text{for } k \simeq k_F, \\ \xi_k &= -\hbar v_F(k + k_F) \quad \text{for } k \simeq -k_F. \end{aligned} \quad (\text{S.25})$$

By expressing the Peierls gap as $\Delta = |\Delta|e^{i\phi}$, separating its amplitude and phase, the Hamiltonian becomes

$$\mathcal{H} = \sum_{0 < k} \begin{bmatrix} c_{k,\uparrow}^\dagger & c_{k-2k_F,\downarrow}^\dagger \end{bmatrix} \begin{bmatrix} \xi_k & \Delta \\ \Delta^* & -\xi_k \end{bmatrix} \begin{bmatrix} c_{k,\uparrow} \\ c_{k-2k_F,\downarrow} \end{bmatrix}, \quad (\text{S.26})$$

and the eigenvalues and eigenvectors of this matrix are given by

$$\begin{aligned} E_\pm(k) &= \pm \sqrt{\xi_k^2 + |\Delta|^2} \equiv \pm E_k, \\ U(k) &= \begin{bmatrix} u(k) & v^*(k) \\ -v(k) & u(k) \end{bmatrix}, \\ u(k) &= \sqrt{\frac{1}{2} \left(1 - \frac{\xi_k}{E_k} \right)}, \\ v(k) &= e^{-i\phi} \sqrt{\frac{1}{2} \left(1 + \frac{\xi_k}{E_k} \right)}. \end{aligned}$$

Accordingly, the expectation value of the density wave associated with the CISSPT is calculated as

$$\begin{aligned} \left\langle \sum_k \hat{c}_{k+Q,\uparrow}^\dagger \hat{c}_{k,\downarrow} \right\rangle &= \langle \hat{S}_{-Q}^{(+)} \rangle = \langle \hat{S}_Q^{(-)} \rangle^* \\ &= \sum_k \left\langle \left[u(k) \hat{\alpha}_{k,-}^\dagger + v(k) \hat{\alpha}_{k,+}^\dagger \right] \left[-v(k) \hat{\alpha}_{k,-} + u(k) \hat{\alpha}_{k,+} \right] \right\rangle \\ &= - \sum_k \frac{\Delta^*(Q)}{2E_k} (1 - 2f(E_k)), \end{aligned} \quad (\text{S.27})$$

where $f(E_k)$ is the Fermi distribution function.

On the other hand, let us denote the phonon conjugate momentum by $\hat{\pi}_{q,\lambda}$. Then the phonon Hamiltonian is expressed as

$$\begin{aligned} \hat{H}_{\text{ph}} &= \sum_{q,\lambda} \hbar \omega_{q,\lambda} b_{q,\lambda}^\dagger b_{q,\lambda} \\ &= \sum_{q,\lambda} \left[\frac{M_i \omega_{q,\lambda}^2}{2} \hat{\zeta}_{q,\lambda} \hat{\zeta}_{-q,-\lambda} + \frac{1}{2M_i} \hat{\pi}_{q,\lambda} \hat{\pi}_{-q,-\lambda} \right], \end{aligned} \quad (\text{S.28})$$

and its expectation value satisfies $\langle \hat{\pi}_{\pm Q, \pm} \rangle = 0$. The phonon-related part of the mean-field Hamiltonian is given by

$$\begin{aligned}\hat{H}_{\text{MF}}^{(\text{ph})} &= \frac{M_i \omega_{Q,+}^2}{2} \hat{\zeta}_{Q,+}^\dagger \hat{\zeta}_{Q,+} + \frac{2iQg_{\text{T}}}{\sqrt{N_i}} \langle \hat{S}_{-Q}^{(+)} \rangle \hat{\zeta}_{Q,+} + \text{h.c.} \\ &= \frac{M_i \omega_{Q,+}^2}{2} \left| \hat{\zeta}_{Q,+}^\dagger + \frac{2iQg_{\text{T}}}{\sqrt{N_i} M_i \omega_{Q,+}^2} \langle \hat{S}_{-Q}^{(+)} \rangle \right|^2 - \frac{Q^2 g_{\text{T}}^2}{N_i M_i \omega_{Q,+}^2} |\langle \hat{S}_{-Q}^{(+)} \rangle|^2.\end{aligned}\quad (\text{S.29})$$

Therefore, in the thermodynamically stable state, minimizing this energy yields the following condition.

$$\langle \hat{\zeta}_{Q,+}^\dagger \rangle + \frac{2iQg_{\text{T}}}{\sqrt{N_i} M_i \omega_{Q,+}^2} \langle \hat{S}_{-Q}^{(+)} \rangle = 0. \quad (\text{S.30})$$

Substituting the expression for $\langle \hat{S}_{-Q}^{(+)} \rangle$ and using the definition of the order parameter,

$$\Delta^* = -\frac{2iQg_{\text{T}}}{\sqrt{N_i}} \langle \hat{\zeta}_{Q,+}^\dagger \rangle, \quad (\text{S.31})$$

we eventually obtain the self-consistent equation for the order parameter:

$$\begin{aligned}\Delta^* &= -\frac{4g_{\text{T}}^2 Q^2}{N_i M_i \omega_{Q,+}^2} \langle \hat{S}_{-Q}^{(+)} \rangle \\ &= \frac{4g_{\text{T}}^2 Q^2}{N_i M_i \omega_{Q,+}^2} \Delta^* \sum_k \frac{1}{2E_k} (1 - 2f(E_k)).\end{aligned}\quad (\text{S.32})$$

This can be simplified as

$$1 = \frac{4g_{\text{T}}^2 Q^2}{M_i \omega_{Q,+}^2} \cdot \frac{1}{N_i} \sum_k \frac{1}{2E_k} (1 - 2f(E_k)). \quad (\text{S.33})$$

The summation over the crystal momenta can be rewritten as

$$\begin{aligned}\frac{1}{N_i} \sum_k \frac{1}{2E_k} (1 - 2f(E_k)) &= \frac{\Omega}{2\pi} \int dk \frac{1}{2E_k} \tanh\left(\frac{E_k}{2k_B T}\right) \\ &= \frac{\Omega}{4\pi \hbar v_F} \int_{-\epsilon_F}^{\epsilon_F} d\xi \frac{1}{\sqrt{\xi^2 + |\Delta|^2}} \tanh\left(\frac{\sqrt{\xi^2 + |\Delta|^2}}{2k_B T}\right),\end{aligned}\quad (\text{S.34})$$

where Ω is the volume of the unit cell, and especially at zero temperature $T = 0$, we have

$$\begin{aligned}\frac{1}{N_i} \sum_k \frac{1}{2E_k} (1 - 2f(E_k)) &= \frac{\Omega}{4\pi \hbar v_F} \int_{-\epsilon_F}^{\epsilon_F} d\xi \frac{1}{\sqrt{\xi^2 + |\Delta|^2}} \\ &= \frac{\Omega}{2\pi \hbar v_F} \sinh^{-1}\left(\frac{\epsilon_F}{|\Delta|}\right).\end{aligned}\quad (\text{S.35})$$

Thus, the above gap equation (S.33) can be rewritten as

$$\sinh^{-1}\left(\frac{\epsilon_F}{|\Delta|}\right) = \frac{\pi M_i (\hbar \omega_{Q,+})^2}{8g_{\text{T}}^2 m_e k_F \Omega}. \quad (\text{S.36})$$

Here, we define a dimensionless electron-phonon coupling constant by

$$\Lambda = \frac{8g_{\text{T}}^2 m_e k_F \Omega}{\pi M_i (\hbar \omega_{Q,+})^2}. \quad (\text{S.37})$$

Solving Eq. (S.36) allows us to express the Peierls gap at $T = 0$ as

$$\begin{aligned}|\Delta|_{T=0} &= \frac{\epsilon_F}{\sinh(1/\Lambda)} \\ &\simeq 2\epsilon_F \exp(-1/\Lambda),\end{aligned}\quad (\text{S.38})$$

where the last approximation corresponds to the weak coupling limit. Meanwhile, the transition temperature obtained from the Green's function method is

$$T^{(\text{TA})} = \frac{2e^\gamma}{\pi} \epsilon_F \exp(-1/\Lambda), \quad (\text{S.39})$$

so that, similarly to BCS theory and conventional Peierls transitions, the universal ratio

$$\frac{\Delta_{T=0}}{T^{(\text{TA})}} \sim 1.76. \quad (\text{S.40})$$

also holds in our model. Note that, although we here considered the case at zero temperature $T = 0$, the same results can be derived by evaluating the free energy.

5. Resultant orders in CISSPT.

The spin density order per unit length (using $\hbar/2$ as the unit) can be expressed using the inverse Fourier transform as

$$\langle \hat{\mathbf{S}}(z) \rangle = \frac{1}{N_i} \left\langle \sum_q \hat{\mathbf{S}}_q e^{iqz} \right\rangle, \quad (\text{S.41})$$

from which we obtain

$$\langle \hat{S}_x(z) \rangle = \frac{1}{2N_i} \left[\langle \hat{S}_{-Q}^{(+)} \rangle e^{-iQz} + \text{c.c.} \right] \quad (\text{S.42})$$

$$= -\frac{|\Delta|}{2\pi\hbar v_F \Lambda} \cos(Qz + \phi), \quad (\text{S.43})$$

and

$$\langle \hat{S}_y(z) \rangle = \frac{1}{2N_i} \left[-i \langle \hat{S}_{-Q}^{(+)} \rangle e^{-iQz} + \text{c.c.} \right] \quad (\text{S.44})$$

$$= \frac{|\Delta|}{2\pi\hbar v_F \Lambda} \sin(Qz + \phi). \quad (\text{S.45})$$

Here, we used $\langle \hat{S}_{-Q}^{(+)} \rangle = \langle \hat{S}_Q^{(-)} \rangle^* = -\frac{N_i}{2\pi\hbar v_F \Lambda} |\Delta| e^{-i\phi}$. Thus, the helical spin density wave in real space is given by

$$\delta \mathbf{S}(z) = \frac{|\Delta|}{2\pi\hbar v_F \Lambda} \begin{bmatrix} \cos(Qz + \phi) \\ -\sin(Qz + \phi) \\ 0 \end{bmatrix}, \quad (\text{S.46})$$

where the minus sign can be absorbed into the phase ϕ (i.e., $\phi \rightarrow \phi + \pi$), and can henceforth be regarded as a redefinition of ϕ . For the other enantiomorph, the spin texture becomes

$$\delta \mathbf{S}(z) = \frac{|\Delta|}{2\pi\hbar v_F \Lambda} \begin{bmatrix} \cos(Qz + \phi) \\ \sin(Qz + \phi) \\ 0 \end{bmatrix}. \quad (\text{S.47})$$

At the same time, the condensation of soft phonon modes $(Q, +)$ and $(-Q, -)$ leads to a structural phase transition of the crystal. The resultant lattice distortion at each spatial point is given by

$$\begin{aligned} \delta \mathbf{u}(z) &= \frac{1}{\sqrt{N_i}} \boldsymbol{\epsilon}_{Q,+} \langle \hat{\zeta}_{Q,+} \rangle e^{iQz} + \text{c.c.} \\ &= \frac{|\Delta|}{\sqrt{2}Qg_T} \begin{bmatrix} \cos(Qz + \phi + \pi/2) \\ -\sin(Qz + \phi + \pi/2) \\ 0 \end{bmatrix}. \end{aligned} \quad (\text{S.48})$$

By aligning the definition of ϕ with that used in the helical SDW, the lattice displacement becomes

$$\delta \mathbf{u}(z) = \frac{|\Delta|}{\sqrt{2}Qg_T} \begin{bmatrix} \cos(Qz + \phi - \pi/2) \\ -\sin(Qz + \phi - \pi/2) \\ 0 \end{bmatrix}. \quad (\text{S.49})$$

For the other enantiomorph, the lattice distortion becomes

$$\delta \mathbf{u}(z) = \frac{|\Delta|}{\sqrt{2}Qg_T} \begin{bmatrix} \cos(Qz + \phi - \pi/2) \\ \sin(Qz + \phi - \pi/2) \\ 0 \end{bmatrix}. \quad (\text{S.50})$$

6. Commensurability effect in CISSPT.

We have so far considered the physical properties realized by CISSPT with an incommensurate wave vector Q . In conventional CDWs and SDWs, it is well established that commensurability—when Q forms a rational fraction of the lattice periodicity—qualitatively modifies the nature of the ordered state [29, 32–38]. For example, once the electronic ordering becomes commensurate, Umklapp processes lock the phase to the lattice, opening a gap in the phason spectrum and strongly altering collective motion. For CISSPT considered here, the role of commensurability is even more drastic. The nesting vector $(Q, +)$ couples the electronic states of $\hat{c}_{k,\downarrow}$ and $\hat{c}_{k+Q,\uparrow}$, while the nesting vector $(-Q, -)$ also couples the electronic states of $\hat{c}_{k-Q,\downarrow}$ and $\hat{c}_{k,\uparrow}$. In the incommensurate case, only (k_F, \uparrow) and $(-k_F, \downarrow)$ states can be connected near the Fermi level, and these two couplings are equivalent. However, in the commensurate case, the states at k and $k + NQ$ (N integer) coincide, so that $\hat{c}_{k,\downarrow}$ and $\hat{c}_{k,\uparrow}$ can each couple to distinct electronic states. As a result, unlike in CDW or SDW systems, in the CISSPT the spin-selective gap-opening mechanism itself is prohibited in the commensurate case described below.

As before in this section, the case with soft modes $(Q, +)$ and $(-Q, -)$ is considered. In commensurate density waves, the wave vector Q is a rational fraction of the lattice reciprocal vector $G = 2\pi/c$, i.e., $Q/G = m/n$ with integers m and n , which defines a superlattice with period nc . As a result, electronic states $k, k + Q, \dots, k + (n-1)Q$ form a closed block that mixes all members, opening energy gaps not only at the Fermi level but also at multiple points across the BZ. This is in contrast to incommensurate waves, where no finite folding occurs, so only states near the Fermi surface experience significant gaps. Therefore, in a commensurate case we have to extend the minimal Hamiltonian fully including these states:

$$\hat{H}_{\text{el}}^{\text{MF}} = \sum_k \hat{C}_k^\dagger \mathbf{H}_k^{(2n)} \hat{C}_k, \quad (\text{S.51})$$

$$\hat{C}_k^\dagger = \left[\hat{c}_{k,\uparrow}^\dagger \quad \hat{c}_{k,\downarrow}^\dagger \quad \hat{c}_{k+Q,\uparrow}^\dagger \quad \hat{c}_{k+Q,\downarrow}^\dagger \cdots \hat{c}_{k+(n-1)Q,\uparrow}^\dagger \quad \hat{c}_{k+(n-1)Q,\downarrow}^\dagger \right], \quad (\text{S.52})$$

$$\mathbf{H}_k^{(2n)} = \begin{bmatrix} \xi_k & \Delta & & \dots & \Delta^\dagger \\ \Delta^\dagger & \xi_{k+Q} & \Delta & & \\ & \Delta^\dagger & \xi_{k+2Q} & \dots & \\ \vdots & & & \ddots & \Delta \\ \Delta & & & \Delta^\dagger & \xi_{k+(n-1)Q} \end{bmatrix}, \quad (\text{S.53})$$

where ξ_k is the electronic Hamiltonian including spin degrees of freedom and, in CISSPT, the electronic states (k, \downarrow) and $(k + Q, \uparrow)$ are coupled:

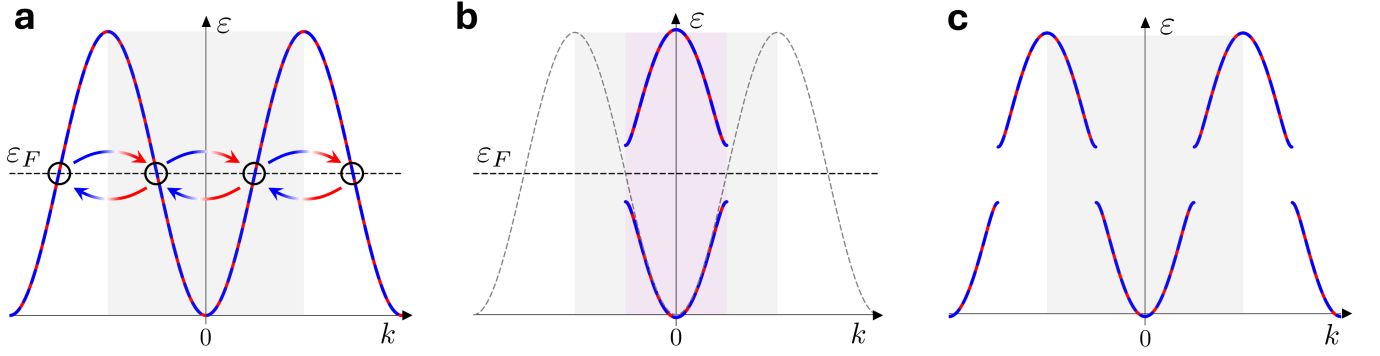
$$\Delta = \begin{bmatrix} 0 & 0 \\ \Delta & 0 \end{bmatrix}. \quad (\text{S.54})$$

The elements of this matrix can be explicitly written as

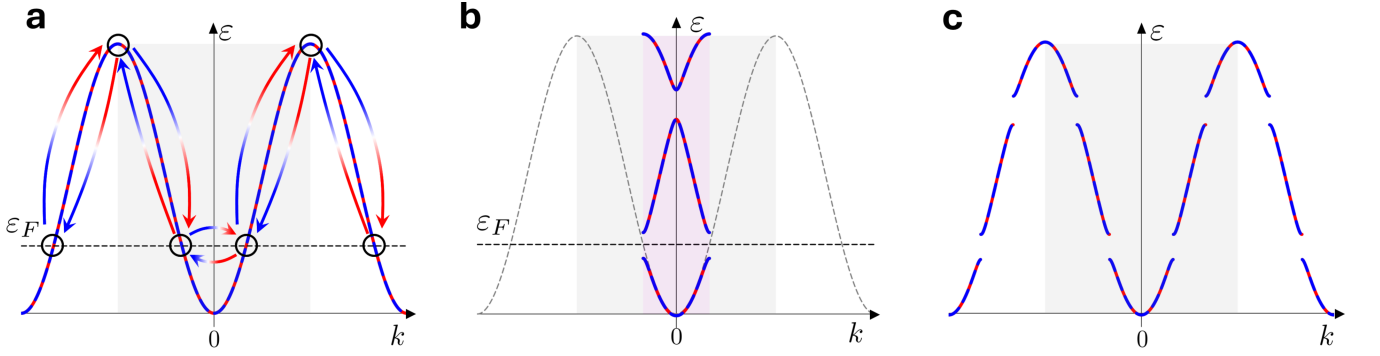
$$\mathbf{H}_k^{(2n)} = \begin{bmatrix} \xi_{k,\uparrow} & & & & & & \dots & & \Delta^* \\ & \xi_{k,\downarrow} & \Delta & & & & \dots & & \\ & \Delta^* & \xi_{k+Q,\uparrow} & & & & \dots & & \\ & & & \xi_{k+Q,\downarrow} & \Delta & & \dots & & \\ & & & \Delta^* & \xi_{k+2Q,\uparrow} & & \dots & & \\ & & & & & \xi_{k+2Q,\downarrow} & \dots & & \\ \vdots & \vdots & \vdots & \vdots & \vdots & \vdots & \ddots & \vdots & \vdots \\ \Delta & & & & & & \dots & \xi_{k+(n-1)Q,\uparrow} & \\ & & & & & & \dots & & \xi_{k+(n-1)Q,\downarrow} \end{bmatrix}. \quad (\text{S.55})$$

Therefore, although the coupling in each sector is spin-selective, both the spin-up and spin-down electronic bands exhibit Peierls gaps, resulting in apparent electronic bands that are qualitatively the same as the conventional CDWs and SDWs.

For examples, we show the cases of half-filling and one-third filling in Supplementary Figs. S6 and S7. The mean field



Supplementary Figure S6. **Schematic illustrations of electronic bands for the half-filling case.** **a**, The cosine-type and spin-degenerate electronic bands above the transition temperature. The grey shaded area represents the first BZ originating from the translational symmetry of the parent phase. The red-blue and blue-red gradient arrows couple the same electronic states shown by black circles, and connect both up and down spin sectors. **b**, The electronic bands below the transition temperature. The purple shaded area represents the reduced BZ folded by commensurate ordering vector Q . The grey dot line is the original electronic band. **c**, The unfolded electronic bands and Peierls gaps in the extended zone scheme.



Supplementary Figure S7. **Schematic illustrations of electronic bands for the one-third filling case.** **a**, The electronic bands above the transition temperature. The electronic states $k - Q$, k , $k + Q$ are coupled. **b**, The electronic bands below the transition temperature. **c**, The unfolded electronic bands and Peierls gaps in the extended zone scheme.

Hamiltonian becomes

$$\mathbf{H}_k^{(4)} = \begin{bmatrix} \xi_{k,\downarrow} & \Delta & 0 & 0 \\ \Delta^* & \xi_{k+Q,\uparrow} & 0 & 0 \\ 0 & 0 & \xi_{k+Q,\downarrow} & \Delta \\ 0 & 0 & \Delta^* & \xi_{k,\uparrow} \end{bmatrix}, \quad (\text{S.56})$$

for the half-filling case $Q/G = 1/2$, where we changed the basis so that the matrix becomes block-diagonalized. Moreover, since finite expectation values $\langle \hat{S}_{-Q}^{(+)} \rangle$ and $\langle \hat{S}_{-Q}^{(-)} \rangle$ coexist, the electronic order becomes the conventional collinear SDW:

$$\begin{aligned} \delta \mathbf{S}(z) &= \frac{|\Delta|}{2\pi\hbar v_F \Lambda} \begin{bmatrix} \cos(Qz + \phi) \\ -\sin(Qz + \phi) \\ 0 \end{bmatrix} + \frac{|\Delta|}{2\pi\hbar v_F \Lambda} \begin{bmatrix} \cos(Qz + \phi) \\ \sin(Qz + \phi) \\ 0 \end{bmatrix} \\ &= \frac{|\Delta|}{\pi\hbar v_F \Lambda} \cos(Qz + \phi) \mathbf{e}_x \\ &= \frac{|\Delta|}{\pi\hbar v_F \Lambda} \cos\left(\frac{\pi z}{c} + \phi\right) \mathbf{e}_x. \end{aligned} \quad (\text{S.57})$$

In the half-filling case, the period of the density wave is precisely twice that of the lattice, and in other words, it results in antiferromagnetic ordering. The commensurability 2 is a particularly special case when we consider CISSPT. Since $2Q = G$, the softening of chiral phonons occurs at the BZ boundary where the phonon PAM is degenerate [22, 23]. Therefore, both $\hat{\zeta}_{Q,+}$

and $\hat{\zeta}_{Q,-}$ are frozen and, as a consequence, CISSPT no longer occurs. This fact is consistent with the results thus far. Note that, however, the absence of CISSPT due to commensurability is not confined to the half-filling case.

We also provide the Hamiltonian for commensurability 3 as an example:

$$\mathbf{H}_k^{(6)} = \begin{bmatrix} \xi_{k,\downarrow} & \Delta & 0 & 0 & 0 & 0 \\ \Delta^* & \xi_{k+Q,\uparrow} & 0 & 0 & 0 & 0 \\ 0 & 0 & \xi_{k+Q,\downarrow} & \Delta & 0 & 0 \\ 0 & 0 & \Delta^* & \xi_{k+2Q,\uparrow} & 0 & 0 \\ 0 & 0 & 0 & 0 & \xi_{k+2Q,\downarrow} & \Delta \\ 0 & 0 & 0 & 0 & \Delta^* & \xi_{k,\uparrow} \end{bmatrix}, \quad (\text{S.58})$$

for the one-third filling case $Q/G = 1/3$.

From a graphical perspective, this characteristic can be understood more intuitively. Taking the case of half-filling as an example, the electronic state $(-k_F, \downarrow)$ is coupled to the state (k_F, \uparrow) shown by the blue-red gradient arrow in Supplementary Fig. S6a. At the same time, the electronic state (k_F, \downarrow) is coupled to the state $(3k_F, \uparrow)$, i.e., $(-k_F, \uparrow)$ in the first BZ. Therefore, the nesting vectors $(Q, +)$ and $(Q, -)$ coexist in the electronic states on the Fermi surface, and the up and down spin sectors couple identically. This holds at any gap position, and consequently, Peierls gaps open in both spin-up and down electronic bands.

Supplementary Note 3. Derivation of collective excitations.

In this Supplementary note, we show the detailed calculations for the collective excitations in chirality-induced spin-selective Peierls states.

1. Calculations of phason and amplitudon frequencies

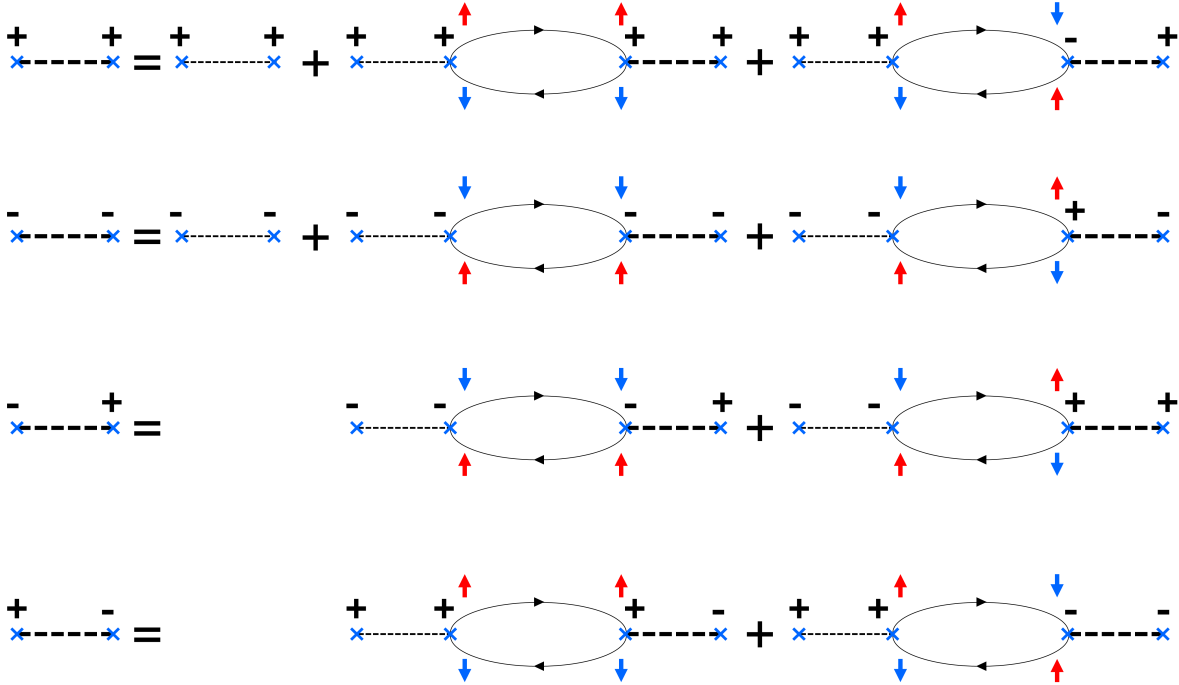
In conventional CDWs and SDWs, the primary collective excitations are phase fluctuations (phason) and amplitude fluctuations (amplitudon) of the density wave. Among them, the phason mode is of particular importance, as it underlies the sliding motion [29, 32, 33, 35, 39–41]. In CDWs, owing to the couplings with phonons, the effective masses of these modes are generally larger than the bare electron mass. This implies that the lattice follows the motion of the CDW. In contrast, the phason and amplitudon modes in SDWs are typically not coupled to phonons, and their effective masses in standard models remain comparable to the bare electron mass.

The Lee-Rice-Anderson model [41] can be applied for the calculation of the collective mode in CISSPT. Below the transition temperature, due to the presence of the nesting vector Q , phonons with wave vectors $Q + q$ and $-Q + q$ become hybridized. Therefore, in the Lee-Rice-Anderson model, the calculation within the RPA approximation is performed incorporating the density wave order. In the limit $\Delta \rightarrow 0$, this calculation coincides with the previous RPA calculation used to obtain the soft phonon mode. Since the notation can be somewhat confusing, we will continue to consider the soft modes $(Q, +)$ and $(-Q, -)$. In this case, the relevant contributions to the calculation come from the phonons with $(Q + q, \lambda = +1)$ and $(-Q + q, \lambda = -1)$, and the electronic states $(k + Q/2, s = +1/2)$ and $(k - Q/2, s = -1/2)$. Moreover, the sign of wave vector regions and spin (phonon angular momentum) are defined in the same manner as follows:

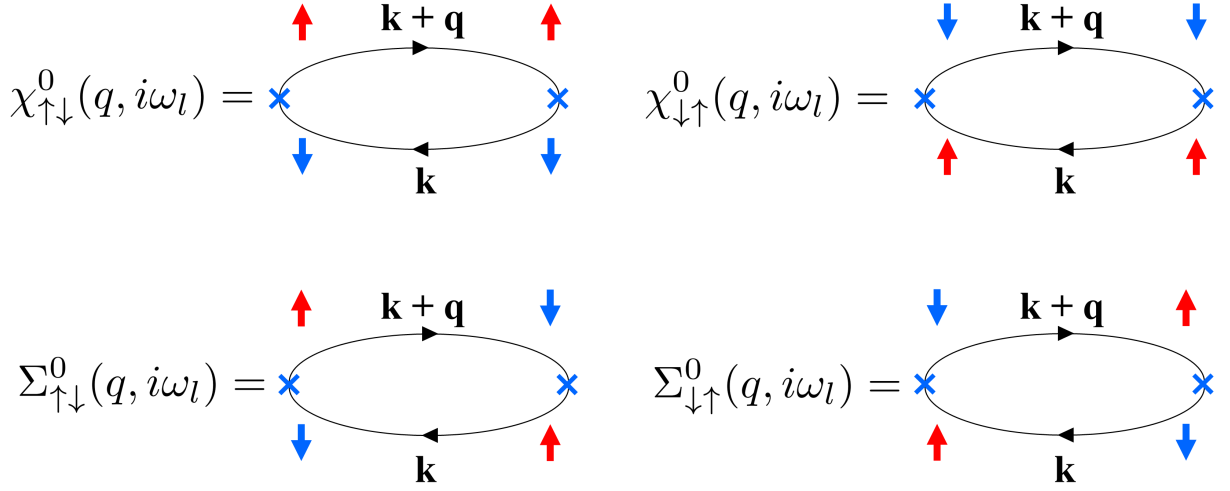
$$\hat{b}_{q+\alpha Q, \alpha}(\tau), \quad \hat{c}_{k+\alpha Q/2, \alpha/2}(\tau) \quad (\alpha = \pm). \quad (\text{S.59})$$

By employing a formulation similar to the anomalous Green function, the electron Green function is redefined as

$$\mathcal{G}_{\alpha\beta}(k, \tau) = -\langle T(\hat{c}_{k+\alpha Q/2, \alpha/2}(\tau)\hat{c}_{k+\beta Q/2, \beta/2}^\dagger) \rangle \quad (\alpha, \beta = \pm). \quad (\text{S.60})$$



Supplementary Figure S8. **Feynman diagram for the Lee-Rice-Anderson model in CISSPT.** The blue crosses represent the vertex part for $\hat{H}_{\text{ep}}^{(\text{T})}$. The red and blue arrows indicate spin up and down, respectively. The $+$ and $-$ denote the sign of the coupled phonon wave vector Q , that is, α .



Supplementary Figure S9. Feynman diagram defining phonon self-energy.

Defining, as in the Nambu representation for superconductors,

$$\Psi_k = \begin{bmatrix} \hat{c}_{k+Q/2,\uparrow} \\ \hat{c}_{k-Q/2,\downarrow} \end{bmatrix}, \quad \Psi_k^\dagger = \begin{bmatrix} \hat{c}_{k+Q/2,\uparrow}^\dagger & \hat{c}_{k-Q/2,\downarrow}^\dagger \end{bmatrix}, \quad (\text{S.61})$$

the Green function is expressed in matrix form as

$$\mathcal{G}(k, \tau) = \begin{bmatrix} -\langle T(\hat{c}_{k+Q/2,\uparrow}(\tau)\hat{c}_{k+Q/2,\uparrow}^\dagger) \rangle & -\langle T(\hat{c}_{k+Q/2,\uparrow}(\tau)\hat{c}_{k-Q/2,\downarrow}^\dagger) \rangle \\ -\langle T(\hat{c}_{k-Q/2,\downarrow}(\tau)\hat{c}_{k+Q/2,\uparrow}^\dagger) \rangle & -\langle T(\hat{c}_{k-Q/2,\downarrow}(\tau)\hat{c}_{k-Q/2,\downarrow}^\dagger) \rangle \end{bmatrix}. \quad (\text{S.62})$$

The inverse matrix is computed as follows:

$$\mathcal{G}^{-1}(k, i\epsilon_n) = i\epsilon_n \mathbf{I} - \mathbf{H}_k = \begin{bmatrix} i\epsilon_n - \xi_{k+Q/2,\uparrow} & -\Delta \\ -\Delta^* & i\epsilon_n - \xi_{k-Q/2,\downarrow} \end{bmatrix}, \quad (\text{S.63})$$

thus, we obtain

$$\mathcal{G}(k, i\epsilon_n) = (\det \mathcal{G})^{-1} \begin{bmatrix} i\epsilon_n - \xi_{k-Q/2,\downarrow} & \Delta \\ \Delta^* & i\epsilon_n - \xi_{k+Q/2,\uparrow} \end{bmatrix}. \quad (\text{S.64})$$

$$\det \mathcal{G} \simeq (i\epsilon_n)^2 - E_k^2. \quad (\text{S.65})$$

Similarly, the phonon Green function is redefined as

$$\mathcal{D}_{\alpha\beta}(q, \tau) = -\langle T(\hat{b}_{\alpha Q+q,\alpha}(\tau) + \hat{b}_{-\alpha Q-q,-\alpha}^\dagger(\tau))(\hat{b}_{-\beta Q-q,-\beta} + \hat{b}_{\beta Q+q,\beta}^\dagger) \rangle. \quad (\text{S.66})$$

From the above notation, the Dyson equations under the RPA shown in Supplementary Fig. S8 are as follows.

$$\begin{aligned} \mathcal{D}_{++}(q, i\omega_l) &= \mathcal{D}_{++}^{(0)}(q, i\omega_l) + \mathcal{D}_{++}^{(0)}(q, i\omega_l) \chi_{\uparrow\downarrow}^{(0)}(q, i\omega_l) \mathcal{D}_{++}(q, i\omega_l) + \mathcal{D}_{++}^{(0)}(q, i\omega_l) \Sigma_{\uparrow\downarrow}^{(0)}(q, i\omega_l) \mathcal{D}_{+-}(q, i\omega_l), \\ \mathcal{D}_{--}(q, i\omega_l) &= \mathcal{D}_{--}^{(0)}(q, i\omega_l) + \mathcal{D}_{--}^{(0)}(q, i\omega_l) \chi_{\uparrow\downarrow}^{(0)}(q, i\omega_l) \mathcal{D}_{--}(q, i\omega_l) + \mathcal{D}_{--}^{(0)}(q, i\omega_l) \Sigma_{\uparrow\downarrow}^{(0)}(q, i\omega_l) \mathcal{D}_{-+}(q, i\omega_l), \\ \mathcal{D}_{+-}(q, i\omega_l) &= \mathcal{D}_{--}^{(0)}(q, i\omega_l) \chi_{\uparrow\downarrow}^{(0)}(q, i\omega_l) \mathcal{D}_{+-}(q, i\omega_l) + \mathcal{D}_{--}^{(0)}(q, i\omega_l) \Sigma_{\uparrow\downarrow}^{(0)}(q, i\omega_l) \mathcal{D}_{++}(q, i\omega_l), \\ \mathcal{D}_{-+}(q, i\omega_l) &= \mathcal{D}_{++}^{(0)}(q, i\omega_l) \chi_{\uparrow\downarrow}^{(0)}(q, i\omega_l) \mathcal{D}_{-+}(q, i\omega_l) + \mathcal{D}_{++}^{(0)}(q, i\omega_l) \Sigma_{\uparrow\downarrow}^{(0)}(q, i\omega_l) \mathcal{D}_{--}(q, i\omega_l), \end{aligned}$$

where we redefined each bubble term as

$$\begin{aligned}\chi_{\uparrow\downarrow}^{(0)}(q, i\omega_l) &= \frac{k_B T}{N} \sum_{k, i\epsilon_n} |g_{\uparrow\downarrow}^{(T)}(Q, +)|^2 \mathcal{G}_{++}^{(0)}(k+q, i\epsilon_n + i\omega_l) \mathcal{G}_{--}^{(0)}(k, i\epsilon_n), \\ \chi_{\downarrow\uparrow}^{(0)}(q, i\omega_l) &= \frac{k_B T}{N} \sum_{k, i\epsilon_n} |g_{\downarrow\uparrow}^{(T)}(Q, -)|^2 \mathcal{G}_{--}^{(0)}(k+q, i\epsilon_n + i\omega_l) \mathcal{G}_{++}^{(0)}(k, i\epsilon_n), \\ \Sigma_{\uparrow\downarrow}^{(0)}(q, i\omega_l) &= \frac{k_B T}{N} \sum_{k, i\epsilon_n} |g_{\uparrow\downarrow}^{(T)}(Q, +)|^2 \mathcal{G}_{-+}^{(0)}(k+q, i\epsilon_n + i\omega_l) \mathcal{G}_{-+}^{(0)}(k, i\epsilon_n), \\ \Sigma_{\downarrow\uparrow}^{(0)}(q, i\omega_l) &= \frac{k_B T}{N} \sum_{k, i\epsilon_n} |g_{\downarrow\uparrow}^{(T)}(Q, -)|^2 \mathcal{G}_{+-}^{(0)}(k+q, i\epsilon_n + i\omega_l) \mathcal{G}_{+-}^{(0)}(k, i\epsilon_n).\end{aligned}$$

These bubble parts of electron-hole pairings are shown in Supplementary Fig. S9. In the region where the wave vectors k and q are small, the following relations

$$\begin{aligned}\xi_{k+Q/2\uparrow} &= \xi_{-k-Q/2\downarrow} = -\xi_{-k+Q/2\uparrow} = -\xi_{k-Q/2\downarrow}, \\ \mathcal{G}_{++}^{(0)}(k, i\epsilon_n) &= \mathcal{G}_{--}^{(0)}(-k, i\epsilon_n) = -\mathcal{G}_{--}^{(0)}(k, -i\epsilon_n),\end{aligned}$$

approximately hold. Therefore, the following symmetries exist between the electronic bubble terms;

$$\begin{aligned}\chi_{\uparrow\downarrow}^{(0)}(q, i\omega_l) &= \chi_{\downarrow\uparrow}^{(0)}(q, i\omega_l), \\ \Sigma_{\uparrow\downarrow}^{(0)}(q, i\omega_l) &= \Sigma_{\downarrow\uparrow}^{(0)}(q, i\omega_l),\end{aligned}$$

which also lead to the following relation for the phonon Green function from the Dyson equations.

$$\begin{aligned}\mathcal{D}_{++}(q, i\omega_l) &= \mathcal{D}_{--}(q, i\omega_l), \\ \mathcal{D}_{+-}(q, i\omega_l) &= \mathcal{D}_{-+}(q, i\omega_l).\end{aligned}$$

Consequently, only the Dyson equations for $\mathcal{D}_{++}(q, i\omega_l)$ and $\mathcal{D}_{+-}(q, i\omega_l)$ need to be solved. Note that in the limit of $\Delta \rightarrow 0$, $\mathcal{D}_{++}(q, i\omega_l)$ agrees with the diagram for soft phonons, while $\mathcal{D}_{+-}(q, i\omega_l)$ represents the effect of the folded BZ associated with the Peierls transition. By solving the Dyson equations, we finally obtain

$$\begin{aligned}\mathcal{D}_{++}(q, i\omega_l) + \mathcal{D}_{+-}(q, i\omega_l) &= \frac{1}{\mathcal{D}^{(0)}(Q, i\omega_l)^{-1} - \chi^{(0)}(q, i\omega_l) - \Sigma^{(0)}(q, i\omega_l)}, \\ \mathcal{D}_{++}(q, i\omega_l) - \mathcal{D}_{+-}(q, i\omega_l) &= \frac{1}{\mathcal{D}^{(0)}(Q, i\omega_l)^{-1} - \chi^{(0)}(q, i\omega_l) + \Sigma^{(0)}(q, i\omega_l)},\end{aligned}$$

where we approximated $\omega_{q\pm Q} \simeq \omega_{\pm Q}$, i.e., defined $\mathcal{D}^{(0)}(Q, i\omega_l) \equiv \mathcal{D}_T^{(0)}(Q, +, i\omega_l)$.

The frequencies of phason and amplitudon are determined in the same manner as in the Lee-Rice-Anderson model, described by the pole of

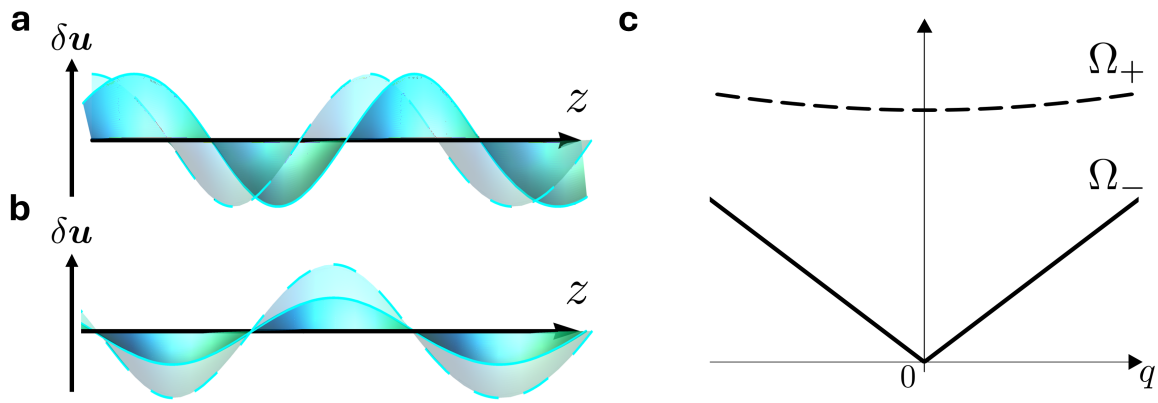
$$A_{\pm}(q, \omega) = \frac{1}{2}(\mathcal{D}_{++}(q, \omega) \pm \mathcal{D}_{+-}(q, \omega)).$$

The $\mathcal{D}_{++} + \mathcal{D}_{+-}$ mode corresponds to the amplitude fluctuation, while the $\mathcal{D}_{++} - \mathcal{D}_{+-}$ mode corresponds to the phase fluctuation [41]. This fact can be understood simply in terms of small oscillations of the phonon field around the mean field $\hat{\zeta}_0$. The fluctuation of the phonon field is decomposed as $\hat{\zeta}_{\pm Q} \simeq (\hat{\zeta}_0 + \delta\hat{\zeta})e^{\pm i\delta\phi}$ with the amplitude fluctuation $\delta\hat{\zeta}$ and the phase fluctuation $\delta\phi$. Then, to the lowest order of fluctuations, $\hat{\zeta}_Q + \hat{\zeta}_{-Q} = 2(\hat{\zeta}_0 + \delta\hat{\zeta})$ and $\hat{\zeta}_Q - \hat{\zeta}_{-Q} = 2i\delta\phi$ are satisfied. Each quantity describes the fluctuation, and therefore $\mathcal{D}_{++} \pm \mathcal{D}_{+-}$ correspond to the amplitude and phase fluctuation modes, which are illustrated in Figs. S10a and b.

The explicit calculation shows the following dispersions of the amplitude and phase modes,

$$\begin{aligned}\Omega_+^2(q) &= \Lambda\omega_{Q,+}^2 + \frac{1}{3}\frac{m_e}{m_e^*}v_F^2q^2, \\ \Omega_-^2(q) &= \frac{m_e}{m_e^*}v_F^2q^2,\end{aligned}\tag{S.67}$$

$$m_e^* \equiv m_e \left(1 + \frac{4|\Delta|^2}{\Lambda(\hbar\omega_{Q,+})^2} \right),\tag{S.68}$$



Supplementary Figure S10. **Collective modes in incommensurate CISSPT.** **a**, Schematic image of the phase mode (phason). **b**, Schematic image of the amplitude mode (amplitudon). **c**, The energy dispersions of the phason Ω_- and the amplitudon Ω_+ .

which are shown in Fig. S10c. Here, m_e^* is the effective mass reflecting the nature of CISSPT, where chiral phonons couple with electrons, and the response time becomes slower than that of bare electrons. The amplitudon mode $\Omega_+(q)$ is a gapful optical mode. Meanwhile, the phason mode $\Omega_-(q) \sim q$ is the Goldstone mode and contributes to the sliding motion of the density wave.

Supplementary Note 4. On transverse Peierls transitions and chiral charge density waves.

In the main text and Supplementary Notes 1-3, we have discussed CISSPT, taking the EPC Hamiltonian,

$$\hat{H}_{\text{ep}}^{(\text{T})} = \frac{1}{\sqrt{N}} \sum_{k,q,s,s'} \sum_{\lambda=\pm} i q g_T \hat{c}_{k+q,s}^\dagger \hat{c}_{k,s'} \hat{\zeta}_{q,\lambda} \delta_{s,s'+l_{z,\lambda}^{\text{ph}}}, \quad (\text{S.69})$$

as our starting point (see Methods). However, tracing back to its origins, this expression is the minimal Hamiltonian derived from Eq. (S.9). Therefore, another minimal model can be considered, such as the following process that preserves electron spin:

$$\hat{H}_{\text{ep}}^{(\text{T})} = \frac{1}{\sqrt{N}} \sum_{k,q,m_{\text{orb}},m'_{\text{orb}}} \sum_{\lambda=\pm} i q g_T \hat{c}_{k+q,m_{\text{orb}}}^\dagger \hat{c}_{k,m'_{\text{orb}}} \hat{\zeta}_{q,\lambda} \delta_{m_{\text{orb}},m'_{\text{orb}}+l_{z,\lambda}^{\text{ph}}}. \quad (\text{S.70})$$

We remind $\delta_{m_{\text{orb}},m'_{\text{orb}}+l_{z,\lambda}^{\text{ph}}}$ in this article means $m_{\text{orb}} = m'_{\text{orb}} + l_{z,\lambda}^{\text{ph}} \pmod{n}$. In this case, instead of the spin-flip process, coupling arises between the real-space component of the electron PAM m_{orb} and the phonon PAM. Similarly to the CISSPT, this type of EPC also induces softening dependent on phonon chirality. However, it results in transverse Peierls transitions and chiral charge density waves. In this Supplementary Note 4, we briefly discuss the transverse Peierls transition. We also show the emergence of a novel class of chiral charge density waves. Hereafter, the spin index is omitted for simplicity.

1. Transverse Peierls transitions in chiral crystals.

We first mention that the EPC of Eq. (S.70) is equivalent to that derived from the tight-binding model in Ref. [2], both satisfying the conservation law of total PAM. Unlike the transverse Peierls transition discussed in Ref. [15], the phonon dispersions here remain intrinsically non-degenerate because we focus on the Peierls transition in chiral crystals.

We here consider the system with three-fold screw symmetry, that is, electronic PAM $m_{\text{orb}} \in \{0, \pm 1\}$ and phonon PAM $l_{z,\lambda}^{\text{ph}} \in \{0, \pm 1\}$. In the Peierls transition, the time-reversal pair (k_F, m_{orb}) , $(-k_F, -m_{\text{orb}})$ is coupled by the phonon scattering. In accordance with the conservation law of total PAM, the following equation holds in the \hat{S}_3 system.

$$m_{\text{orb}} \equiv -m_{\text{orb}} + l_{z,\lambda}^{\text{ph}} \pmod{3}, \quad (\text{S.71})$$

which reduces to the compact form;

$$2 m_{\text{orb}} \equiv l_{z,\lambda}^{\text{ph}} \pmod{3}. \quad (\text{S.72})$$

Therefore, the Kohn anomaly of chiral phonon with $l_{z,\lambda}^{\text{ph}} = 1$ corresponds to the Peierls instability between the $(k_F, -1)$ and $(-k_F, 1)$ electronic states. In the same manner, the chiral phonon with $l_{z,\lambda}^{\text{ph}} = -1$ corresponds to the Peierls instability between the $(k_F, 1)$ and $(-k_F, -1)$ states. This is analogous to the spin-flip process discussed in Supplementary Note 2 and the main text, and we only have to extend it to the multiband formulation.

Following the same procedure as in Supplementary Note 2, the phonon self-energy contributed by electron particle-hole excitations reads

$$\Pi^{(\text{T})}(q, +, i\omega_m) = \frac{2\hbar q^2 g_T^2}{M_i \omega_{q,+}} \chi_{-1,1}^{(0)}(q, i\omega_m), \quad (\text{S.73})$$

$$\Pi^{(\text{T})}(q, -, i\omega_m) = \frac{2\hbar q^2 g_T^2}{M_i \omega_{q,-}} \chi_{1,-1}^{(0)}(q, i\omega_m), \quad (\text{S.74})$$

with the bare electron self-energy

$$\chi_{m_{\text{orb}}, -m_{\text{orb}}}^{(0)}(q, i\omega_m) = \frac{k_B T}{N_i} \sum_{k, i\epsilon_n} \mathcal{G}_{m_{\text{orb}}}^{(0)}(k, i\epsilon_n) \mathcal{G}_{-m_{\text{orb}}}^{(0)}(k - q, i\epsilon_n - i\omega_m), \quad (\text{S.75})$$

where $\mathcal{G}_{\text{orb}}^{(0)}(k, i\epsilon_n) = (i\epsilon_n - \xi_{k, m_{\text{orb}}})^{-1}$ is the Green function for the electron with band index m_{orb} . The phonon's self-energy in Eqs. (S.73) and (S.74) still depends on the chiral phonon frequency $\omega_{q,\lambda}$. Therefore, if phonon softening occurs in the transverse modes, the transition temperature differs for each handedness of the chiral phonon. This is the mechanism of chirality-dependent Kohn anomaly discussed in Supplementary Note 2, here realized in the electronic PAM channel.

When the phonon modes (Q, λ) and $(-Q, -\lambda)$ are frozen, the order parameter is defined by the same form as in the main text, $\Delta = 2iQg_T \langle \hat{\zeta}_{Q,+} \rangle / \sqrt{N_i}$. The electronic order parameter that acquires a finite expectation value is the inter-band density operator,

$$\hat{\rho}_Q^{(m_{\text{orb}}, -m_{\text{orb}})} \equiv \sum_k \hat{c}_{k+Q, m_{\text{orb}}}^\dagger \hat{c}_{k, -m_{\text{orb}}}. \quad (\text{S.76})$$

We hereafter assume that the soft phonon modes are (Q, λ) and $(-Q, -\lambda)$ with the incommensurate wave vector Q and introduce $2\ell \equiv l_{z,\lambda}^{\text{bh}} \pmod{3}$, i.e., $(\lambda, \ell) = (1, -1)$ or $(-1, 1)$. The relevant electronic bands near the Fermi level (k_F, ℓ) and $(-k_F, -\ell)$ construct a 2×2 minimal Hamiltonian. Defining the spinor

$$\hat{C}_k^\dagger = \begin{bmatrix} \hat{c}_{k,\ell}^\dagger & \hat{c}_{k-Q,-\ell}^\dagger \end{bmatrix}, \quad (\text{S.77})$$

the mean-field Hamiltonian becomes

$$\hat{H}_{\text{el}}^{\text{MF}} = \sum_{k>0} \hat{C}_k^\dagger \begin{bmatrix} \xi_{k,\ell} & \Delta \\ \Delta^* & \xi_{k-Q,-\ell} \end{bmatrix} \hat{C}_k. \quad (\text{S.78})$$

Accordingly, the eigenenergy is given by

$$E_{\pm}(k) = \frac{\xi_{k,\ell} + \xi_{k-Q,-\ell}}{2} \pm \sqrt{\left(\frac{\xi_{k,\ell} - \xi_{k-Q,-\ell}}{2}\right)^2 + |\Delta|^2}. \quad (\text{S.79})$$

We now obtain the real-space charge modulation by projecting the expectation value onto the real-space density operator. In complete analogy with Supplementary Note 2, the electronic density operator and Δ are connected by the following linear relation.

$$\langle \hat{\rho}_Q^{(\ell,-\ell)} \rangle = \frac{N_i}{2\pi\hbar v_F \Lambda} \Delta^*, \quad (\text{S.80})$$

where Λ is the dimensionless electron-phonon coupling constant. On the other hand, when explicitly incorporating the Bloch function and band index (here, the degrees of freedom of the electronic PAM), the electronic density is given as follows.

$$\begin{aligned} \hat{\rho}(\mathbf{r}) &= \Psi^\dagger(\mathbf{r}) \Psi(\mathbf{r}) \\ &= \sum_{m_{\text{orb}}, m'_{\text{orb}}} \sum_{k, k'} \hat{c}_{k, m_{\text{orb}}}^\dagger \hat{c}_{k', m'_{\text{orb}}} u_{k, m_{\text{orb}}}^*(z) u_{k', m'_{\text{orb}}}(z) e^{i(k'-k)z} e^{i(m'_{\text{orb}} - m_{\text{orb}})\Phi}. \end{aligned} \quad (\text{S.81})$$

By retaining the non-zero dominant finite- Q component generated by the $(\ell, -\ell)$ off-diagonal expectation value, we have

$$\begin{aligned} \langle \hat{\rho}(\mathbf{r}) \rangle &= \sum_k \langle \hat{\rho}_Q^{(\ell,-\ell)} \rangle F_\ell e^{-iQz} e^{-i2\ell\Phi} + \text{c.c.}, \\ &\propto |\Delta| \cos(Qz - 2\ell\Phi + \phi). \end{aligned} \quad (\text{S.82})$$

We defined the form factor

$$F_\ell \equiv \frac{1}{V_{\text{cell}}} \int dz u_{k+Q,\ell}^*(z) u_{k,-\ell}(z), \quad (\text{S.83})$$

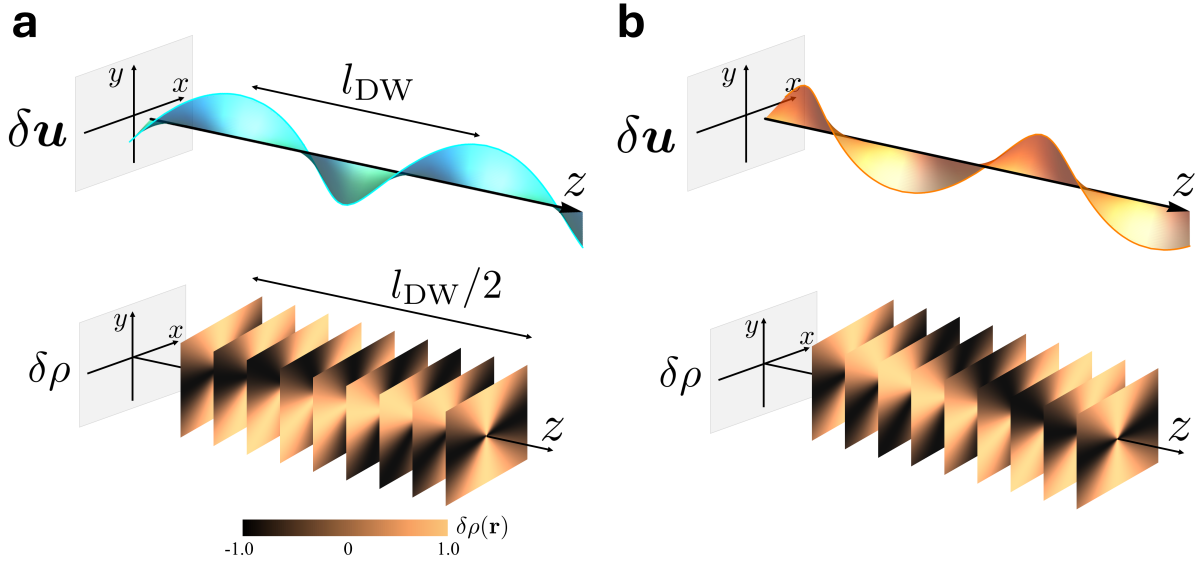
and assumed that the k -dependence of F_ℓ is negligible for brevity. To avoid confusion, we note that ϕ denotes the initial phase of the density wave, while $\Phi = \tan^{-1}(y/x)$ denotes the azimuthal angle within the xy plane. Alongside, the lattice displacement follows from the phonon condensate and results in the chiral standing wave:

$$\delta \mathbf{u}(z) = \frac{|\Delta|}{\sqrt{2} Q g_T} \begin{bmatrix} \sin(Qz + \phi) \\ -\lambda \cos(Qz + \phi) \\ 0 \end{bmatrix}, \quad (\text{S.84})$$

which is the same form as calculated in Supplementary Note 2.

This result indicates that the system experiences a chiral charge density wave associated with the transverse Peierls transition. The charge density given by Eq. (S.82) shows that the charge density wave is not a simple one-dimensional modulation $\cos(Qz)$, but rather a helical pattern with an additional winding structure $e^{\pm i2\ell\Phi}$ in the azimuthal coordinate. A close analogy is optical vortex beams [42, 43], where the factor $e^{i2\ell\Phi}$ endows photons with orbital angular momentum $2\ell\hbar$. Another analog are cholesteric liquid crystals [44, 45]. The charge density wave therefore becomes spiral order with the periodicity $2\pi/Q$ wrapped around the z -axis, with which the chiral lattice distortion possessing the same period emerges.

At the same time, the charge density wave preserves the 2ℓ -fold rotational symmetry, $\hat{C}_{2\ell}$, which originates from the inherent electronic PAM. Therefore, as shown in Supplementary Fig. S11, the charge alignment exhibits electric multipole order within each xy plane and rotates along the z -axis direction. In addition, we remark that this class of chiral CDW is entirely different



Supplementary Figure S11. **Winding charge density waves and entailed lattice distortions.** **a**, The chiral lattice distortion (top) and winding charge density wave (bottom), associated with transverse Peierls transition in the LH crystal. The color bar represents the modulation of charge density $\delta\rho(\mathbf{r})$, and we see that electric quadrupolar modulation rotates counter-clockwise along the z -axis. For clarity, we show only half a period of the winding CDW. **b**, The same figure as **a**, but in the RH crystal. The charge density wave rotates clockwise along the z -axis.

from chiral CDWs observed recently in van der Waals materials [46–55]: the former comes from a single wave vector and becomes twisted itself, while the latter originates from multiple wave number vectors, each of which is arranged by rotating relative to one another. In order to distinguish between these orders, we here refer to the CDW discussed above as a winding CDW.

In the \hat{S}_3 symmetric systems, determined by the handedness of the reference crystal, the pair of (λ, ℓ) takes the values of $(1, -1)$ or $(-1, 1)$. By substituting these values into Eqs. (S.82) and (S.84), the concrete azimuth-dependence of the ordered states becomes

$$\langle \hat{\rho}(\mathbf{r}) \rangle \propto |\Delta| \cos(Qz + 2\Phi + \phi) \equiv \delta\rho_R(\mathbf{r}), \quad (\text{S.85})$$

$$\delta\mathbf{u}(z) \propto |\Delta| \begin{bmatrix} \sin(Qz + \phi) \\ -\cos(Qz + \phi) \\ 0 \end{bmatrix}, \quad (\text{S.86})$$

for the right-handed crystals based on the notation in the main text and

$$\langle \hat{\rho}(\mathbf{r}) \rangle \propto |\Delta| \cos(Qz - 2\Phi + \phi) \equiv \delta\rho_L(\mathbf{r}), \quad (\text{S.87})$$

$$\delta\mathbf{u}(z) \propto |\Delta| \begin{bmatrix} \sin(Qz + \phi) \\ \cos(Qz + \phi) \\ 0 \end{bmatrix}, \quad (\text{S.88})$$

for the left-handed crystals. In particular, the crystals with \hat{S}_3 symmetry host the \hat{C}_2 -preserving (i.e., electric quadrupolar) winding CDW. Furthermore, the chirality, that is, the direction of the spiral in the winding CDW $\langle \hat{\rho}(\mathbf{r}) \rangle$ and the lattice distortion $\delta\mathbf{u}(z)$ is inverted among the opposite enantiomorphs because the signs of λ and ℓ ($= m_{\text{orb}}$) reverse between the right-handed and left-handed crystals.

We again emphasize the winding CDW,

$$\delta\rho_R(\mathbf{r}) = |\Delta| \cos(Qz + 2\Phi), \quad (\text{S.89})$$

is chiral. Its chiral nature is revealed by checking how $\delta\rho(\mathbf{r})$ transforms under spatial symmetries. The transformation properties under inversion, mirror, and rotation operations are summarized below:

- **Inversion** ($\mathbf{r} \rightarrow -\mathbf{r}$): $\cos(Qz + 2\Phi) \rightarrow \cos(Qz - 2\Phi)$ ($\because \Phi \rightarrow \Phi + \pi, z \rightarrow -z$)
- **Mirror in yz-plane** ($x \rightarrow -x$): $\cos(Qz + 2\Phi) \rightarrow \cos(Qz - 2\Phi)$ ($\because \Phi \rightarrow \pi - \Phi, z \rightarrow z$)

- **Mirror in xz-plane** ($y \rightarrow -y$): $\cos(Qz + 2\Phi) \rightarrow \cos(Qz - 2\Phi)$ ($\because \Phi \rightarrow -\Phi, z \rightarrow z$)
- **Diagonal mirror $x = y$** ($x \leftrightarrow y$): $\cos(Qz + 2\Phi) \rightarrow \cos(Qz - 2\Phi)$ ($\because \Phi \rightarrow \pi/2 - \Phi, z \rightarrow z$)
- **Diagonal mirror $x = -y$** ($x \leftrightarrow -y$): $\cos(Qz - 2\Phi) \rightarrow \cos(Qz - 2\Phi)$ ($\because \Phi \rightarrow -\pi/2 - \Phi, z \rightarrow z$)
- **180° rotation about z** ($C_{2,z}$): $\cos(Qz + 2\Phi) \rightarrow \cos(Qz + 2\Phi)$ ($\because \Phi \rightarrow \Phi + \pi, z \rightarrow z$)
- **180° rotation about x** ($C_{2,x}$): $\cos(Qz + 2\Phi) \rightarrow \cos(Qz + 2\Phi)$ ($\because \Phi \rightarrow -\Phi, z \rightarrow -z$)
- **180° rotation about y** ($C_{2,y}$): $\cos(Qz + 2\Phi) \rightarrow \cos(Qz + 2\Phi)$ ($\because \Phi \rightarrow \pi - \Phi, z \rightarrow -z$)

Here, we set the initial phase as $\phi = 0$. These rules show that all mirror and inversion symmetries are broken, while \hat{C}_2 rotation around the z -axis is preserved. Consequently, the azimuthal dependence encodes a well-defined handedness, confirming that the charge modulation $\delta\rho(\mathbf{r})$ is intrinsically chiral, which in turn indicates that the winding CDW is characterized by a proper pseudo-scalar. For example, by the analogy of the vortex beam, ℓ in Eq. (S.82) corresponds to the topological charge of the vortex beam. Therefore, chiral characteristics of the winding CDW, i.e., G_0 interpretation, can be expressed by a product of the wave vector Q and the winding number of phase ℓ (see Methods).

2. Collective excitations and angular momentum transport

The above formulation can be straightforwardly extended to the discussion of the collective excitations associated with the ordered phase. Importantly, since the lattice displacement field δu takes exactly the same form as in the CISSPT of the main text, the dynamical properties of the collective modes directly entail the circular motion of ions. Consequently, the sliding motion of the chiral density wave leads to a mechanical angular momentum flow, which is consistent with Ref. [15].

Moreover, the winding CDW carries a winding number 2ℓ , indicating that the density modulation itself belongs to a finite angular momentum channel. As a result, the sliding motion of the winding CDW also transports not only linear momentum (as in conventional CDWs) but also a well-defined flux of orbital angular momentum [42, 43]. This orbital angular momentum character provides a direct bridge between electronic ordering phenomena and the broader context of vortex physics in wave systems.

3. Coexistence of CISSPT and chiral charge density wave order

We comment on the possible coexistence of CISSPT and chiral CDWs. At the most fundamental level, the selection rule imposed by the conservation law of the total PAM is

$$l_{\text{PAM,el}} = l'_{\text{PAM,el}} + l_{\text{PAM,ph}}^s \pmod{n}, \quad (\text{S.90})$$

which we assumed to be decoupled as

$$m_{\text{orb}} + s = m'_{\text{orb}} + s' + l_{z,\lambda}^{\text{ph}} \pmod{n}. \quad (\text{S.91})$$

Depending on how the chiral phonon mediates transitions between electronic states, either the electronic spin sector (discussed in the main text) or the orbital sector (discussed in Supplementary Note 4) of PAM - or most significantly both simultaneously - can contribute to the Peierls instability.

This observation implies that a winding CDW and a helical SDW are not mutually exclusive but may emerge cooperatively within the same microscopic framework. Such coexistence enriches the variety of possible ordered states and highlights the central role of chiral phonons in unifying spin, orbital, and lattice degrees of freedom.

4. Extension to transverse Peierls transitions in achiral crystals.

Throughout this article, we have focused on chiral crystals, where the screw symmetry endows the electrons and phonons with well-defined pseudo angular momentum. This symmetry guarantees strict selection rules, and the resulting coupling between electronic bands and chiral phonons naturally drives transverse Peierls transitions such as the CISSPT and a winding CDW. This concept is not limited to chiral crystals. If anything, our results can naturally be extended to a more general form with n -fold rotational symmetry \hat{C}_n . In this case, the role of pseudo angular momentum is naturally replaced by the orbital angular momentum or, more strictly, by the discrete angular momentum associated with the underlying rotational symmetry \hat{C}_n [13, 24, 56, 57]. This replacement immediately generalizes the framework of Ref. [15], where the selection rule of the phonon angular momentum and electron spins was invoked, to the rigorous conservation including electronic orbital angular momentum.

The crucial difference between chiral and achiral crystals is that, in the latter, phonons carrying opposite angular momenta are generically degenerate. As pointed out by Ref. [15], if this degeneracy is lifted either intrinsically or extrinsically, the system undergoes a transverse Peierls transition accompanied by chiral CDWs. In this achiral case, the azimuthal dependence of the winding CDW that was governed by electronic PAM in chiral systems [ℓ in Eq. (S.82)] is instead determined by the orbital (or

discrete) angular momentum of the electronic bands. Therefore, extending our model can naturally reveal C_2 - and C_4 -symmetric chiral CDWs [58], linking the symmetry of the density wave order to the underlying electronic angular momentum.

* asano.shun.57x@st.kyoto-u.ac.jp

† yanase@scphys.kyoto-u.ac.jp

- [1] X. Wang, Y. Xian, and Y. Yan, **Chiral electrons and spin selectivity at chiral-achiral interfaces** (2024), arXiv:2306.01664 [cond-mat.mtrl-sci].
- [2] T. Tateishi, A. Kato, and J.-i. Kishine, Electron–chiral phonon coupling, crystal angular momentum, and phonon chirality, *Journal of the Physical Society of Japan* **94**, 053601 (2025).
- [3] I. Božovic, Possible band-structure shapes of quasi-one-dimensional solids, *Phys. Rev. B* **29**, 6586 (1984).
- [4] W. Izumida, K. Sato, and R. Saito, Spin–orbit interaction in single wall carbon nanotubes: Symmetry adapted tight-binding calculation and effective model analysis, *Journal of the Physical Society of Japan* **78**, 074707 (2009).
- [5] D. Gosálbez-Martínez, A. Crepaldi, and O. V. Yazyev, Diversity of radial spin textures in chiral materials, *Phys. Rev. B* **108**, L201114 (2023).
- [6] M. Sakano, M. Hirayama, T. Takahashi, S. Akebi, M. Nakayama, K. Kuroda, K. Taguchi, T. Yoshikawa, K. Miyamoto, T. Okuda, K. Ono, H. Kumigashira, T. Ideue, Y. Iwasa, N. Mitsuishi, K. Ishizaka, S. Shin, T. Miyake, S. Murakami, T. Sasagawa, and T. Kondo, Radial spin texture in elemental tellurium with chiral crystal structure, *Phys. Rev. Lett.* **124**, 136404 (2020).
- [7] J. A. Krieger, S. Stolz, I. Robredo, K. Manna, E. C. McFarlane, M. Date, B. Pal, J. Yang, E. B. Guedes, J. H. Dil, C. M. Polley, M. Leandersson, C. Shekhar, H. Borrmann, Q. Yang, M. Lin, V. N. Strocov, M. Caputo, M. D. Watson, T. K. Kim, C. Cacho, F. Mazzola, J. Fujii, I. Vobornik, S. S. P. Parkin, B. Bradlyn, C. Felser, M. G. Vergniory, and N. B. M. Schröter, Weyl spin-momentum locking in a chiral topological semimetal, *Nature Communications* **15**, 3720 (2024).
- [8] G. Chang, B. J. Wieder, F. Schindler, D. S. Sanchez, I. Belopolski, S.-M. Huang, B. Singh, D. Wu, T.-R. Chang, T. Neupert, S.-Y. Xu, H. Lin, and M. Z. Hasan, Topological quantum properties of chiral crystals, *Nature Materials* **17**, 978 (2018).
- [9] K. Ishito, H. Mao, Y. Kousaka, Y. Togawa, S. Iwasaki, T. Zhang, S. Murakami, J.-i. Kishine, and T. Satoh, Truly chiral phonons in α -hgs, *Nature Physics* **19**, 35 (2023).
- [10] T. Zhang and S. Murakami, Chiral phonons and pseudoangular momentum in nonsymmorphic systems, *Phys. Rev. Res.* **4**, L012024 (2022).
- [11] Y. Yang, Z. Xiao, Y. Mao, Z. Li, Z. Wang, T. Deng, Y. Tang, Z.-D. Song, Y. Li, H. Yuan, M. Shi, and Y. Xu, **Catalogue of chiral phonon materials** (2025), arXiv:2506.13721 [cond-mat.mtrl-sci].
- [12] S. Zhang, Z. Huang, M. Du, T. Ying, L. Du, and T. Zhang, **Comprehensive study of phonon chirality under symmetry constraints** (2025), arXiv:2503.22794 [cond-mat.mtrl-sci].
- [13] H. Zhu, J. Yi, M.-Y. Li, J. Xiao, L. Zhang, C.-W. Yang, R. A. Kaindl, L.-J. Li, Y. Wang, and X. Zhang, Observation of chiral phonons, *Science* **359**, 579 (2018).
- [14] X. Chen, X. Lu, S. Dubey, Q. Yao, S. Liu, X. Wang, Q. Xiong, L. Zhang, and A. Srivastava, Entanglement of single-photons and chiral phonons in atomically thin wse₂, *Nature Physics* **15**, 221 (2019).
- [15] K. Luo and X. Dai, Transverse peierls transition, *Phys. Rev. X* **13**, 011027 (2023).
- [16] G. L. Bir and G. E. Pikus, *Symmetry and strain-induced effects in semiconductors* (Wiley, 1974).
- [17] J. Fransson, Chiral phonon induced spin polarization, *Phys. Rev. Res.* **5**, L022039 (2023).
- [18] J. Fransson, Vibrational origin of exchange splitting and ”chiral-induced spin selectivity”, *Phys. Rev. B* **102**, 235416 (2020).
- [19] D. S. L. Abergel and V. I. Fal’ko, Spin-orbit-assisted electron-phonon interaction and the magnetophonon resonance in semiconductor quantum wells, *Phys. Rev. B* **77**, 035317 (2008).
- [20] A. Kumar, P. Chandra, and P. A. Volkov, Spin-phonon resonances in nearly polar metals with spin-orbit coupling, *Phys. Rev. B* **105**, 125142 (2022).
- [21] A. Kumar, P. Chandra, and P. A. Volkov, Phonon-induced collective modes in spin-orbit coupled polar metals, *Phys. Rev. B* **108**, 075162 (2023).
- [22] H. Tsunetsugu and H. Kusunose, Theory of energy dispersion of chiral phonons, *Journal of the Physical Society of Japan* **92**, 023601 (2023).
- [23] A. Kato and J.-i. Kishine, Note on angular momentum of phonons in chiral crystals, *Journal of the Physical Society of Japan* **92**, 075002 (2023).
- [24] T. Wang, H. Sun, X. Li, and L. Zhang, Chiral phonons: Prediction, verification, and application, *Nano Letters* **24**, 4311 (2024).
- [25] H. Ueda, M. García-Fernández, S. Agrestini, C. P. Romao, J. van den Brink, N. A. Spaldin, K.-J. Zhou, and U. Staub, Chiral phonons in quartz probed by x-rays, *Nature* **618**, 946 (2023).
- [26] H. Chen, W. Wu, J. Zhu, Z. Yang, W. Gong, W. Gao, S. A. Yang, and L. Zhang, Chiral phonon diode effect in chiral crystals, *Nano Letters* **22**, 1688 (2022).
- [27] J. Kishine, A. S. Ovchinnikov, and A. A. Tereshchenko, Chirality-induced phonon dispersion in a noncentrosymmetric micropolar crystal, *Phys. Rev. Lett.* **125**, 245302 (2020).
- [28] A. A. Abrikosov, I. Dzyaloshinskii, L. P. Gorkov, and R. A. Silverman, *Methods of quantum field theory in statistical physics* (Dover, New York, NY, 1975).
- [29] G. Grüner, *Density Waves In Solids*, 1st ed. (CRC Press, 1994).
- [30] A. Manchon, H. C. Koo, J. Nitta, S. M. Frolov, and R. A. Duine, New perspectives for rashba spin–orbit coupling, *Nature Materials* **14**,

871 (2015).

- [31] V. Galitski and I. B. Spielman, Spin–orbit coupling in quantum gases, *Nature* **494**, 49 (2013).
- [32] G. Grüner, The dynamics of charge-density waves, *Rev. Mod. Phys.* **60**, 1129 (1988).
- [33] G. Grüner, The dynamics of spin-density waves, *Rev. Mod. Phys.* **66**, 1 (1994).
- [34] P. M. and, Electronic crystals: an experimental overview, *Advances in Physics* **61**, 325 (2012).
- [35] G. Grüner and A. Zettl, Charge density wave conduction: A novel collective transport phenomenon in solids, *Physics Reports* **119**, 117 (1985).
- [36] A. J. Berlinsky, One-dimensional metals and charge density wave effects in these materials, *Reports on Progress in Physics* **42**, 1243 (1979).
- [37] D. Radić, Charge density waves in solids—from first concepts to modern insights, *Symmetry* **17**, 10.3390/sym17071135 (2025).
- [38] E. Fawcett, Spin-density-wave antiferromagnetism in chromium, *Rev. Mod. Phys.* **60**, 209 (1988).
- [39] H. Seo, C. Hotta, and H. Fukuyama, Toward systematic understanding of diversity of electronic properties in low-dimensional molecular solids, *Chemical Reviews* **104**, 5005 (2004).
- [40] H. Fukuyama and P. A. Lee, Dynamics of the charge-density wave. i. impurity pinning in a single chain, *Phys. Rev. B* **17**, 535 (1978).
- [41] P. Lee, T. Rice, and P. Anderson, Conductivity from charge or spin density waves, *Solid State Communications* **14**, 703 (1974).
- [42] K. Bliokh, I. Ivanov, G. Guzzinati, L. Clark, R. Van Boxem, A. Béché, R. Juchtmans, M. Alonso, P. Schattschneider, F. Nori, and J. Verbeeck, Theory and applications of free-electron vortex states, *Physics Reports* **690**, 1 (2017), theory and applications of free-electron vortex states.
- [43] S. M. Lloyd, M. Babiker, G. Thirunavukkarasu, and J. Yuan, Electron vortices: Beams with orbital angular momentum, *Rev. Mod. Phys.* **89**, 035004 (2017).
- [44] X. Zhang, Y. Xu, C. Valenzuela, X. Zhang, L. Wang, W. Feng, and Q. Li, Liquid crystal-templated chiral nanomaterials: from chiral plasmonics to circularly polarized luminescence, *Light: Science & Applications* **11**, 223 (2022).
- [45] D. Andrienko, Introduction to liquid crystals, *Journal of Molecular Liquids* **267**, 520 (2018), special Issue Dedicated to the Memory of Professor Y. Reznikov.
- [46] J. Ishioka, Y. H. Liu, K. Shimatake, T. Kurosawa, K. Ichimura, Y. Toda, M. Oda, and S. Tanda, Chiral charge-density waves, *Phys. Rev. Lett.* **105**, 176401 (2010).
- [47] H. F. Yang, K. Y. He, J. Koo, S. W. Shen, S. H. Zhang, G. Liu, Y. Z. Liu, C. Chen, A. J. Liang, K. Huang, M. X. Wang, J. J. Gao, X. Luo, L. X. Yang, J. P. Liu, Y. P. Sun, S. C. Yan, B. H. Yan, Y. L. Chen, X. Xi, and Z. K. Liu, Visualization of chiral electronic structure and anomalous optical response in a material with chiral charge density waves, *Phys. Rev. Lett.* **129**, 156401 (2022).
- [48] K. Kim, H.-W. J. Kim, S. Ha, H. Kim, J.-K. Kim, J. Kim, J. Kwon, J. Seol, S. Jung, C. Kim, D. Ishikawa, T. Manjo, H. Fukui, A. Q. R. Baron, A. Alatas, A. Said, M. Merz, M. Le Tacon, J. M. Bok, K.-S. Kim, and B. J. Kim, Origin of the chiral charge density wave in transition-metal dichalcogenide, *Nature Physics* **20**, 1919 (2024).
- [49] J. van Wezel, Chirality and orbital order in charge density waves, *Europhysics Letters* **96**, 67011 (2011).
- [50] W. Shi, B. J. Wieder, H. L. Meyerheim, Y. Sun, Y. Zhang, Y. Li, L. Shen, Y. Qi, L. Yang, J. Jena, P. Werner, K. Koepf, S. Parkin, Y. Chen, C. Felser, B. A. Bernevig, and Z. Wang, A charge-density-wave topological semimetal, *Nature Physics* **17**, 381 (2021).
- [51] Y. Zhao, Z. Nie, H. Hong, X. Qiu, S. Han, Y. Yu, M. Liu, X. Qiu, K. Liu, S. Meng, L. Tong, and J. Zhang, Spectroscopic visualization and phase manipulation of chiral charge density waves in 1t-tas₂, *Nature Communications* **14**, 2223 (2023).
- [52] S. Shao, W.-C. Chiu, M. S. Hossain, T. Hou, N. Wang, I. Belopolski, Y. Zhao, J. Ni, Q. Zhang, Y. Li, J. Liu, M. Yahyavi, Y. Jin, Q. Feng, P. Cui, C.-L. Zhang, Y. Yao, Z. Wang, J.-X. Yin, S.-Y. Xu, Q. Ma, W. bo Gao, A. Bansil, M. Z. Hasan, and G. Chang, *A predictive first-principles framework of chiral charge density waves* (2024), arXiv:2411.03664 [cond-mat.mtrl-sci].
- [53] X. Luo, D. Obeysekera, C. Won, S. H. Sung, N. Schnitzer, R. Hovden, S.-W. Cheong, J. Yang, K. Sun, and L. Zhao, Ultrafast modulations and detection of a ferro-rotational charge density wave using time-resolved electric quadrupole second harmonic generation, *Phys. Rev. Lett.* **127**, 126401 (2021).
- [54] B. Singh, G. McNamara, K.-M. Kim, S. Siddique, S. D. Funni, W. Zhang, X. Luo, P. Sakrikar, E. M. Kenney, R. Singha, S. Alekseev, S. A. A. Ghorashi, T. J. Hicken, C. Baines, H. Luetkens, Y. Wang, V. M. Plisson, M. Geiwitz, C. A. Occhialini, R. Comin, M. J. Graf, L. Zhao, J. Cano, R. M. Fernandes, J. J. Cha, L. M. Schoop, and K. S. Burch, Ferroaxial density wave from intertwined charge and orbital order in rare-earth tritellurides, *Nature Physics* **21**, 1578 (2025).
- [55] D. Wulferding, J. Park, T. Tohyama, S. R. Park, and C. Kim, Magnetic field control over the axial character of higgs modes in charge-density wave compounds, *Nature Communications* **16**, 114 (2025).
- [56] L. Zhang and Q. Niu, Angular momentum of phonons and the einstein–de haas effect, *Phys. Rev. Lett.* **112**, 085503 (2014).
- [57] L. Zhang and Q. Niu, Chiral phonons at high-symmetry points in monolayer hexagonal lattices, *Phys. Rev. Lett.* **115**, 115502 (2015).
- [58] F. Z. Yang, K. F. Luo, W. Zhang, X. Guo, W. R. Meier, H. Ni, H. X. Li, P. Mercado Lozano, G. Fabbri, A. H. Said, C. Nelson, T. T. Zhang, A. F. May, M. A. McGuire, R. Juneja, L. Lindsay, H. N. Lee, J.-M. Zuo, M. F. Chi, X. Dai, L. Zhao, and H. Miao, Incommensurate transverse peierls transition and signature of chiral charge density wave in eual₄, *Nature Communications* **16**, 10401 (2025).